UNIVERSITY OF TECHNOLOGY SYDNEY
Faculty of Engineering and Information Technology

Generalized Continuous Wave Synthetic Aperture Radar

by

Yijiang Nan

A Thesis Submitted
in Partial Fulfillment of the
Requirements for the Degree

Doctor of Philosophy

Sydney, Australia

2019

Certificate of Authorship/Originality

I, Yijiang Nan, declare that this thesis, is submitted in fulfilment of the requirements for the award of PhD, in the School of Electrical and Data Engineering, Faculty of Engineering and Information Technology at the University of Technology Sydney.

This thesis is wholly my own work unless otherwise reference or acknowledged. In addition, I certify that all information sources and literature used are indicated in the thesis.

This document has not been submitted for qualifications at any other academic institution.

This research is supported by the Australian Government Research Training Program.

Production Note:
Signature: Signature removed prior to publication.
Date: 11/10/2019

ABSTRACT

Synthetic aperture radar (SAR) suffers from several intrinsic limitations caused by the slow time sampling in azimuth. In this thesis, a generalized continuous wave synthetic aperture radar (GCW-SAR) is developed based on one-dimensional (1-D) continuous wave (CW) signalling, thus removing these limitations.

GCW-SAR reconstructs a radar image originally by correlating the received one-dimensional raw data after self-interference cancellation (SIC) with predetermined location dependent reference signals. The SIC in GCW-SAR is discussed and then the system geometry and the original imaging method are proposed. To reduce the complexity, a novel piecewise constant Doppler (PCD) algorithm based on the linear approximation of the slant range, is proposed reconstructing a SAR image recursively in azimuth. Additionally, a faster and more flexible PCD implementation, called decimated PCD algorithm, is proposed, by which the image azimuth spacing can be extended further reducing the computational cost significantly.

The PCD algorithm is the key technique for the GCW-SAR. This thesis presents a theoretical PCD imaging performance analysis. Firstly, the difference between conventional SAR imaging and PCD imaging is revealed. Exact ambiguity function expressions of the PCD imaging in range and azimuth are then derived respectively. An error function of the PCD imaging is further defined and shown to be a function of an image quality factor to quantify the imaging performance. The decimated PCD imaging error is also analyzed accordingly.

Passive GCW-SAR system and millimeter wave GCW-SAR system with deramp-on-receive are proposed respectively. A modified PCD algorithm suited for passive GCW-SAR is proposed to remove the conventional passive SAR limitations. Using deramping technique can drastically reduce the receiving sampling rate and the millimeter wave carrier enables high azimuth resolution as well as short synthetic aperture which in turn significantly reduces the imaging computational complexity. The effects of deramp-on-receive in PCD imaging is analyzed accordingly.

Finally, a real GCW-SAR experimental system is developed and the experimental results are presented. This practical system consists of four subsystems, i.e., receiver frontend subsystem, radar control subsystem, positioning control subsystem and digital imaging subsystem. The first two parts are constructed by using the AWR1843 single-chip 77-GHz FMCW radar sensor made by Texas Instruments, the third by using the linear moving platform made by FUYU Technology company, and the digital imaging is possessed by MATLAB off-line processing in a personal computer (PC). The experimental results validate the advantages of the proposed GCW-SAR system.

Acknowledgements

The work of this thesis is accomplished in the School of Electrical and Data Engineering at the University of Technology Sydney (UTS), New South Wales, Australia. Many people have offered me great assistance and contributed to my research. I am honored to have shared my best and worst moments of my doctoral study journey with them and I thank all my friends and family for their help and company along this long but fulfilling road.

Firstly, I would like to express my most sincere appreciation and gratitude to my supervisor, Prof. Xiaojing Huang, for his continual guidance and support throughout my PhD study. Prof. Huang provides me an excellent atmosphere for doing research, and I have benefited tremendously from his knowledge and great insights in the related research areas. I am also grateful to my co-supervisor Prof. Yingjie Jay Guo for his constructive suggestions and wonderful supports. All of these are extremely important for me to proceed through my doctoral program and complete my thesis.

Many thanks specially goes to my mentors including Dr. Tom Wang and Dr. Hang Li, who always have discussions with me to tackle with my research problems. I would also like to thank my friends including Hao Zhang, Ahn Tuyen Le, Hongyang Zhang, Shulin Chen, and Tianyu Yang, who are always willing to help me when I encountered difficulties.

Finally, I am greatly thankful to my parents, Hua Nan and Honghong Wang, who have worked hard to understand my PhD study and given me all of their spiritual supports.

Yijiang Nan
Sydney, Australia, 2019.

List of Publications

Journal Papers

J-1. **Y. Nan**, X. Huang and Y. J. Guo, "Generalized Continuous Wave Synthetic Aperture Radar for High Resolution and Wide Swath Remote Sensing," *in IEEE Transactions on Geoscience and Remote Sensing*, vol. 56, no. 12, pp. 7217-7229, Dec. 2018.

J-2. **Y. Nan**, X. Huang and Y. J. Guo, "A Millimeter Wave GCW-SAR Based on Deramp-on-Receive and Piecewise Constant Doppler Imaging," *in IEEE Transactions on Geoscience and Remote Sensing*, vol. 58, no. 1, pp. 680-690, Jan. 2020 .

J-3. **Y. Nan**, X. Huang and Y. J. Guo, "Piecewise Constant Doppler Algorithm: Performance Analysis and Further Simplification," *to appear in IEEE Transactions on Aerospace and Electronic System*, (Accepted on 12-Feb-2020).

Conference Papers

C-1. **Y. Nan**, X. Huang and Y. J. Guo, "A Generalized Continuous Wave Synthetic Aperture Radar," *2017 IEEE 85th Vehicular Technology Conference (VTC Spring)*, Sydney, Australia, Jun., 2017.

C-2. **Y. Nan**, X. Huang and Y. J. Guo, "Passive synthetic aperture radar imaging with piecewise constant Doppler algorithm," *2017 IEEE-APS Topical Conference on Antennas and Propagation in Wireless Communications (APWC)*, Verona, Italy, Sep., 2017.

C-3. A. T. Le, **Y. Nan**, L. C. Tran, X. Huang, Y. J. Guo and Y. Vardaxoglou, "Analog Least Mean Square Loop for Self-Interference Cancellation in Generalized Continuous Wave SAR," *2018 IEEE 88th Vehicular Technology Conference (VTC2019-Fall)*, Chicago, IL, USA, Aug., 2018.

C-4. **Y. Nan**, X. Huang and Y. J. Guo, "A Fast Piecewise Constant Doppler Algorithm for generalized Continuous Wave Synthetic Aperture Radar," *2019 International Conference on Radar (RADAR2019)*, Toulon, France, Sep., 2019.

Patents

P-1. X. Huang, Y. Nan, and Y. J. Guo, "Imaging Synthetic Aperture Radar System and Method", AU2017902109.

Contents

List of Figures

Abbreviation

ADC: Analog-to-Digital Converter

AoA: Angle-of-Arrival

BPA: Back-Projection Algorithm

CSA: Chirp Scaling Algorithm

CW: Continuous Wave

DPCA: Displaced Phase Center Antenna

DVB-T: Digital Video Broadcasting-Terrestrial

FD: Full-Duplex

FFT: Fast Fourier Transformation

FM: Frequency Modulated

FMCW: Frequency Modulated Continuous Wave

GCW-SAR: Generalized Continuous Wave Synthetic Aperture Radar

GUI: Graphical User Interface

HRWS: High Resolution and Wide Swath

IF: Intermediate Frequencies

LFM: Linearly Frequency Modulated

LNA: Low Noise Amplifier

LPF: Low-Pass Filters

MIMO: Multiple Input Multiple Output

One-Dimensional: 1-D

PA: Power Amplifier

PC: Personal Computer

PCD: Piecewise Constant Doppler

PRF: Pulse Repetition Frequency

PRI: Pulse Repetition Interval

RCM: Range Cell Migration

RCMC: Range Cell Migration Compensation

RCS: Radar Cross Section

RDA: Range Doppler Algorithm

RVP: Residual Video Phase

SAR: Synthetic Aperture Radar

SIC: Self-Interference Cancellation

SIR: Signal-to-Interference Ratio

SNR: Signal-to-Noise Ratio

SoP: Sense-on-Power

SPI: Serial Peripheral Interface

SRC: Secondary Range Compression

SS-BSAR: Space-Surface Bistatic Synthetic Aperture Radar

Two-Dimensional: 2-D

UAV: Unmanned Aerial Vehicle

WDA: Wavenumber Domain Algorithm

Chapter 1

Introduction

Synthetic aperture radar (SAR) is an important remote sensing technology used to observe the Earth and monitor the natural resources [2, 3, 4, 5, 6]. The radar-based sensors have many advantages over the optical-based ones because of their own illumination. They can work day and night under all weather conditions and provide a better discrimination of surface features than optical sensors. The transmitted electromagnetic waves can also pass through the clouds and precipitation with little or no deterioration [7, 8]. Therefore, this thesis is focused on the research of a novel SAR concept. In this chapter, the development of SAR is firstly reviewed and then the research motivation is given. The challenges, contributions and the organization of the thesis are lastly outlined.

1.1 Research Background

Radar-based sensing technique has experienced a long-term and steady growth with advances in antennas, radio frequency technology and digital technology [9]. The radar originally measures the range and direction of a target via time delay and antenna directivity, and its range and azimuth resolutions are determined by the transmitted signal bandwidth and the beamwidth of radar antenna respectively. However, a fine azimuth resolution can be hardly achieved especially considering a long-distance imaging scenario due to a small physical antenna aperture. After the principle of aperture synthesis was demonstrated by Carl Wiley in 1951, this problem was resolved by the use of Doppler frequency shift between a radar and targets. Mounted on a moving platform, the radar transmits pulses sequentially

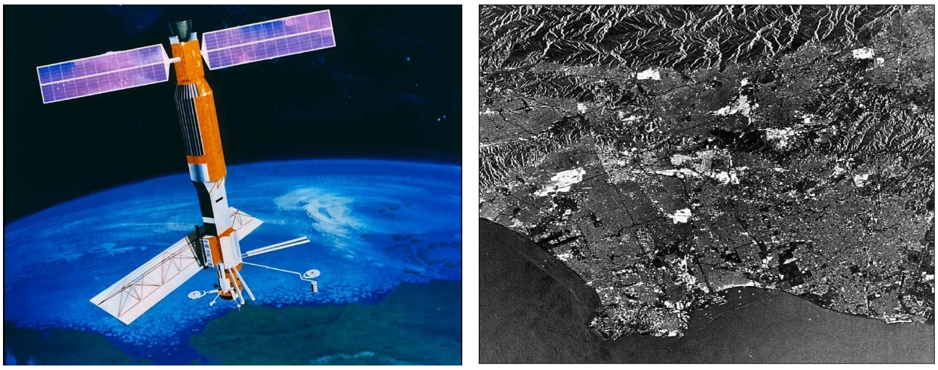

Figure 1.1 : SEASAT satellite model and a sample SEASAT-1 SAR image of the Los Angeles metropolitan area observed in 1978 (image credit JPL/NASA).

and collects the back-scattered signals reflected from the observed targets. This imaging system termed as synthetic aperture radar creates a large virtual aperture by analyzing the coherent back-scattered signals received in different radar moving positions, thus leading to a fine azimuth resolution [7, 8].

The first civilian SAR satellite "SEASAT" was launched in the late 1970s [10]. The detailed images of the atmosphere and the Earth surface over a wide area reconstructed from the received data showed the advantages of SAR in remote sensing, thus spurring a further development of spaceborne SAR system. Since then, several SAR satellites such as ERS-1, ERS-2, JERS-1 and RADARSAT-1 [11, 12, 13] have been launched and the related radar technologies including the work on digital SAR processors and specific SAR applications have been developed rapidly. To improve the image quality and simplify the imaging process, a fast SAR imaging algorithm, called range Doppler algorithm (RDA), was firstly proposed by MacDonald Dettwiler and Jet Propulsion Lab in 1978 and then well refined by other researchers. Some other fast imaging algorithms, such as chirp scaling algorithm (CSA), Omega-K algorithm, have been also developed to tackle the difficulties in SAR imaging process, e.g., range cell migration compensation (RCMC) and secondary range compression

(SRC).

With the increasing demand for dynamic monitoring of human activities, climate change and natural resources, the mapping capabilities of current SAR sensors are not sufficient to provide enough information to reconstruct a high resolution and wide swath image. A large number of new SAR systems combined with other advanced technologies have been proposed. By utilizing the phased-array antenna, either a longer synthetic aperture or a wider range swath can be obtained, resulting in two SAR working modes, i.e., Scan SAR [14, 15] and Spotlight SAR [16, 17]. Since the single-channel SAR system can only reconstruct a 2-D image of an observed scene, state-of-the-art SAR systems start to employ multiple antennas to achieve multichannel SAR data acquisition in space, time and polarization. To fully exploit multiple input multiple output (MIMO) SAR system, more new challenges like the waveform diversity design and MIMO SAR system flexibility must be overcome [18, 19, 20, 21, 22, 23]. A new class of hybrid and adaptive SAR working modes with MIMO antennas is becoming a key topic of the design of future SAR systems.

1.2 Research Motivation

SAR is a side-looking imaging radar system mounted on a spaceborne or airborne platform as shown in Fig. 1.2. In a conventional pulsed SAR system, the radar moves with a constant speed v and transmits a frequency modulated pulse signal whenever the radar travels for a pulse repetition interval (PRI). The coherent echoes received during different PRI are not overlapped and thus can construct a 2-D raw data matrix. One dimension corresponds to the time delay of the back-scattered signals, known as the fast time t. The other corresponds to the time whenever the radar travels a distance $v \cdot \mathrm{PRI}$, known as the slow time τ. The separation of fast and slow time makes it possible to consider the time delay and Doppler

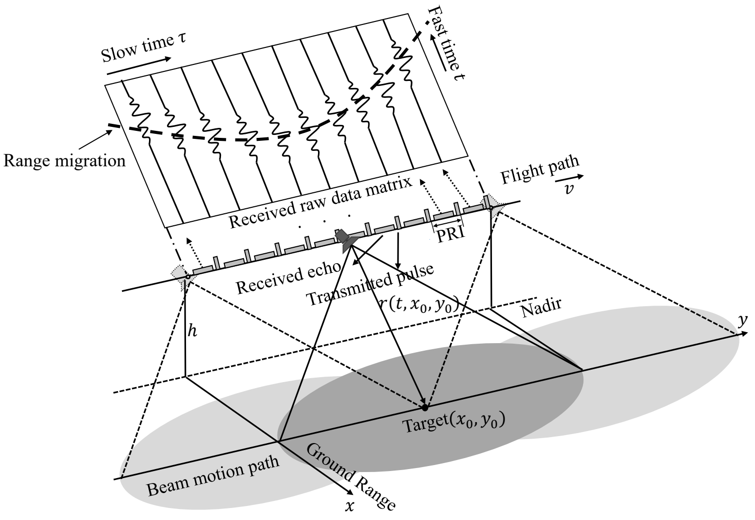

Figure 1.2 : Transmission and reception in SAR system.

frequency shift independently and thus the imaging process can be easily achieved by fast Fourier transformation (FFT). However, this 2-D data structure leads to the intrinsic limitations in the SAR system design [7, 24, 25].

1.2.1 Rigid Time Sequence Between Transmission and Reception

Conventional pulsed SAR system requires a rigid time sequence between transmission and reception to avoid the range ambiguity caused by the selection of PRI and the sidelobes of the transmitted beam. During the reception, the transmission must be stopped to prevent interference to the received echoes. Assuming that the nearest and farthest slant ranges are described as R_n and R_f, the system time sequence should satisfy $2R_n/c \geqslant T_{pd} + \Delta t$ and $PRI \geqslant 2R_f/c + T_{pd} + \Delta t$, where T_{pd} is the pulse duration and Δt is the switching time between the transmission and the reception. On the other hand, some useless echoes of the sidelobes of the transmitted beam may also reflect back to the radar. Especially the echoes reflected from the nadir with high power may be mingled with the desired echoes and deteriorate the final image. To avoid these interference, the system reception must be triggered

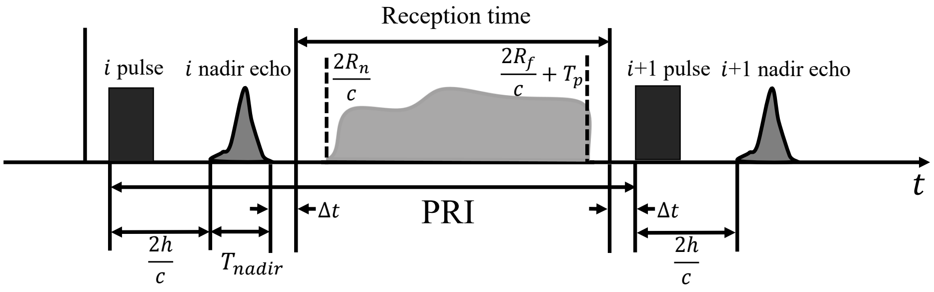

Figure 1.3 : Time sequence between transmission and reception.

the transmission pulses, desired and nadir echoes. It is evident that the rigid time sequence limits the selection of PRI.

1.2.2 Minimum Antenna Area Constraint

Although extending the synthetic aperture by shortening the antenna physical aperture can improve the azimuth resolution, a higher azimuth resolution requires a higher pulsed repetition frequency (PRF) due to a wider Doppler frequency bandwidth. On the other hand, to achieve a wider swath radar image, a lower PRF is preferable. Such conflicting requirement known as the minimum antenna area constraint renders it necessary to have a trade-off between azimuth resolution and swath width. Assuming that the swath width is W_r and θ_{Inc} is the beam incident angle, the signal reception window can be calculated as

$$T_w = 2W_r sin(\theta_{Inc})/c \tag{1.1}$$

where the W_r is approximated as $R_c\phi_r/cos(\theta_{Inc})$, R_c is the distance from the radar to the center of the beam footprint, and ϕ_r is the antenna beamwidth in range calculated as $\phi_r \approx \lambda/L_r$. L_r is the physical antenna aperture in elevation. To avoid the aliasing effect, the PRI must be larger than T_w and thus the L_r should satisfy

$$L_r \geqslant \frac{2\lambda R_f \cdot PRF \cdot tan(\theta_{Inc})}{c}. \tag{1.2}$$

On the other hand, the wide Doppler frequency bandwidth restricts the selection of the antenna aperture L_a. At any point of the observed scene, the Doppler frequency bandwidth is expressed as

$$B_a = \frac{2vsin(\phi_a)}{\lambda} \tag{1.3}$$

where ϕ_a is the antenna beamwidth in azimuth and $sin(\phi_a) \approx \phi_a$ when ϕ_a is very small. According to the sampling theorem, the PRF should be larger than B_a and thus L_a should satisfy

$$L_a \geqslant \frac{2v}{PRF}. \tag{1.4}$$

Consequently, the minimum antenna area can be further derived as

$$A_{min} = L_r L_a >= \frac{4\lambda R_f v \cdot tan(\theta_{Inc})}{c}. \tag{1.5}$$

In several practical SAR applications, the minimum antenna area is always larger than the theoretical value due to the other limitations such as the rigid time sequence requirement, the suppression of the ambiguity energy and the improvement of signal-to-noise ratio (SNR).

1.2.3 Range Cell Migration

Current SAR imaging algorithms based on the 2-D data matrix reconstruct the SAR images by using range and azimuth compression independently. After range compression, the range samples represent the distance units from the radar to the targets. The instantaneous slant range is a hyperbolic function with respect to slow time τ, and thus the azimuth samples within the same distance unit migrate over synthetic aperture as seen in Fig. 1.2. This migration is called range cell migration (RCM) which is an essential feature of the SAR, complicating the imaging process. The differences of RCMC distinguish the various SAR imaging algorithms. How to correct the RCM accurately with a low computational complexity is the key of the SAR imaging design especially for the high squint SAR imaging. In the low squint case, the RCMC and the azimuth compression can be achieved easily since the instantaneous slant range is approximated as a parabolic mode corresponding to a linear frequency modulated (FM) signal in azimuth. However, in the high squint case, a parabolic mode is not valid and the FM signal in azimuth is slightly nonlinear. The functions used in RCMC and azimuth compression have to be modified, and a new filter called secondary range compression must be used to correct the imaging error caused by a cross coupling between range and azimuth.

1.2.4 Ambiguities and Restrictions in Frequency Modulated Continuous Wave SAR

A lightweight cost-effective SAR imaging was proposed by adopting frequency modulated continuous wave (FMCW) technique as the SAR radio frontend [26, 27, 28]. FMCW SAR operates with a constant low power transmission and can be adopted in many civil and defense applications where a low cost and compact equipment is needed. In pulsed SAR, the instantaneous slant range can be assumed as a constant during each PRI due to the very short pulse time. This approximation in pulsed SAR is no longer valid in FMCW SAR since the variation of the instantaneous slant range introduced by the continuous motion during a much longer pulse time cannot be negligible. This has two effects on the FMCW SAR processors [28], i.e., a range walk term and an additional range-azimuth coupling. The range walk term, a range-invariant phase, is removed by a filter and the range-azimuth coupling complicates the interpolation in the imaging process.

1.3 Challenges, Contributions and Organization

The above mentioned limitations of SAR essentially derive from the 2-D data acquisition. If the slow time in azimuth is no longer adopted, these limitations can be totally removed. Therefore, this research aims to revisit the continuous wave (CW) imaging technology and develop a generalized continuous wave SAR (GCW-SAR) concept, by which a high resolution and wide swath image can be reconstructed from the continuous 1-D received signals.

1.3.1 Research Challenges

Removing the slow time sampling in azimuth leads to significant challenges to the GCW-SAR system design as follows.

- Firstly, to obtain the received back-scattered signals continuously, the transmission and reception of the radar must be conducted simultaneously. The transmitted signal must be subtracted before imaging due to the effect of self-interference. Self-interference cancellation (SIC) can be generally achieved in three domains: propagation domain, analog circuit domain, and digital domain, and GCW-SAR system can adopt any or all of the appropriate techniques. Though SIC as a key technique in a full-duplex system has been developed for many years, its applications in radar system have been hardly reported.

- Secondly, the variation of instantaneous slant range in GCW-SAR is expressed as a function of fast time t, and thus the azimuth information cannot be obtained independently. Therefor, the range and azimuth information has to be retrieved jointly. In conventional SAR imaging, the range and azimuth samples are manipulated respectively in a two-dimensional domain and many fast imaging algorithms can be developed based on 2-D FFT operation. Obviously, these algorithms cannot be applied in GCW-SAR and a fast imaging algorithm designed for imaging from 1-D CW data is required.

- Thirdly, the performance analysis and further simplification of the GCW-SAR imaging algorithms are also significant. Although the ambiguities caused by

RCM is removed, GCW-SAR imaging algorithms may lead to some new errors which can deteriorate the image quality. The effect of these errors to the GCW-SAR imaging performance should be analyzed in detail and a method of GCW-SAR parameter design is required for a practical GCW-SAR system.

- Finally, in order to develop practical GCW-SAR systems for different SAR applications, a real GCW-SAR experimental prototype must be built to demonstrate the GCW-SAR performance and its implementation. In this experiment, a single channel radar and a moving platform can be used for the 1-D received data and form the synthetic aperture respectively. However, there are still a number of practical issues in the system setup and signal processing for dealing with a large amount of real-time data.

1.3.2 Contributions

The main contributions of this thesis are listed as follows:

- The GCW-SAR concept is firstly developed in the thesis. In GCW-SAR, the slow time is removed and the SAR image is reconstructed by directly correlating the received 1-D raw data with predetermined location dependent reference signals after self-interference cancellation. The applicability of the SIC in GCW-SAR is discussed and the ambiguity function of this correlation based imaging process, i.e., back projection algorithm, is derived. To reduce the computational complexity, the piecewise constant Doppler (PCD) algorithm is proposed to calculate the correlation after applying the piecewise linear approximation of the range curve. A faster and more flexible PCD imaging process, called decimated PCD algorithm, is further proposed, by which the image azimuth spacing can be easily extended, leading to a further reduction of the PCD complexity.

- The PCD algorithm is the key technique in GCW-SAR imaging. The difference between conventional SAR and PCD imaging is revealed. The exact ambiguity functions of the PCD imaging in range and azimuth are derived respectively. An error function of the PCD imaging as compared with the ideal matched filtering imaging process is defined to analyze its performance and shown to be a function of an image quality factor which can be used to quantify the PCD imaging performance. Accordingly, the error function of the decimated PCD algorithm is analyzed. The method of GCW-SAR parameter design is proposed based on this performance analysis.

- Two GCW-SAR systems, i.e., passive GCW-SAR system and a millimeter wave GCW-SAR system with deramp-on-receive, are developed. After reviewing the geometry and imaging process of the conventional passive SAR system, a modified PCD algorithm is proposed for the passive GCW-SAR system. Without the slow time, many intrinsic limitations in passive SAR have been removed. The millimeter wave GCW-SAR system with deramp-on-receive is developed for low-complexity GCW-SAR implementation. Adopting the FMCW radar as radio frontend, the sampling rate in receiver can be drastically reduced and this down-sampled received signals recovered from the beat signals can be used for the PCD imaging. Using the millimeter wave transmitted signal can shorten the synthetic aperture with the same antenna aperture, thus reducing the complexity of the PCD algorithm. The effects of deramp-on-receive and millimeter wave signal on the GCW-SAR imaging process are analyzed respectively.

- A real GCW-SAR experimental system is built based on the millimeter wave GCW-SAR. The AWR1843 single-chip 77-GHz FMCW radar sensor made by Texas Instruments and a linear slider made by FUYU Technology company are adopted as the radio frontend and the moving platform respectively. The complete system consists of receiver frontend subsystem, radar control subsystem, positioning control subsystem and digital imaging subsystem. Each of them is described in details. The real imaging results are obtained to demonstrate the GCW-SAR concept, performance analysis and GCW-SAR system proposed in early chapters.

1.3.3 Thesis Organization

The rest of this thesis is organized as follows:

- *Chapter 2*: A literature review of the state-of-the-art SAR technologies is presented in this chapter. The pulsed SAR, FMCW SAR and the SAR ambiguity functions are firstly reviewed. Then, the different SAR working modes, i.e., Scan SAR and Spotlight SAR, are introduced and the corresponding imaging process and system geometry are briefly described. Finally, the modern SAR concept with multiple channel receivers including the high resolution and wide swath (HRWS) SAR and MIMO SAR systems is introduced.

- *Chapter 3*: This chapter proposes the GCW-SAR concept. Firstly, the SIC for GCW-SAR in propagation domain, analog circuit domain, and digital domain is analyzed and discussed. Then, the system geometry and the image reconstruction of the GCW-SAR are presented and the GCW-SAR ambiguity functions in range and azimuth are derived respectively. To reduce the computational cost, a fast 1-D continuous wave imaging algorithm, i.e., PCD algorithm, is developed and a flexible and simplified PCD implementation called decimated PCD algorithm is further proposed to extend the azimuth spacing of the final GCW-SAR image. The simulation results show the advantages of the GCW-SAR.

- *Chapter 4*: The PCD algorithm is the key technique to realize the GCW-SAR system and thus its performance analysis is conducted in this chapter. Firstly, the difference between the conventional SAR imaging algorithm and the PCD imaging algorithm is presented and then the ambiguity function of the PCD imaging algorithm is derived. Afterwards, the PCD imaging performance is evaluated by using a normalized imaging error function as compared with the ideal matched filtering method and the decimated PCD imaging error is also analyzed accordingly. Finally, the simulation results validate the GCW-SAR performance analysis.

- *Chapter 5*: This chapter develops two GCW-SAR system, i.e., passive GCW-SAR system and millimeter wave GCW-SAR system with deramp-on-receive. The system configuration is presented and the modified PCD algorithm suitable for the passive GCW-SAR imaging is derived in the first section. In the second section, the millimeter wave GCW-SAR system with the deramp-on-receive is also analyzed. By using the deramp-on-receive, the required sampling rate can be drastically reduced. The recovery of the received signal is described firstly and the effect of the deramping technique on the PCD imaging performance is analyzed accordingly. Then, the effect of the millimeter wave transmitted signal on the GCW-SAR system is illustrated and their advantages are demonstrated. The simulation results of the two system are presented respectively in corresponding sections.

- *Chapter 6*: A real millimeter wave GCW-SAR experimental system is built up in this chapter. The system configuration including 4 subsystems, i.e., receiver frontend subsystem, radar control subsystem, positioning control subsystem and digital imaging subsystem, is firstly presented. These subsystems are then introduced respectively in the following sections. Finally, the experimental results are shown to validate the GCW-SAR concept and performance analysis.

- *Chapter 7*: The last chapter concludes this thesis and summarizes some the future work for the GCW-SAR research.

Chapter 2

State-of-the-Art SAR Technologies

2.1 Introduction

The state-of-the-art SAR technologies are reviewed in this chapter. Section 2.2 presents the concept of SAR imaging process in pulsed SAR and FMCW SAR respectively, and derives the ambiguity function whose properties indicate the range and azimuth resolutions of the SAR system. To improve resolution or broaden wide swath, many new SAR working modes are developed by using advance techniques. The phased-array antenna [29], which can electrically steer the antenna beam, realizes the Sacn SAR and the Spotlight SAR working modes which are reviewed in Section 2.3. Applying a multiple transmit/receive antenna array to SAR imaging, the SAR system can achieve high spatial diversity, flexible transmit/receive antenna arrangement and resolution improvement and is capable of reconstructing a high resolution and wide swath image. Section 2.4 provides a brief review of these modern SAR concepts and investigates their challenges and potentials.

2.2 SAR Imaging Concept

2.2.1 Pulsed SAR

In a conventional pulsed SAR, the radar transmits an FM pulse train with an appropriate PRF. It then receives and stores the back-scattered signals. Due to the short transmission time, the range equation of a target can be assumed as a constant during pulse duration and varies from pulse to pulse. This approximation, called stop-and-go approximation, leads to the independence between the time delay of

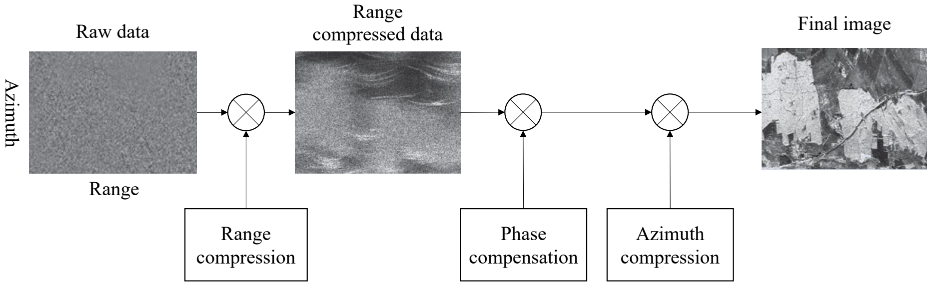

Figure 2.1 : Basic steps of pulsed SAR imaging process [1].

the received echoes and the variation of the instantaneous slant range, and thus the coherent received echoes can form a 2-D raw data matrix with respect to the fast and slow time.

Before range and azimuth compression, SAR raw data matrix does not directly show any useful information on the observed scene. Fig. 2.1 shows the basic steps of the pulsed SAR imaging process, where the time delay and the Doppler frequency shift are considered independently in range and azimuth directions [1]. The reflected signals in range direction can be compressed to short pulses by performing a convolution in time domain, which is often achieved by a multiplication in the frequency domain due to the much lower computational complexity. After the FFT operation with respect to fast time t, the received echoes with different slow time are multiplied by the complex conjugate of the spectrum of the transmitted chirp signal. A range compressed image is then obtained, revealing the relative distance between the radar and any point in the observed scene. Due to the variation of the instantaneous slant range, i.e., range equation, the RCM and SRC should be compensated before the azimuth compression. These errors can be corrected by different filters in range-Doppler or 2-D frequency domain. The azimuth compression is achieved by performing an individual convolution in different range lines. Due to the linear variation of the Doppler frequency with the radar movement, the reference signals in azimuth can be constructed as a set of chirp signals, corresponding to the range from near to far. To reduce the computational complexity, the azimuth compression can be conducted in range-Doppler or 2-D frequency domain. Finally, after inverse FFT operation, the image can be reconstructed in 2-D time domain.

2.2.2 FMCW SAR

An idea solving the high peak transmission power problem is the combination of FMCW signaling and SAR techniques, leading to a lightweight cost-effective imaging sensor, i.e., FMCW-SAR, which can operate at a constant low transmission power. In an FMCW-SAR system, the radar transmits linearly frequency modulated (LFM) signal periodically, and then the received signal is mixed with a replica (reference signal) of the transmitted signal and down converted to baseband to produce the beat signal via low pass filtering (called deramp-on-receive) [30]. The FMCW SAR system operation is shown in Fig. 2.2. Instead of using the time delay of the

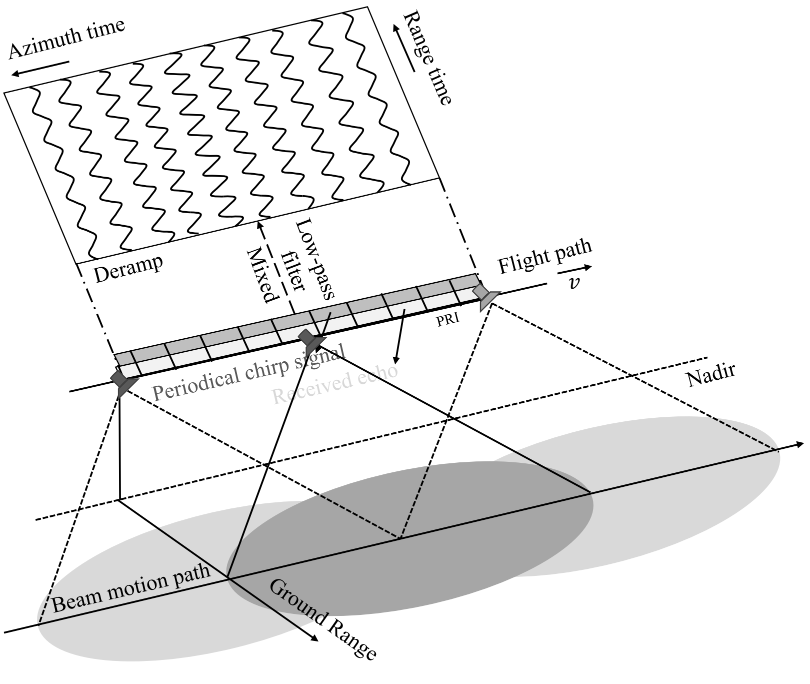

Figure 2.2 : FMCW-SAR system operation.

received echoes, the frequency difference in the beat signal during each PRI is used to determine the instantaneous range of a target.

FMCW radar has a very long transmit duration due to the need for producing the beat signal, where the transmission and the reception must be conducted simultaneously. Hence, the continuous motion of the radar during PRI cannot be negligible and the stop-and-go approximation in pulsed SAR is not valid anymore [28]. To represent the effects of the variation of the range equation during pulse duration, a more accurate signal model is required, and a more complicated imaging system has to be developed to remove the range walk term and additional range/azimuth coupling introduced by the continuous motion of the radar.

In an FMCW SAR imaging process, the residual video phase (RVP) [31] introduced by the deramp-on-received operation is firstly removed by using range FFT, chirp phase multiplication, and range inverse FFT. Then, performing azimuth FFT to transform the 2-D data to 2-D frequency domain, the range-invariant phase terms, e.g., range walk term, bulk RCM, can be removed by using the corresponding matched filters. Afterwards, the wavenumber domain algorithm (WDA) [28] is often adopted, where the Stolt interpolation can achieve azimuth compression and completely remove the range/azimuth coupling by remapping the range transformation. Finally, an FMCW SAR image can be reconstructed after transforming the compressed 2-D data to 2-D time domain.

2.2.3 SAR Ambiguity Function

The theory of radar imaging can be generally considered as a matched filtering operation to recover the radar cross section (RCS) [32]. This operation can be designed as a correlation between the received signals and a location dependent reference signal, and its output can be seen as the average of RCS weighted by the ambiguity function over a domain limited by an integration. To indicate the range and azimuth resolution, the ambiguity function of SAR system is derived in this subsection.

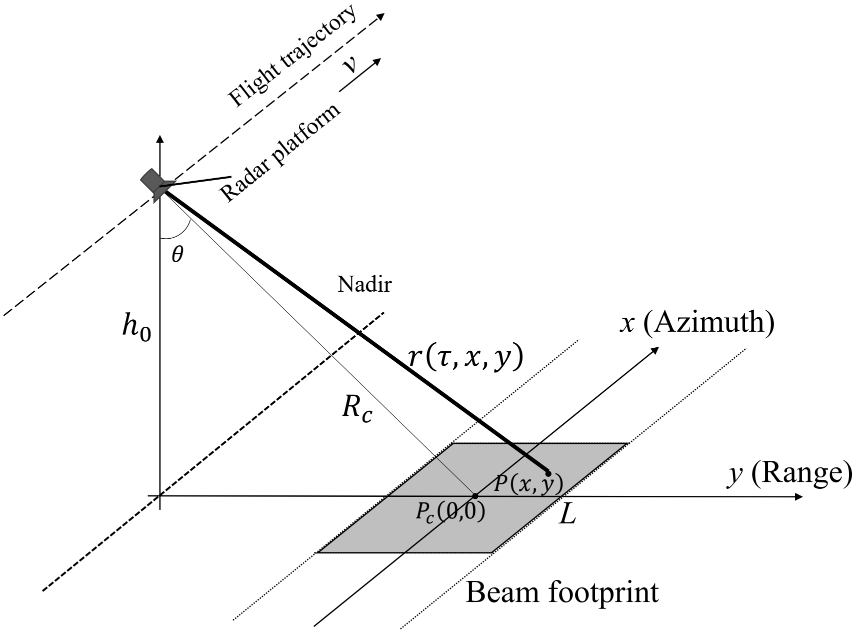

Figure 2.3 : Flat-terrain Stripmap SAR geometry.

For simplicity, consider the SAR working in the flat-terrain stripmap geometry shown in Fig. 2.3, where the side looking radar, at height h_0, travels along the x-direction with a constant speed v. Assuming that the difference between the forward and backward wave propagations is negligible, the instantaneous slant range with respect to slow time τ is derived as

$$r(\tau,x,y)=\sqrt{(R_c sin\theta+y)^2+(x-v\tau)^2+h_0^2}\approx R(y)+\frac{(x-v\tau)^2}{2R(y)} \tag{2.1}$$

where R_c is the closest range from the flight trajectory to the scene center and $R(y)=\sqrt{(R_c sin\theta+y)^2+h_0^2}$. The approximation is valid under the condition $|x-v\tau|\ll R(y)$. Assuming that the transmitted baseband signal is described as $s(t)$, the received echoes can be expressed as a superposition of a large number of reflected echoes from the beam footprint, that is

$$s_r(t,\tau) = \int\int \sigma(x,y)s(t-\frac{2r(\tau,x,y)}{c})e^{-j\frac{4\pi}{\lambda}r(\tau,x,y)}dxdy \tag{2.2}$$

where λ is the transmitted wavelength and $\sigma(x,y)$ is the RCS of the target located at (x,y). To reconstruct an imaging point $I(x',y')$, the output of the matched filter is given by

$$\begin{aligned} I(x',y') =& \int\int\int\int \sigma(x,y)s(t-\frac{2r(\tau,x,y)}{c})s^*(t-\frac{2r(\tau,x',y')}{c}) \\ &\cdot e^{-j\frac{4\pi}{\lambda}r(\tau,x,y)}e^{j\frac{4\pi}{\lambda}r(\tau,x',y')}dxdydtd\tau \\ =& \int\int \chi(x,y;x',y')\sigma(x,y)dxdy \end{aligned} \tag{2.3}$$

where $\chi(x,y;x',y')$ is the SAR ambiguity function expressed as

$$\begin{aligned} \chi(x,y;x',y') =& \int\int s(t-\frac{2r(\tau,x,y)}{c})s^*(t-\frac{2r(\tau,x',y')}{c}) \\ &\cdot e^{-j\frac{4\pi}{\lambda}r(\tau,x,y)}e^{j\frac{4\pi}{\lambda}r(\tau,x',y')}dtd\tau. \end{aligned} \tag{2.4}$$

Assuming that the range cell migration can be neglected, substituting (2.1) to (2.4), $\chi(x,y;x',y')$ can be derived as

$$\begin{aligned} \chi(x,y;x',y') \approx& \int\int s(t-\frac{2R(y)+\frac{(x-v\tau)^2}{R(y)}}{c})s^*(t-\frac{2R(y')+\frac{(x'-v\tau)^2}{R(y')}}{c}) \\ &\cdot e^{j\frac{4\pi}{\lambda}(R(y')-R(y)+\frac{(x'-v\tau)^2}{2R(y')}-\frac{(x-v\tau)^2}{2R(y)})}dtd\tau \\ \approx& \int\int s(t-\frac{2R(y)}{c})s^*(t-\frac{2R(y')}{c})e^{j\frac{4\pi}{\lambda}(R(y')-R(y)+\frac{(x'-v\tau)^2}{2R(y')}-\frac{(x-v\tau)^2}{2R(y)})}dtd\tau \end{aligned} \tag{2.5}$$

Conventional SARs often adopt the linearly frequency modulated waveform, expressed as

$$s(t) = e^{j\pi K_r t^2}, t \in [-T/2, T/2) \tag{2.6}$$

where K_r is the chirp rate and T is the chirp duration. The range and azimuth resolution factors of the SAR ambiguity function are considered respectively in this subsection:

- *Range factor*: Substituting (2.6) to (2.5) and considering the two imaging points having coordinates (x, y) and (x, y'), the range factor of the SAR ambiguity function $\chi(x, y; x, y')$ can be derived as

$$\begin{aligned}\chi(x, y; x, y') &\approx e^{j\pi K_r((\frac{2R(y)}{c})^2-(\frac{2R(y')}{c})^2)} e^{j\frac{4\pi}{\lambda}(R(y')-R(y))} \frac{Tsin(\frac{2\pi K_r T}{c}(R(y')-R(y)))}{\frac{2\pi K_r T}{c}(R(y')-R(y))} \\ &= e^{j\pi K_r((\frac{2R(y)}{c})^2-(\frac{2R(y')}{c})^2)} e^{j\frac{4\pi}{\lambda}(R(y')-R(y))} Tsinc(\frac{2\pi B}{c}(R(y')-R(y)))\end{aligned} \tag{2.7}$$

  where $sinc(t) = sin(t)/t$ is the sinc function and $K_r T = B$ is the transmitted signal bandwidth. The range resolution δ_r is determined by $R(y') - R(y) = c/(2B)$ which is the first null point in this sinc function, that is

$$\delta_{R(y)} = \frac{c}{2B}. \tag{2.8}$$

- *Azimuth factor*: When $y = y'$, the $s(t - 2R(y)/c)s^*(t - 2R(y')/c)$ is a constant and the azimuth factor of the SAR ambiguity function can be derived as

$$\begin{aligned}\chi(x, y; x', y) &\approx e^{j\frac{2\pi(x'^2-x^2)}{\lambda R(y)}} \frac{L}{v} sinc(\frac{2\pi L}{\lambda R(y)}(x' - x)) \\ &\approx e^{j\frac{2\pi(x'^2-x^2)}{\lambda R(y)}} \frac{L}{v} sinc(\frac{2\pi}{L_a}(x' - x))\end{aligned} \tag{2.9}$$

  where the antenna aperture is denoted as L_a and the synthetic aperture L is approximately equal to $\lambda/L_a \cdot R(y)$. Therefore, the azimuth resolution determined by $x' - x = L_a/2$ is derived as

$$\delta_x = \frac{L_a}{2}. \tag{2.10}$$

2.3 SAR Working Modes

A phased-array antenna can electrically create a beam of radio wave which can be steered in different directions without any antenna moving. This capability is exploited to address the trade-off between azimuth resolution and swath width and two SAR working modes, i.e., Scan SAR and Spotlight SAR, are developed. Note that the conventional SAR without beam steering is called Stripmap SAR.

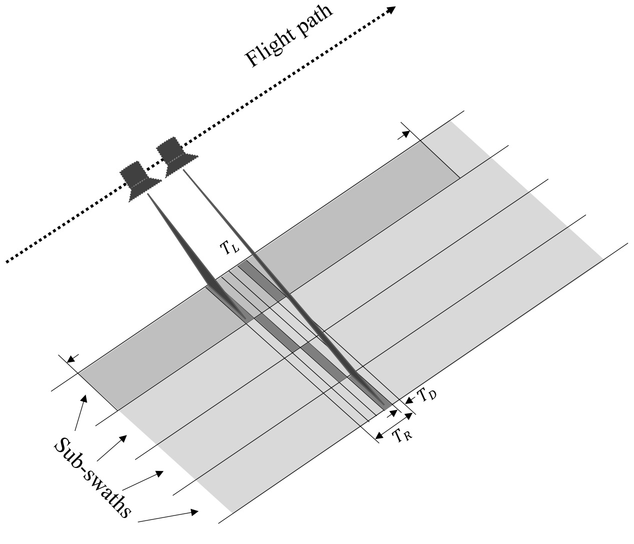

Figure 2.4 : Scan SAR system operation.

2.3.1 Scan SAR

In Scan SAR mode [13, 14, 15], a very wide swath coverage is achieved by steering the antenna beam to several range sub-swaths periodically. The sub-images of the multiple sub-swaths are reconstructed independently and then assembled to a wide-swath image at the cost of a poor azimuth resolution.

Fig. 2.4 shows a Scan SAR system operation. The radar sensor sweeps all the sub-swaths periodically and work as a burst-mode SAR for each of them. To achieve a continuous coverage in azimuth, one burst reflected from a sub-swath must be received at least over a synthetic aperture time. In Scan SAR, the variation of the beam gain leads to a nonuniform signal energy extraction from different Doppler spectrum when processing the azimuth compression. This drawback, called "scalloping" problem, can be compensated by multi-looking of the radar, i.e., a sub-swath image is reconstructed several times over a synthetic aperture time with different looking angle. The duration of the burst and the number of sub-swath are defined as T_b and N_s respectively. The period of scanning cycle can be derived as

$T_R \approx N_s \cdot T_b$ neglecting the switching time between the data acquisitions of different sub-swaths. Assuming that the synthetic aperture time is denoted as T_L, the number of looking angle to observe a sub-swath over a T_L can be derived as $N_L \approx T_L/T_R$. An increased coverage and a better scalloping compensation in Scan SAR lead to a worse azimuth resolution. An example of four sub-swath Scan SAR imaging is shown in Fig. 2.4. Assuming that the number of looking angle is $N_L = 5$, the number of azimuth samples has been reduced by $N_b \cdot N_L = 30$ times. Due to the data loss in the switching time, a smaller number of azimuth samples is acquired, leading to a very low resolution.

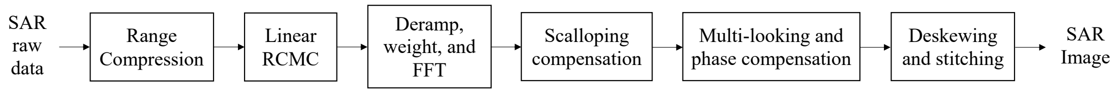

Figure 2.5 : Block diagram of SPECAN imaging process.

The data focusing of Scan SAR has been developed for many years and the most efficient one is called the SPECAN algorithm [33, 34, 35], where the azimuth compression is simplified by using the “deramping” operation. A block diagram of the SPECAN imaging process is shown in Fig. 2.5. The SPECAN algorithm adopts the same range compression in the RDA algorithm. Since the Scan SAR is designed for achieving a wide-swath image with a lower azimuth resolution, the higher order terms in the RCM can be neglected. Therefore, only a simplified linear RCMC is required in the SPECAN algorithm. Based on the deramping operation in FMCW radar, the frequency difference can also distinguish the location of the targets. The reference function is firstly produced and then multiplied by the range compressed signal. After the FFT, the azimuth of a target can be determined by the frequency value. Note that the length of FFT should be less then the pulse repetition interval to avoid the aliasing of the deramped signal. In one-look case, the scalloping in azimuth can be compensated by multiplying the data by the inverse of the energy profile with the accurate Doppler centroid estimation. Multi-looking process [36] is also adopted to reduce the effect of scalloping. The bursts of a sub-swath are spread evenly over different parts of the beam and thus the energy level of each sub-swath is balanced. This compensation is independent of Doppler centroid errors. After the azimuth compression, a skew of the data caused by the linear RCMC is corrected and image stitching is achieved. Note that the phase error caused by the derampping and FFT must be corrected if the data phase is significant for the application.

2.3.2 Spotlight SAR

In a Spotlight SAR mode [16, 17], the antenna beam continuously points to the same target area during the movement of platform, forming a longer synthetic aperture. A higher azimuth resolution image can be achieved at the cost of a non-contiguous coverage along the flight path.

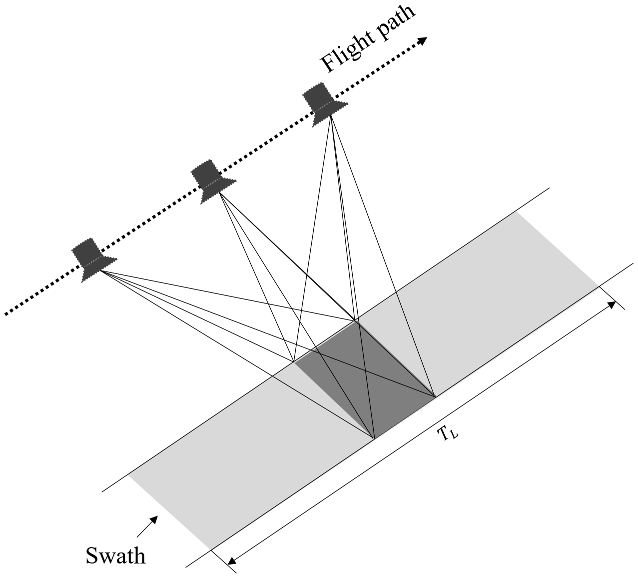

Figure 2.6 : Spotlight SAR system operation.

Fig. 2.6 shows a Spotlight SAR system operation. The synthetic aperture is no longer limited by the beam width and the azimuth resolution is determined by the data acquisition length rather than the antenna aperture. Due to the very long synthetic aperture, Spotlight SAR has some special problems [16, 37]. Firstly, due to a larger squint angle, the volume of the RCM in Spotlight SAR grows more rapidly than that in Stripmap SAR with the improvement of range resolution. Secondly, a considerable rotation between the radar and target in Spotlight SAR can cause the range courses of target scattering points beyond the imagination of a resolution cell at both range and azimuth direction, which is termed as 2-D movement through resolution cells. This rotation also leads to the space-variant phase error and different compensation phase filters have to be used to focus different scattering points. Besides, the Doppler frequency centroid constantly changes with the variation of the beam steering angle. The Doppler bandwidth in Spotlight is much larger than that in Stripmap SAR. Therefore, an efficient method should be adopted to eliminate the azimuth spectrum spread infection caused by the change of Doppler centroid, and an appropriate PRF should be selected to remove the range and azimuth ambiguities. Finally, the coupling between range and azimuth cannot be neglected in Spotlight SAR since a long synthetic aperture mandates the higher order terms of the slang range curve to be considered.

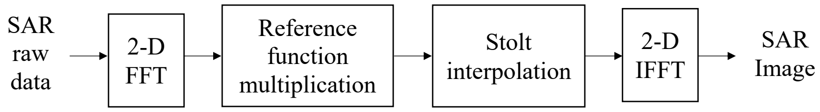

Figure 2.7 : Block diagram of ωKA imaging process.

The conventional algorithms such as RDA and SPECAN cannot compensate the range-azimuth coupling accurately. To reconstruct a high squint SAR image in Spotlight SAR, the Omega-K algorithm (ωKA) [38, 39, 40] is developed, by which the hyperbolic range equation is adopted. Fig. 2.7 shows the imaging process of the

ωKA algorithm, which is totally conducted in 2-D frequency domain. Firstly, a 2-D FFT is performed to transfer the SAR raw data to the 2-D frequency domain. Then, a reference data matrix in 2-D frequency domain is produced and multiplied by the SAR data, compensating the phase at the reference range which is usually set to the mid-swath range. The phase difference between the reference range and other ranges can be derived as a quadratic function of range and Doppler frequencies. A mapping of the range frequency axis by using Stolt interpolation [40] is adopted to adjust the range and azimuth phase difference. Finally, the SAR image can be reconstructed after 2-D IFFT. Another approximate ωKA algorithm is also proposed, where the Stolt interpolation is simplified in range-Doppler domain by using a range dependent azimuth matched filter to remove the residual azimuth modulation.

2.4 Modern SAR Concepts

In recent years, capabilities of frequent monitoring with a wide-swath and high resolution are becoming an increasingly significant issue in SAR applications. However, the conventional SAR working modes cannot simultaneously satisfy these requirements. To increase the data acquisition both in range and azimuth, SAR system is equipped with an antenna array with a group of transmit/receive elements, by which more degrees of freedom and improved spatial resolution are obtained from the advantages of MIMO architecture [41, 42].

2.4.1 High Resolution and Wide Swath SAR

A novel SAR concept, called high resolution and wide swath SAR, was firstly proposed to overcome the inevitable contradiction between the range swath and azimuth resolution [10]. This system uses a small transmitted antenna to illuminates a large area on the ground with wide swath and long synthetic aperture, and a separate large received array is employed to achieve multi-channel on receive. The system operations in range and azimuth are described as follows.

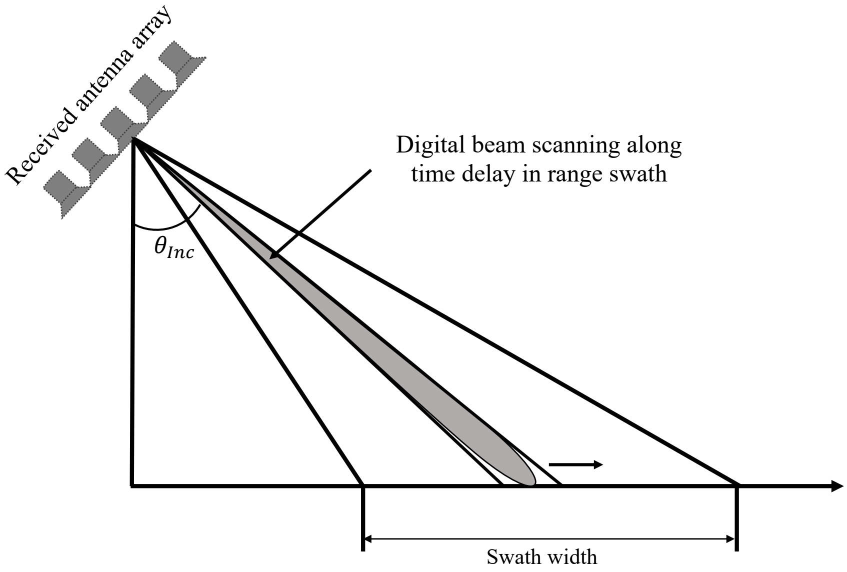

Figure 2.8 : Digital beamforming in range swath.

In range direction, the data acquisition is achieved by using a digital beamforming in elevation. Each azimuth aperture is divided into a number of vertically arranged sub-apertures and each sub-aperture covers a small part of the illuminated area. The received signals from the individual sub-apertures are then combined in real time to form a narrow beam which scans the illuminated swath following the time delay of the radar pulses, which is illustrated in Fig. 2.8 [43]. The received array collects all the radar echoes from the wide swath, thus compensating the gain loss caused by a small size of transmitted antenna.

The system operation in azimuth is shown in Fig. 2.9, where the displaced phase center antenna (DPCA) [44, 45] is adopted to increase the azimuth sampling rate and suppress the azimuth ambiguity. The multi-channel receiver in azimuth consists of M_a azimuth sub-apertures, forming M_a effective phase centers mutually displaced along the radar flight trajectory. The radar transmits a pulse and M_a sub-arrarys

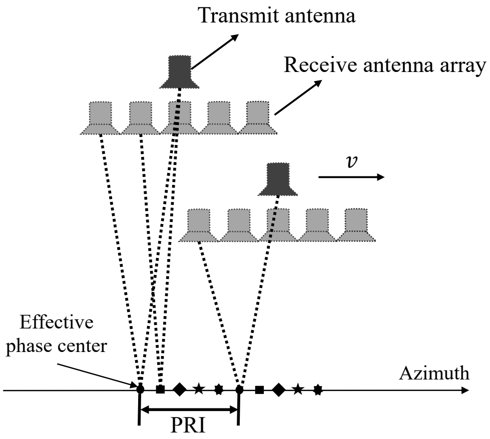

Figure 2.9 : HRWS SAR operation in azimuth.

can receive the echoes simultaneously, thus obtaining M_a azimuth samples during a PRI. With an appropriate radar moving speed, the effective azimuth sampling rate can be increased to M_a/PRI without the reduction of the range swath.

However, there are also some obvious drawbacks in HRWS SAR. The application of DPCA technique requires a stringent PRI: the radar platforms must exactly moves one half of the receive array length during a PRI to allow for a uniform sampling rate in azimuth. Some new imaging algorithms [43, 46] has been developed to overcome the rigid selection of PRF, but these methods may cause some negative effects such as ambiguous returns. On the other hand, a huge amount of data samples received from independent multiple apertures are redundant and the reduced mutual information can complicate the imaging system.

2.4.2 MIMO SAR

To further take advantage of MIMO architecture, a large receive array with multiple transmitters in combination of digital beamforming and multi-dimensional waveform encoding, termed as MIMO SAR, was developed [18, 19, 20, 21, 22, 23].

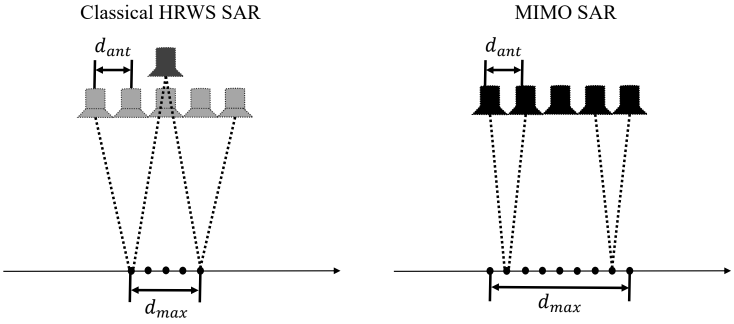

Figure 2.10 : Additional phase centers provided by multiple transmit antennas.

Multiple transmit antennas in MIMO SAR provide extra phase centers, which is shown in Fig. 2.10, compared with the phase centers in HRWS SAR. With a single transmit antenna, the HRWS SAR only has M_a effective phase centers with uniform spacing $d_{ant}/2$, where d_{ant} is the distance between two adjacent receive subapertures. The maximum distance of the effective phase centers d_{max} for HRWS SAR can be derived as $d_{max} = (M_a - 1)/2 \cdot d_{ant}$. Assuming that the MIMO SAR is employed with a transmit/receive antenna array with the same number of subapertures in HRWS SAR, $2M_a - 1$ effective phase centers can be obtained and its maximum distance $d_{max} = (M_a - 1) \cdot d_{ant}$ doubles that of the HRWS SAR.

MIMO SAR with multiple transmit and receive channels was firstly proposed to provide additional baselines for ground moving target indication (GMTI) [47, 48, 49] and SAR interferometric applications [50, 51, 52]. Then, the MIMO SAR was further developed to achieve a super resolution in range direction by observing the same target area from slightly different incident angle. Another MIMO SAR application is the fully polarimetric SAR imaging [53, 54]. In conventional SAR, two orthogonal polarizations are transmitted in subsequent PRIs alternatively, where the required high azimuth sampling rate leads to a narrow range swath. MIMO SAR can use multiple antennas to transmit two orthogonal polarizations simultaneously in a PRI, thus avoiding the limitations in conventional SAR. Nowadays, a completely new class of hybrid and adaptive MIMO SAR modes [21] are being developed. This working mode can provide different spatial or radiometric resolutions for different observed scenes at the same time. For example, Sentinel-1 [55] can observe the whole Earth surface with a moderate resolution of 20 m in Scan SAR mode, and simultaneously allow for a Stripmap SAR working mode to map a narrow swath with a significantly improved spatial resolution.

In a MIMO SAR system, orthogonal transmitted waveforms [22, 56] are adopted to separate the received echoes from multiple transmitters. The design of MIMO SAR transmitted waveform is a great challenge. On one hand, to achieve a high range resolution, a wide signal bandwidth is required. On the other hand, the radars mounted on airplanes or satellites often have a high average transmit power. A linearly frequency modulation chirp signal with good ambiguity characteristics has been widely used in SAR system, and thus a set of mutual orthogonal waveforms with different chirp rates, i.e., up and down chirp waveforms, have been developed for MIMO SAR. However, it is not sufficient to ensure the orthogonality of received echoes from different transmitters especially when considering a wide illuminated area. After the matched filtering, the unwanted orthogonal signals in the received frequency band cannot be vanished but appear in different positions. Such leaked energy is accumulated with the increasing number of orthogonal signals and deteriorates the SAR image seriously. Although the restrictions have been resolved by a short-term shift-orthogonal waveform in combination with DFB on receive [22], the increased system complexity limits the MIMO SAR applications in a space-limited spaceborne or airborne SAR. Actually, MIMO SAR still adopt the stop-and-go assumption and the slow time in azimuth, and thus cannot break the trade-off between azimuth resolution and range ambiguity. The improved spatial resolution is just achieved due to a larger data acquisition in MIMO system.

2.5 Summary

This chapter provides a literature review of the SAR technologies with a focus on the imaging process and the different working modes. The basic imaging process of the pulsed and FMCW SAR is firstly reviewed in the first section, where a 2-D SAR data structure within fast and slow time sampling is adopted and the corresponding ambiguity functions are derived. In order to reconstruct a high resolution and wide swath SAR image, current advances in different fields, e.g., phase antenna array, MIMO antenna array, digital beamforming and several novel imaging algorithms, are combined with SAR techniques, forming different novel SAR working modes, which are summarized in the second and third sections. The literature review of the state-of-the-art SAR technologies shows that the current SAR system still adopts the slow time sampling in azimuth and how to deal with the intrinsic limitations caused by slow time is still a great challenge for the future SAR system.

Chapter 3

GCW-SAR Concept

In this chapter, the GCW-SAR concept is proposed to reconstruct the SAR image from the 1-D received signals. The GCW-SAR is a combination of full-duplex (FD) radio technique and CW radar. In an FD system, transmission and reception are conducted at the same time in the same frequency band since the received signal can be extracted after SIC [57, 58, 59, 60, 61]. Applying SIC to SAR system, both transmission and reception modes can work simultaneously, and the image of an observed scene can be recovered from the received CW echo signal. Unlike the FMCW-SAR or conventional pulsed SAR, the slow time in azimuth for the separation of range and azimuth information is no longer adopted, and various SAR system restrictions are removed.

The use of SIC in GCW-SAR with a detailed analysis in propagation, analog-circuit and digital domains is firstly discussed in Section 3.1. Then, the geometry and the image reconstruction are derived in Section 3.2. In addition, Section 3.3 derives the ambiguity function of the ideal matched filter imaging based on the 1-D continuous wave received signal. To reduce the huge computational complexity in GCW-SAR imaging reconstruction, a fast imaging algorithm, called the piecewise constant Doppler algorithm, is proposed subsequently in Section 3.4, which produces the radar image recursively in the azimuth direction and is only processed in time domain. Meanwhile, a faster and more flexible GCW-SAR imaging process, called decimated PCD algorithm, is developed in Section 3.5, by which the image azimuth spacing in PCD algorithm can be easily extended and hence the computational complexity can be further reduced significantly. Simulation results are finally presented in Section 3.6, to validate the GCW-SAR concept.

3.1 SIC in GCW-SAR

SIC can be generally achieved in three domains: propagation domain, analog circuit domain, and digital domain. To ensure simultaneous transmission and reception, the GCW-SAR system can adopt any or all of the appropriate SIC techniques.

In propagation domain, if necessary, the system can use two separate antennas for transmission and reception, respectively, and provide as high as possible isolation between the transmitted and received signals through exploiting various signal propagation characteristics such as path loss [62, 63], cross-polarization [64, 65], and antenna directionality [64, 65]. In analog circuit domain, various cancellation techniques [59, 60, 61] can suppress self-interference in the analog receive-chain circuitry before the receiver's analog-to-digital converter (ADC). In the digital domain, the self-interference can be easily removed from the final reconstructed image since it represents a near-field reflection that is outside the transmission beam footprint. From the analysis and simulation results, the self-interference in digital domain has a negligible impact on the imaging quality even at a signal-to-interference ratio (SIR) of -45 dB in airborne case. Consequently, the only requirement for SIC in GCW-SAR is that the residual self-interference should be captured within the receiver's ADC dynamic range. For example, an ADC with 10 effective number of bits can have a dynamic range of 60 dB. A number of SIC techniques [57, 58, 59, 60, 61, 64, 65] have been proposed in recent years, and a total of 90-dB cancellation can be achieved in propagation and analog circuit domains, which ensures that the GCW-SAR principle can be applied in airbornebased SARs. For example, in a practical FMCW-SAR, the transmit power is 18 dBm [66, 67], and the receiver noise floor is at -90 dBm. The above-mentioned -45-dB SIR requirement implies that only 63-dB SIC is required before ADC. Considering the FM noise and other practical imperfection effects, more SIC is necessary, especially for spaceborne SARs due to longer signal propagation and possibly higher transmit power. It is believed that the increasingly better suppression in self-interference will enable the implementation of such systems in the future.

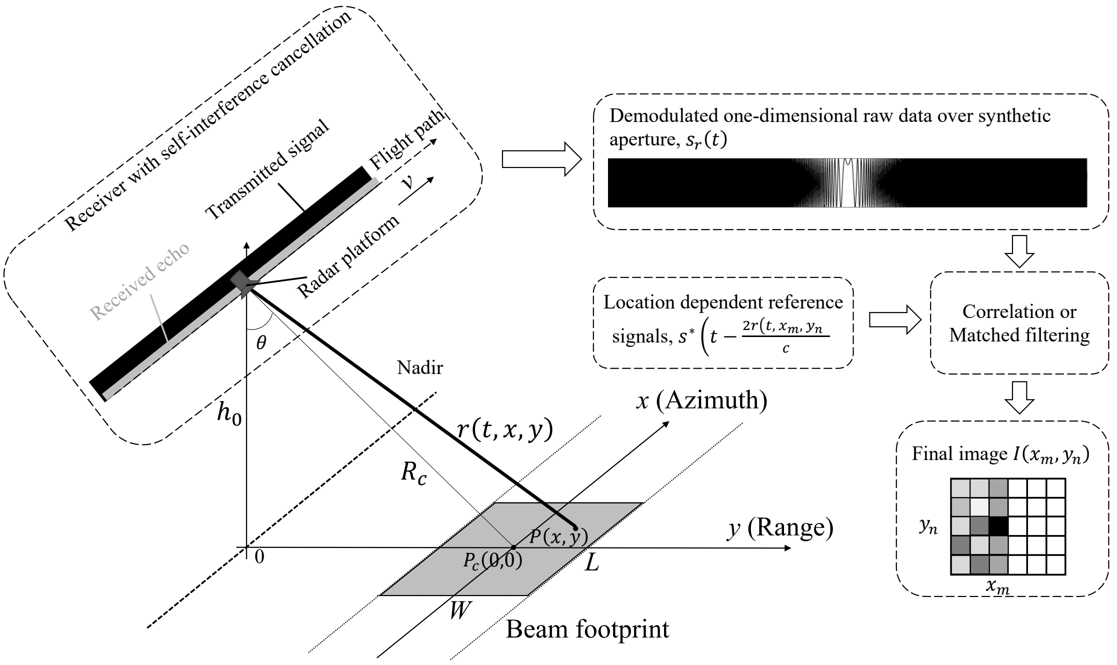

Figure 3.1 : GCW-SAR geometry and image reconstruction process.

3.2 System Geometry and Image Reconstruction

The GCW-SAR system geometry and image reconstruction process are illustrated in Fig. 3.1. The radar, at a height h_0, travels at a constant speed v in the x-direction and the origin $(0,0)$ is located at the center of the beam footprint, which is illustrated as the shaded area. The coordinate of an arbitrary point P in the beam footprint is denoted as (x,y). The round-trip delay time for the wave propagation varies as a function of time t. For simplicity, the difference between forward and back trips can be negligible [27] and the instantaneous slant range can be expressed as

$$r(t,x,y) = \sqrt{(R_c sin\theta + y)^2 + (x - vt)^2 + h_0^2} \tag{3.1}$$

where $t \in (x/v - T_L/2, x/v + T_L/2)$ and $T_L = L/v$ is the synthetic aperture time.

In a GCW-SAR, the baseband transmitted waveform $s(t)$ is up-converted to the carrier frequency and transmitted continuously. After self-interference cancellation [68], the received raw GCW-SAR data can be represented as a one-dimensional continuous wave signal $s_r(t)$, which is a superposition of a large number of reflected echoes from the beam footprint, i.e.,

$$s_r(t) = \int_{vt-\frac{L}{2}}^{vt+\frac{L}{2}} \int_{-\frac{W}{2}}^{\frac{W}{2}} \sigma(x,y) s(t - \frac{2r(t,x,y)}{c}) e^{-j\frac{4\pi}{\lambda}r(t,x,y)} dy dx \tag{3.2}$$

where the center of beam footprint is $(0, vt)$ and $\sigma(x,y)$ is the RCS of the image point (x,y). For simplicity, only the flat terrain is considered in this section.

Two separate range and azimuth compressions in conventional SAR are not valid in GCW-SAR, since the one-dimensional raw data involves both range and azimuth modulations which cannot be separated over longer pulse repetition interval for wider swath imaging. Therefore, both time delay and Doppler frequency shift of the received raw data should be considered jointly during the imaging process. For a point $P(x_m, y_n)$ in the transmitted signal beam footprint, GCW-SAR produces a location dependent reference signal and then recovers the RCS, $\sigma(x_m, y_n)$, by passing the received signal through a matched filter, which is expressed as

$$I(x_m, y_n) = \int_{\frac{x_m}{v}-\frac{T_L}{2}}^{\frac{x_m}{v}+\frac{T_L}{2}} s_r(t) s^*(t - \frac{2r(t,x_m,y_n)}{c}) e^{j\frac{4\pi}{\lambda}r(t,x_m,y_n)} dt \tag{3.3}$$

where $I(x_m, y_n)$ is the output of the matched filter, the asterisk $*$ indicates complex conjugation and $r(t, x_m, y_n)$ indicates the range from the radar antenna to the point (x_m, y_n). Based on (3.3), the image reconstruction process in principle can be described as follows. Firstly, assuming that the beam footprint is filled with a set of uniformly distributed point scatterers, whose spacings along x and y axises are Δx and Δy respectively, the pixels in the final image are arranged as a two-dimensional matrix. Secondly, the expected received signals from these pixels are used as the location dependent reference signals to be used in the matched filters. Thirdly, after the radar collects all the raw data over one synthetic aperture distance in azimuth direction, a set of pixel values in range direction for a given azimuth coordinate can be obtained by performing correlation between the received signal and the corresponding reference signals. Finally, as the GCW-SAR moves on in the azimuth direction, consecutive sets of pixel values in range direction can be obtained and a two dimensional image can be finally reconstructed. This process is also shown in Fig. 3.1.

3.3 GCW-SAR Ambiguity Function

Like the SAR ambiguity function analysis, further derivation of (3.3) can be performed to relate the image output to the GCW-SAR ambiguity function. Substitution of (3.2) into (3.3) gives

$$\begin{aligned} I(x_m, y_n) = & \int_{\frac{x_m}{v}-\frac{T_L}{2}}^{\frac{x_m}{v}+\frac{T_L}{2}} \int_{vt-\frac{L}{2}}^{vt+\frac{L}{2}} \int_{-\frac{W}{2}}^{\frac{W}{2}} \sigma(x,y) s(t-\frac{2r(t,x,y)}{c}) s^*(t-\frac{2r(t,x_m,y_n)}{c}) \\ & \cdot e^{j\frac{4\pi}{\lambda}(r(t,x_m,y_n)-r(t,x,y))} dydxdt \\ = & \int_{x_m-L}^{x_m+L} \int_{-\frac{W}{2}}^{\frac{W}{2}} \chi_g(x,y,x_m,y_n)\sigma(x,y) dydx \end{aligned} \tag{3.4}$$

where

$$\begin{aligned} \chi_g(x,y,x_m,y_n) = & \int_{\frac{x_m}{v}-\frac{T_L}{2}}^{\frac{x_m}{v}+\frac{T_L}{2}} s(t-\frac{2r(t,x,y)}{c}) s^*(t-\frac{2r(t,x_m,y_n)}{c}) \\ & e^{j\frac{4\pi}{\lambda}(r(t,x_m,y_n)-r(t,x,y))} dt \end{aligned} \tag{3.5}$$

is the GCW-SAR ambiguity function of the point (x, y), which can be considered as a weighting function on the RCS $\sigma(x, y)$.

With the slow time sampling in azimuth, the range and azimuth resolutions in conventional SARs have been derived in the chapter 2. However, under the one-dimensional data structure without slow time involved, the derivation of the range and azimuth resolutions requires a different approach, which is provided as follows.

Firstly, the slant range defined in (3.1) can be approximated as

$$r = \sqrt{R(y)^2 + (x-vt)^2} \approx R(y) + \frac{(x-vt)^2}{2R(y)}, t \in [\frac{x}{v} - \frac{T_L}{2}, \frac{x}{v} + \frac{T_L}{2}] \tag{3.6}$$

where $R(y) = \sqrt{(R_c sin\theta + y)^2 + h_0^2}$, which is valid when $|x - vt| \ll R(y)$ is satisfied. Since the received echoes are the far-field reflections, and the slant range for any pixel satisfies the condition $r(t + x_m/v, x_m, y_n) = r(t, 0, y_n)$, the ambiguity function of an arbitrary point (x_m, y_n) can be related to the one of the origin $(0, 0)$. For simplicity, only the ambiguity function at the origin, $\chi_g(0, 0, x_m, y_n)$, is considered, which can be expressed as

$$\begin{aligned} &\chi_g(0,0,x_m,y_n) \\ &= \int_{-\frac{T_L}{2}}^{\frac{T_L}{2}} s(t - \frac{2r(t,0,0)}{c}) s^*(t - \frac{2r(t,x_m,y_n)}{c}) e^{j\frac{4\pi}{\lambda}(r(t,x_m,y_n) - r(t,0,0))} dt \\ &\approx \int_{-\frac{T_L}{2}}^{\frac{T_L}{2}} s(t + \frac{2(r(t,x_m,y_n) - r(t,0,0))}{c}) s^*(t) e^{j\frac{4\pi}{\lambda}(r(t,x_m,y_n) - r(t,0,0))} dt. \end{aligned} \tag{3.7}$$

It is apparent that the ambiguity function closely relates to the range difference $r(t, x_m, y_n) - r(t, 0, 0)$. In this section, two cases of the ambiguity function $\chi_g(0, 0, 0, y_n)$ and $\chi_g(0, 0, x_m, 0)$ are considered respectively: the first one indicates the range resolution and the second one indicates the azimuth resolution.

- *Range Resolution*: When $x_m = 0$, $r(t, 0, y_n) - r(t, 0, 0) \approx (R(y_n) - R_c)(1 - v^2t^2/(2R(y_n)R_c)) \approx R(y_n) - R_c$ since the term $v^2t^2/(2R(y_n)R_c)$ can be neglected as $R_c >> L$. Eq. (3.7) can then be expressed as

$$\chi_g(0,0,0,y_n) \approx e^{j\frac{4\pi}{\lambda}(R(y_n) - R_c)} \int_{-\frac{T}{2}}^{\frac{T}{2}} s(t + \frac{2(R(y_n) - R_c)}{c}) s^*(t) dt. \tag{3.8}$$

Assuming that $s(t)$ is any normalized low pass baseband signal, $\int_{-\frac{T_L}{2}}^{\frac{T_L}{2}} |s(t)|^2 dt = 1$, with constant energy spectrum in its bandwidth B, its auto-correlation function will be a sinc function. Consequently, Eq. (3.8) can be further expressed as

$$\chi_g(0,0,0,y_n) \approx e^{j\frac{4\pi}{\lambda}(R(y_n)-R_c)} \frac{sin(\pi\frac{2B}{c}(R(y_n)-R_c))}{\pi\frac{2B}{c}(R(y_n)-R_c)}. \tag{3.9}$$

The range resolution δ_y is determined by $R(y_n) - R_c = \frac{c}{2B}$ which is the first null point in the ambiguity function. Given that the beam incident angle is θ,

$$\delta_y = \frac{c}{2Bsin\theta}. \tag{3.10}$$

- *Azimuth Resolution*: When $y_n = 0$, the range difference can be approximated as $r(t,x,0) - r(t,0,0) \approx (x^2 - 2vxt)/(2R_c)$ and the ambiguity function can be expressed as

$$\begin{aligned}\chi_g(0,0,x_m,0) &\approx \int_{-\frac{T_L}{2}}^{\frac{T_L}{2}} e^{j\frac{4\pi}{\lambda}\frac{x_m^2-2vx_mt}{2R_c}} s(t + \frac{x_m^2 - 2vx_mt}{cR_c}) s^*(t) dt \\ &= \int_{-\frac{T_L}{2}}^{\frac{T_L}{2}} e^{j\frac{4\pi}{\lambda}\frac{x_m^2-2vx_mt}{2R_c}} s(t + \frac{1}{f_c}\frac{x_m^2 - 2vx_mt}{\lambda R_c}) s^*(t) dt\end{aligned} \tag{3.11}$$

where $f_c = c/\lambda$ is the carrier frequency. Assuming that $s(t)$ is a normalized phase only signal, $s(t) = \frac{1}{\sqrt{T_L}} e^{j\phi(t)}$, Eq. (3.11) can be simplified as

$$\begin{aligned}\chi_g(0,0,x_m,0) &= \frac{1}{T_L}\int_{-\frac{T_L}{2}}^{\frac{T_L}{2}} e^{j\frac{4\pi}{\lambda}\frac{x_m^2-2vx_mt}{2R_c}} e^{j(\phi(t+\frac{1}{f_c}\frac{x_m^2-2vx_mt}{\lambda R_c})-\phi(t))} dt \\ &\approx \frac{1}{T_L}\int_{-\frac{T_L}{2}}^{\frac{T_L}{2}} e^{j2\pi\frac{x_m^2-2vx_mt}{\lambda R_c}} e^{j\phi'(t)\frac{1}{f_c}\frac{x_m^2-2vx_mt}{\lambda R_c}} dt \\ &= \frac{1}{T_L}\int_{-\frac{T_L}{2}}^{\frac{T_L}{2}} e^{j2\pi\frac{x_m^2-2vx_mt}{\lambda R_c}(1+\frac{\phi'(t)}{2\pi f_c})} dt \\ &\approx \frac{1}{T_L}\int_{-\frac{T_L}{2}}^{\frac{T_L}{2}} e^{j2\pi\frac{x_m^2-2vx_mt}{\lambda R_c}} dt = e^{j\frac{2\pi x_m^2}{\lambda R_c}} \frac{sin(\pi\frac{2L}{\lambda R_c}x_m)}{\pi\frac{2L}{\lambda R_c}x_m}\end{aligned} \tag{3.12}$$

where $\phi'(t)$ is the first order derivative of $\phi(t)$. Because $2\pi f_c$ is far larger than the maximum $\phi'(t)$ which is less than $2\pi B$, $\frac{\phi'(t)}{2\pi f_c}$ is neglected in deriving (3.12).

The azimuth resolution δ_x is determined by $x_m = \frac{\lambda R_c}{2L}$ which is the first null point in the ambiguity function and hence

$$\delta_x = \frac{\lambda R_c}{2L} = \frac{L_a}{2} \tag{3.13}$$

where $\lambda R_c/L$ is equal to the antenna aperture L_a.

Though the range and azimuth resolutions of the GCW-SAR are the same as those of the conventional pulsed SAR and FMCW-SAR respectively, the above analysis clearly shows the requirements of the transmitted signal, i.e., a constant energy spectrum in the frequency domain and a constant signal envelope in the time domain, under which the range and azimuth resolutions are bounded by (3.10) and (3.13) respectively. The removal of slow time sampling enables great flexibility in signal waveform design.

3.4 Piecewise Constant Doppler Algorithm

According to the general image reconstruction described in the second section of this chapter, integration over the entire synthetic aperture time is necessary for each pixel in the GCW-SAR image. As the amount of pixels in a high resolution and wide swath image is significant, the direct implementation of the algorithm leads to a great computational complexity. However, existing fast imaging algorithms designed for back-projection algorithm (BPA) [69, 70, 71, 72, 73] are not applicable to GCW-SAR, since they depend on the two-dimensional raw data structure and also involve slow time sampling in azimuth under the stop-and-go assumption. In this section, to develop a novel fast imaging algorithm well suited for GCW-SAR, the relationships between the correlations of the adjacent pixels in azimuth direction are analyzed and a complexity reduced approach, i.e., PCD algorithm, is designed, which can calculate the correlation recursively after applying piecewise linear approximation to the range curve.

3.4.1 Principle

The time delay of the received signal from an imaging point changes in response to its slant range. Assuming that the platform is moving at a constant speed in a straight line, the variation of the slant range is equal to a quadratic curve. In order to deal with this nonlinearity, this curve can be divided into multiple linear segments linked end to end. Therefore, the Doppler frequency shift in each segment can be considered as a constant. According to (3.3), the image $I(x_m, y_n)$ of the pixel (x_m, y_n) involves integration over an entire synthetic aperture time $[-T_L/2 + x_m/v, T_L/2 + x_m/v]$. If we divide the time interval $[-T_L/2, T_L/2]$ into P segments with a length of T_P and define the time instants at the two ends of the interval as well as the segment joint points as $t_p = pT_P - T_L/2$ for $p = 0, 1, ..., P$, the pth segment of the synthetic aperture time can be denoted as $(x_m/v + t_p, x_m/v + t_{p+1}]$ and the corresponding correlation value over this time interval can be calculated as

$$I_p(x_m, y_n) = \int_{\frac{x_m}{v}+t_p}^{\frac{x_m}{v}+t_{p+1}} s_r(t)s^*(t - \frac{2r(t, x_m, y_n)}{c})e^{j\frac{4\pi}{\lambda}r(t,x_m,y_n)}dt. \tag{3.14}$$

The image $I(x_m, y_n)$ of the pixel (x_m, y_n) is thus expressed as

$$I(x_m, y_n) = \sum_{p=0}^{P-1} I_p(x_m, y_n). \tag{3.15}$$

Now, the correlation value $I_p(x_m + \Delta x, y_n)$ over the pth segment of a synthetic aperture time for the image point $(x_m+\Delta x, y_n)$ in relation to $I_p(x_m, y_n)$ is derived. In this segment, the received echo from the image point $(x_m+\Delta x, y_n)$ is made up of two parts: the first one is received during the time interval $(x_m/v+\Delta x/v+t_p, x_m/v+t_{p+1}]$ which is also used to calculate $I_p(x_m, y_n)$; the second one is received during the time interval $(x_m/v + t_{p+1}, x_m/v + \Delta x/v + t_{p+1}]$. Since $r(t + x/v, x, y) = r(t, 0, y)$, the image $I_p(x_m + \Delta x, y_n)$ can be expressed as

$$\begin{aligned} I_p(x_m + \Delta x, y_n) = &\int_{\frac{x_m}{v}+\frac{\Delta x}{v}+t_p}^{\frac{x_m}{v}+t_{p+1}} s_r(t)s^*(t - \frac{2r(t, x_m + \Delta x, y_n)}{c})e^{j\frac{4\pi}{\lambda}r(t,x_m+\Delta x,y_n)}dt \\ &+ \int_{\frac{x_m}{v}+t_{p+1}}^{\frac{x_m}{v}+\frac{\Delta x}{v}+t_{p+1}} s_r(t)s^*(t - \frac{2r(t, x_m + \Delta x, y_n)}{c})e^{j\frac{4\pi}{\lambda}r(t,x_m+\Delta x,y_n)}dt \\ = &\int_{\frac{\Delta x}{v}+t_p}^{t_{p+1}} s_r(t + \frac{x_m}{v})s^*(t + \frac{x_m}{v} - \frac{2r(t, \Delta x, y_n)}{c})e^{j\frac{4\pi}{\lambda}r(t,\Delta x,y_n)}dt \\ &+ \int_{t_{p+1}}^{\frac{\Delta x}{v}+t_{p+1}} s_r(t + \frac{x_m}{v})s^*(t + \frac{x_m}{v} - \frac{2r(t, \Delta x, y_n)}{c})e^{j\frac{4\pi}{\lambda}r(t,\Delta x,y_n)}dt. \end{aligned} \tag{3.16}$$

The slant range in the pth segment can be approximated as a linear function of t as

$$\begin{aligned} &\widetilde{r}(t, \Delta x, y_n) \\ &= r(t_p + \frac{\Delta x}{v}, \Delta x, y_n) + \frac{r(t_{p+1} + \frac{\Delta x}{v}, \Delta x, y_n) - r(t_p + \frac{\Delta x}{v}, \Delta x, y_n)}{t_{p+1} - t_p}(t - t_p - \frac{\Delta x}{v}) \\ &= r(t_p, 0, y_n) - \frac{\lambda}{2}f_{D_p}(y_n)(t - t_p - \frac{\Delta x}{v}) \\ &= \widetilde{r}(t, 0, y_n) + \frac{\lambda}{2}f_{D_p}(y_n)\frac{\Delta x}{v} \end{aligned} \tag{3.17}$$

where $f_{D_p}(y_n) = -2/\lambda \cdot (r(t_{p+1}, 0, y_n) - r(t_p, 0, y_n))/(t_{p+1} - t_p)$ is defined as the constant Doppler frequency shift for segment p. For the same $R(y_n)$, the time delay difference in the baseband reference signal between two adjacent pixels (x_m, y_n) and $(x_m + \Delta x, y_n)$ can be neglected since $|x - vt| << R(y_n)$, indicating $s^*(t + \frac{x_m}{v} - \frac{2r(t,\Delta x,y_n)}{c}) \approx s^*(t + \frac{x_m}{v} - \frac{2r(t,0,y_n)}{c})$. Eq. (3.16) thus can be re-written as

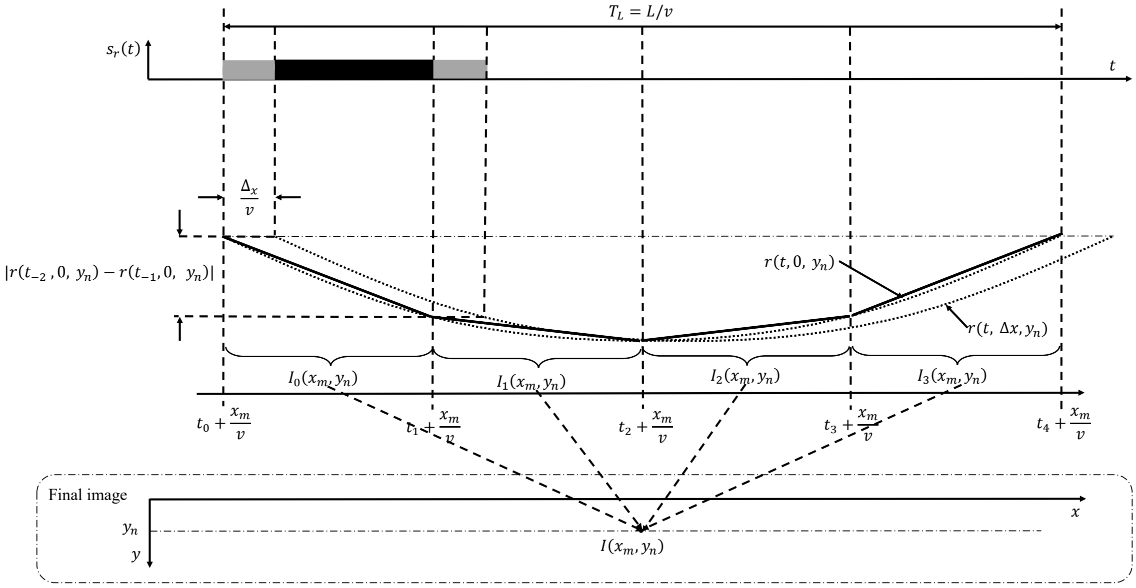

Figure 3.2 : Segmentation, linearization and their relationship with image reconstruction.

$$
\begin{aligned}
& I_p(x_m + \Delta x, y_n) \\
&= \int_{t_p}^{t_{p+1}} s_r(t + \frac{x_m}{v}) s^*(t + \frac{x_m}{v} - \frac{2\widetilde{r}(t, \Delta x, y_n)}{c}) e^{j\frac{4\pi}{\lambda}\widetilde{r}(t, \Delta x, y_n)} dt \\
&- \int_{t_p}^{\frac{\Delta x}{v} + t_p} s_r(t + \frac{x_m}{v}) s^*(t + \frac{x_m}{v} - \frac{2\widetilde{r}(t, \Delta x, y_n)}{c}) e^{j\frac{4\pi}{\lambda}\widetilde{r}(t, \Delta x, y_n)} dt \\
&+ \int_{t_{p+1}}^{\frac{\Delta x}{v} + t_{p+1}} s_r(t + \frac{x_m}{v}) s^*(t + \frac{x_m}{v} - \frac{2\widetilde{r}(t, \Delta x, y_n)}{c}) e^{j\frac{4\pi}{\lambda}\widetilde{r}(t, \Delta x, y_n)} dt \\
&= \int_{t_p}^{t_{p+1}} s_r(t + \frac{x_m}{v}) s^*(t + \frac{x_m}{v} - \frac{2\widetilde{r}(t, 0, y_n)}{c}) e^{j\frac{4\pi}{\lambda}(\widetilde{r}(t, 0, y_n) + \frac{\lambda}{2} f_{D_p}(y_n) \frac{\Delta x}{v})} dt \\
&- \int_{t_p}^{\frac{\Delta x}{v} + t_p} s_r(t + \frac{x_m}{v}) s^*(t + \frac{x_m}{v} - \frac{2\widetilde{r}(t, \Delta x, y_n)}{c}) e^{j\frac{4\pi}{\lambda}\widetilde{r}(t, \Delta x, y_n)} dt \\
&+ \int_{t_{p+1}}^{\frac{\Delta x}{v} + t_{p+1}} s_r(t + \frac{x_m}{v}) s^*(t + \frac{x_m}{v} - \frac{2\widetilde{r}(t, \Delta x, y_n)}{c}) e^{j\frac{4\pi}{\lambda}\widetilde{r}(t, \Delta x, y_n)} dt \\
&= I_p(x_m, y_n) e^{j2\pi f_{D_p}(y_n) \frac{\Delta x}{v}} \\
&- \int_{0}^{\frac{\Delta x}{v}} s_r(t + t_p + \frac{x_m}{v}) s^*(t + t_p + \frac{x_m}{v} - \frac{2\widetilde{r}(t + t_p, \Delta x, y_n)}{c}) e^{j\frac{4\pi}{\lambda}\widetilde{r}(t + t_p, \Delta x, y_n)} dt \\
&+ \int_{0}^{\frac{\Delta x}{v}} s_r(t + t_{p+1} + \frac{x_m}{v}) s^*(t + t_{p+1} + \frac{x_m}{v} - \frac{2\widetilde{r}(t + t_{p+1}, \Delta x, y_n)}{c}) e^{j\frac{4\pi}{\lambda}\widetilde{r}(t + t_{p+1}, \Delta x, y_n)} dt.
\end{aligned}
\tag{3.18}
$$

Taking $P = 4$ as an example, the segmentation, linearization and their relationship with the image reconstruction are shown in Fig. 3.2. The dotted curves indicate the slant ranges of the pixels (x_m, y_n) and $(x_m + \Delta x, y_n)$ respectively, which are approximated as the solid linear segments. In a segment p, the recursive imaging process is explained as follows:

- Assume that the correlation $I_p(x_m, y_n)$ in the interval $(t_p + x_m/v, t_{p+1} + x_m/v]$ has been obtained for the pixel (x_m, y_n). To calculate the correlation in the integration interval $(t_p + x_m/v + \Delta x/v, t_{p+1} + x_m/v + \Delta x/v]$ for the pixel $(x_m + \Delta x, y_n)$, the Doppler frequency shift in the previously calculated $I_p(x_m, y_n)$ is firstly compensated, which is achieved by multiplying $I_p(x_m, y_n)$ by $e^{j2\pi f_{Dp}(y_n)\Delta x/v}$.
- The second step is to remove the correlation obtained in the interval $(t_p + x_m/v, t_p + x_m/v + \Delta x/v]$ for the pixel (x_m, y_n).
- Finally, add new signal correlation during the interval $(t_{p+1} + x_m/v, t_{p+1} + x_m/v + \Delta x/v]$ to obtain $I_p(x_m + \Delta x, y_n)$.

3.4.2 Implementation

To ensure the quality of the final image, the number of pixels to $N = 2W/\delta_y$ and $M = L/(T_s v)$ are set in range and azimuth respectively. After the sampling of the demodulated received signal, the data sequence is represented as $s_r(mT_s)$ and the coordinate of the pixel (x_m, y_n) can be rewritten as $(mT_s v, y_n)$, where m indicates the imaging pixel index in azimuth.

Based on (3.18) and letting $\Delta x = T_s v$, the corresponding recursive process is further derived as

$$
\begin{aligned}
&I_p((m+1)T_s v, y_n)\\
&= I_p(mT_s v, y_n)e^{j2\pi f_{D_p}(y_n)T_s} - T_s s_r(mT_s + t_p + T_s)s^*(mT_s + t_p + T_s\\
&- \frac{2r(t_p + T_s, T_s v, y_n)}{c})e^{j\frac{4\pi}{\lambda}r(t_p+T_s,T_s v,y_n)} + T_s s_r(mT_s + t_{p+1} + T_s)s^*(mT_s + t_{p+1} + T_s\\
&- \frac{2r(t_{p+1} + T_s, T_s v, y_n)}{c})e^{j\frac{4\pi}{\lambda}r(t_{p+1}+T_s,T_s v,y_n)}\\
&= I_p(mT_s v, y_n)e^{j2\pi f_{D_p}(y_n)T_s}\\
&- T_s s_r((m+1)T_s + t_p)s^*((m+1)T_s + t_p - \frac{2r(t_p, 0, y_n)}{c})e^{j\frac{4\pi}{\lambda}r(t_p,0,y_n)}\\
&+ T_s s_r((m+1)T_s + t_{p+1})s^*((m+1)T_s + t_{p+1} - \frac{2r(t_{p+1}, 0, y_n)}{c})e^{j\frac{4\pi}{\lambda}r(t_{p+1},0,y_n)}.
\end{aligned}
\tag{3.19}
$$

Taking $P = 4$ as an example, the flow graph of the PCD implemention is shown in Fig. 3. It is seen that, instead of performing correlation for each pixel individually, the PCD algorithm updates the correlation recursively and thus saves much data storage and reduces the computational complexity.

3.4.3 Complexity Analysis

Existing SAR imaging algorithms come in two broad classes: frequency domain methods, e.g., RDA, and BPA. For the sake of comparison, an $N \times N$ final image is reconstructed by using RDA, conventional BPAs and PCD algorithm respectively.

The RDA adopts range and azimuth compressions with phase compensation, e.g., RCMC. The numbers of complex multiplications required for one-dimensional fast Fourier transform (FFT) are $Nlog_2N$ [69]. Hence, the range and azimuth compressions need totally $4N^2log_2N + 2N^2$ complex multiplications, including FFT and inverse FFT. Supposing that the number of complex multiplications required to interpolate one data sample is N_{interp}, the total number of complex multiplications required for the RDA is $4N^2log_2N + N^2 \cdot (N_{interp} + 2)$.

The conventional BPA reconstructs each pixel of the SAR image individually

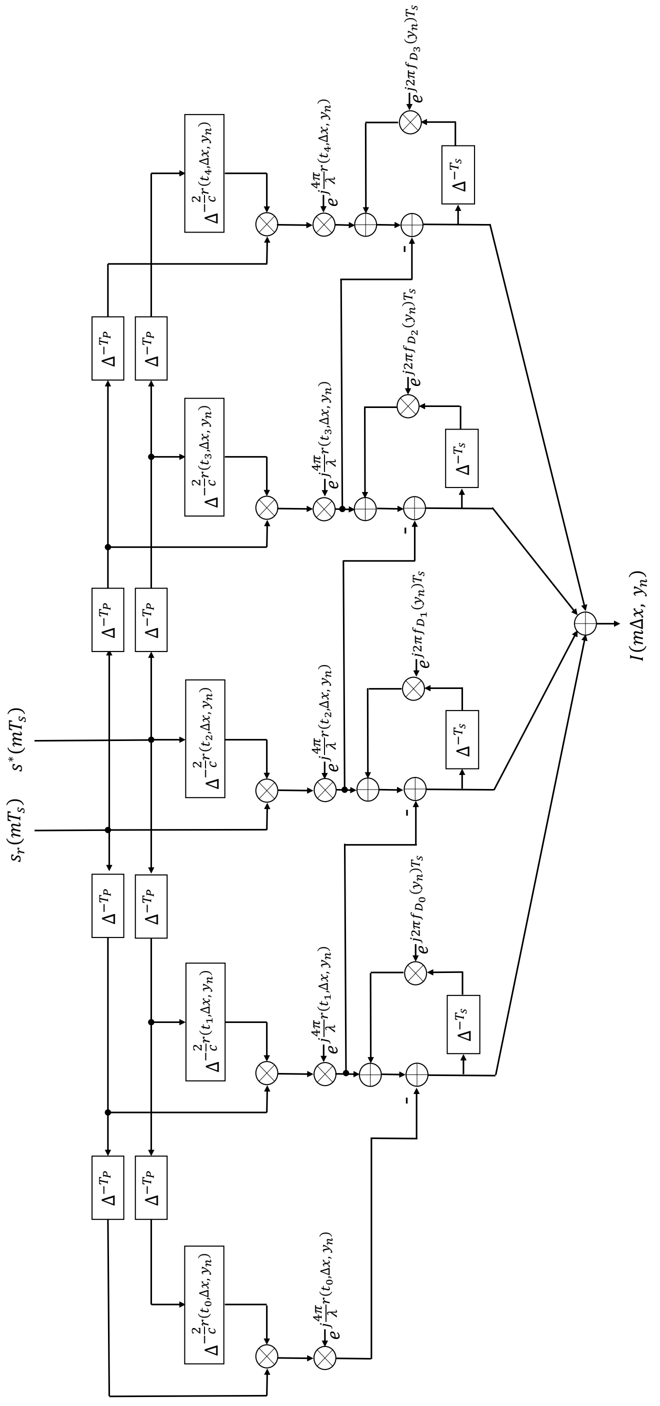

Figure 3.3 : Flow graph of PCD implementation for a given y_n, where the $\Delta^{\pm\tau}$ denotes time delay or advance by τ.

from the range compressed SAR data. The RCS of each image pixel can be obtained by the correlation over the synthetic aperture, thus the azimuth compression consists of N complex multiplications. Considering the interpolation of data, the total number of complex multiplications required to reconstruct an $N \times N$ final image is $2N^2 log_2 N + N^3 + N^2 \cdot (N_{interp} + 1)$.

The PCD algorithm updates the correlation recursively. After the correlation for the first pixel, each pixel in azimuth only needs $3P + 2$ complex multiplications as shown in Fig. 3. Considering that GCW-SAR adopts the CW transmit signal, the number of complex multiplications required to reconstruct an $N \times N$ final image is $(3P + 2) \cdot N^2$. Note that the $N \times N$ final image is much smaller in terms of physical area than that of pulsed SAR due to the sample-by-sample recursion. To reconstruct the image of the same area, the GCW-SAR system requires $(3P + 2) \cdot N^3$ complex multiplications assuming that one synthetic aperture time has N^2 samples. However, a decimated PCD algorithm which performs recursion over multiple samples can be developed to reduce the complexity. By further exploring the signal correlation in range direction, the complexity of the PCD algorithm can be reduced to a level similar to that of BPA. This work is out of the scope of this dissertation and will be reported separately.

3.5 Decimated PCD Algorithm

In PCD algorithm, the image pixels in azimuth direction are reconstructed recursively with a spacing equivalent to the signal sampling period T_s, i.e., $\Delta x = T_s v$. Since the azimuth sampling rate is much larger than the Doppler frequency bandwidth, the image spacing in azimuth direction is much shorter than the azimuth resolution, leading to a large amount of redundant image points and hence significant computational cost. In this section, a faster algorithm is designed to extend the PCD image spacing in azimuth.

3.5.1 Decimated PCD Principle

To remove the redundant imaging pixels, the imaging spacing Δx can be extended corresponding to multiple sampling periods, resulting in a decimated PCD algorithm. Further take the zero-th order approximation on top of the linear segments of the slant range as shown in Fig. 3.4 (a). The approximated slant range curves $\widetilde{r}(t, x_m, y_n)$ and $\hat{r}(t, x_m, y_n)$ during $[t_p, t_{p+1})$ for PCD and decimated PCD algorithms are shown respectively using the dash and solid lines. Just as in the conventional SAR imaging, the azimuth image spacing Δx can be as large as that corresponding to a PRI.

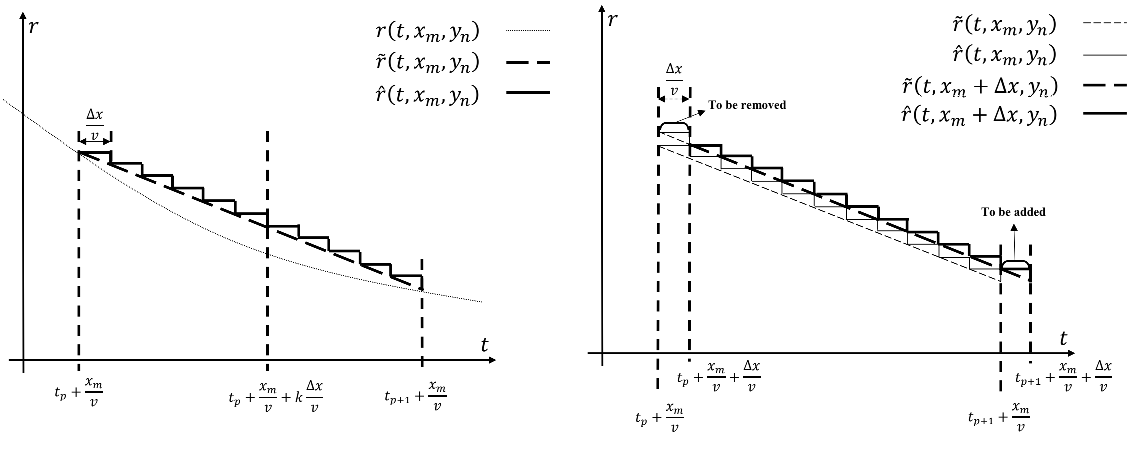

(a) (b)

Figure 3.4 : Decimated PCD imaging: (a) slant range approximation; (b) recursive imaging process from x_m/v to $(x_m + \Delta x)/v$.

The recursive imaging process of the decimated PCD algorithm is shown in Fig. 3.4 (b). Note that after the further zero-th order slant range approximation the Doppler frequency shift remains the same since $\hat{r}(t, x_m, y_n) - \hat{r}(t, x_m + \Delta x, y_n) = \widetilde{r}(t, x_m, y_n) - \widetilde{r}(t, x_m + \Delta x, y_n)$, and that the slant range can be considered as a constant over the integration interval $[0, \Delta x/v)$, i.e., $\hat{r}(t + t_p, \Delta x, y_n) = r(t_p, \Delta x, y_n)$. Therefore, from (3.18), the p-th segment of the image $I_p(x_m + \Delta x, y_n)$ can be expressed as

$$\begin{aligned}
&I_p(x_m + \Delta x, y_n) \\
&= I_p(x_m, y_n) e^{j2\pi f_{D_p}(y_n)\frac{\Delta x}{v}} \\
&- \int_0^{\frac{\Delta x}{v}} s_r(t + t_p + \frac{x_m}{v}) s^*(t + t_p + \frac{x_m}{v} - \frac{2\hat{r}(t + t_p, \Delta x, y_n)}{c}) e^{j\frac{4\pi}{\lambda}\hat{r}(t+t_p,\Delta x,y_n)} dt \\
&+ \int_0^{\frac{\Delta x}{v}} s_r(t + t_{p+1} + \frac{x_m}{v}) s^*(t + t_{p+1} + \frac{x_m}{v} - \frac{\hat{r}(t + t_{p+1}, \Delta x, y_n)}{c}) e^{j\frac{4\pi}{\lambda}\hat{r}(t+t_{p+1},\Delta x,y_n)} dt \\
&= \hat{I}_1^{(p)}(x_m, y_n) e^{j2\pi f_{D_p}(y_n)\frac{\Delta x}{v}} \\
&- e^{j\frac{4\pi}{\lambda} r(t_p,\Delta x,y_n)} \int_0^{\frac{\Delta x}{v}} s_r(t + t_p + \frac{x_m}{v}) s^*(t + t_p + \frac{x_m}{v} - \frac{2r(t_p, \Delta x, y_n)}{c}) dt \\
&+ e^{j\frac{4\pi}{\lambda} r(t_{p+1},\Delta x,y_n)} \int_0^{\frac{\Delta x}{v}} s_r(t + t_{p+1} + \frac{x_m}{v}) s^*(t + t_{p+1} + \frac{x_m}{v} - \frac{2r(t_{p+1}, \Delta x, y_n)}{c}) dt.
\end{aligned} \tag{3.20}$$

It is worthwhile noting that the zero-th order approximation is used in the decimated PCD imaging for reducing the complexity. It has nothing to do with PRI or slow time as in the conventional SAR imaging. The concept of PRI or slow time is no longer valid in any PCD imaging.

3.5.2 Decimated PCD Implementation

Assuming that each linear segment is further divided into K constant segments in the decimated PCD imaging, the imaging spacing Δx can be extended from $T_s v$ to $(T_P v)/K = N_s T_s v$, where $N_s = T_P/(T_s K)$ is the number of received samples over each constant segment. The image azimuth coordinate can be expressed as $x_m = m\Delta x$ where m is an integer index describing the image pixel location in azimuth.

Replacing the integration over $[0, \Delta x/v)$ in (3.20) by a sum of N_s discrete signal

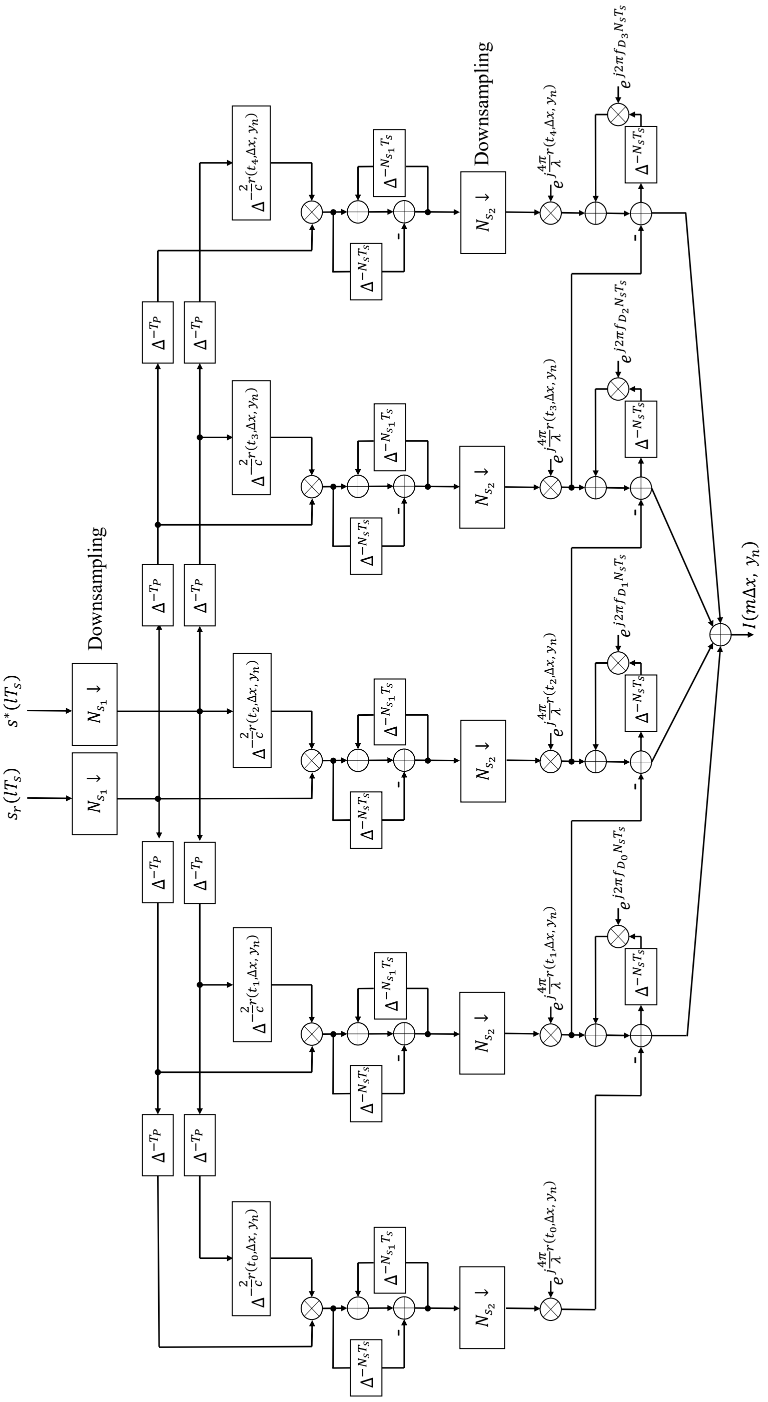

Figure 3.5 : Flow graph of decimated PCD algorithm for a given y_n, where $\Delta^{\pm\tau}$ denotes time delay or advance by τ, $l = i + mN_s$ denotes signal sampling time index, and m is the image azimuth sampling index.

samples, the recursive process can be expressed as

$$\begin{aligned}
&\hat{I}_1^{(p)}((m+1)\Delta x, y_n) \\
&= \hat{I}_1^{(p)}(m\Delta x, y_n)e^{j2\pi f_{D_p}(y_n)N_s T_s} \\
&- e^{j\frac{4\pi}{\lambda}r(t_p,\Delta x,y_n)}T_s\sum_{i=1}^{N_s} s_r((i+mN_s)T_s+t_p)s^*((i+mN_s)T_s+t_p-\frac{2r(t_p,\Delta x,y_n)}{c}) \\
&+ e^{j\frac{4\pi}{\lambda}r(t_{p+1},\Delta x,y_n)}T_s\sum_{i=1}^{N_s} s_r((i+mN_s)T_s+t_{p+1}) \\
&\cdot s^*((i+mN_s)T_s+t_{p+1}-\frac{2r(t_{p+1},\Delta x,y_n)}{c}).
\end{aligned} \tag{3.21}$$

Furthermore, the received and reference signals can be downsampled by a factor N_{s_1}. Hence, the number of samples involved in the summations can be reduced to $N_{s_2} = \frac{N_s}{N_{s_1}}$ and Eq. (3.21) can be further expressed as

$$\begin{aligned}
&\hat{I}_1^{(p)}((m+1)\Delta x, y_n) \\
&= \hat{I}_1^{(p)}(m\Delta x, y_n)e^{j2\pi f_{D_p}(y_n)N_s T_s} \\
&- e^{j\frac{4\pi}{\lambda}r(t_p,\Delta x,y_n)}N_{s_1}T_s\sum_{i=1}^{N_{s_2}} s_r((i+mN_{s_2})N_{s_1}T_s+t_p)s^*((i+mN_{s_2})N_{s_1}T_s+t_p \\
&- \frac{2r(t_p,\Delta x,y_n)}{c}) + e^{j\frac{4\pi}{\lambda}r(t_{p+1},\Delta x,y_n)}N_{s_1}T_s\sum_{i=1}^{N_{s_2}} s_r((i+mN_{s_2})N_{s_1}T_s+t_{p+1}) \\
&s^*((i+mN_{s_2})N_{s_1}T_s+t_{p+1}-\frac{2r(t_{p+1},\Delta x,y_n)}{c})
\end{aligned} \tag{3.22}$$

where the number of complex multiplications are reduced by N_{s_1} times.

Taking $P = 4$ as an example, the flow graph of the decimated PCD algorithm is drawn based on (3.22) as shown in Fig. 3.5. Obviously, after extending the image spacing in azimuth by N_s times, the computational cost is largely reduced compared with the original PCD algorithm which is the special case of $N_s = 1$.

3.5.3 Complexity Analysis

For easy comparison purpose, the same observed scene is reconstructed by using PCD and decimated PCD algorithm respectively. It is also assumed that there are N^2 samples within a sweep of the observed area and the number of range pixels is N.

The PCD algorithm updates the image in azimuth recursively whenever the system obtains a new demodulated sample, thus achieving an $N \times N^2$ pixel image over the observed scene. Each image point in azimuth needs $3P + 2$ complex multiplications, and thus the PCD algorithm requires $(3P + 2) \times N^3$ complex multiplications.

However, after extending the azimuth imaging spacing, the decimated PCD algorithm only achieves an $N \times N^2/N_s$ pixel image and only uses part of the samples when $N_{s_1} > 1$, thus the computational cost is largely reduced. As seen in Fig. 3.5, the number of samples in azimuth has been reduced to N^2/N_{s_1} after the first donwsampling, hence the decimated PCD algorithm only requires $(P+1) \cdot N \cdot N^2/N_{s_1}$ complex multiplications before the second downsampling. After the second downsampling, the recursion needs further $(2P + 1)N^3/N_s$ complex multiplications. Therefore, the total computational complexity can be finally reduced to $(P + 1) \cdot N^3/N_{s_1} + (2P + 1)N^3/N_s$.

Table 3.1 : Complexity Comparison

SAR Imaging Algorthm	Number of Complex Multiplication
BPA	$2N^2 log_2 N + N^3 + N^2 \cdot (N_{interp} + 1)$
RDA	$4N^2 log_2 N + N^2 \cdot (N_{interp} + 2)$
PCD	$(3P + 2) \times N^3$
Decimated PCD	$(P + 1) \cdot N^3/N_{s_1} + (2P + 1)N^3/N_s$

Table 3.1 shows the complexity comparison between the conventional SAR imaging and PCD imaging. It is seen that the number of the complex multiplication in the decimated PCD imaging can be reduced to a level similar to that of BPA. Due to the recursive imaging in azimuth, the range imaging can be done in parallel and well suited for field-programmable gate array (FPGA) or graphics processing unit (GPU) based implementation. Therefore, the decimated PCD imaging can be achieved as fast as the RDA.

3.6 Simulation Results

In this section, the GCW-SAR performance is evaluated in an airborne simulation scenario and compared with conventional FMCW-SAR, both using periodic chirp signals as the transmitted signals. Denote $N_r = T_L/T_r$ as the number of chirp periods over the aperture time T_L, where T_r is the period of the chirp signal. The FMCW-SAR and the GCW-SAR are assumed to operate in the same stripmap mode with the following airborne SAR parameters [66, 67]: carrier frequency 10 GHz, speed of radar platform 70 m/s, platfrom altitude 7000 m, antenna aperture 0.9 m, and $R_c = 8083$ m. Moreover, the y and x coordinates are normalized by the range and azimuth resolutions δ_y and δ_x respectively.

3.6.1 Anti-Self-interference Performance in Digital Domain

Due to the FD operation in the GCW-SAR, the interference from the transmitted signal will impact on the imaging performance. Assuming that sufficient self-interference cancellation can be achieved by using existing joint propagation domain and analog-circuit domain cancellation techniques so that the reflected signal and self-interference are received within the ADC dynamic range. only the residual self-interference in digital domain is considered in this subsection.

To analyze the anti-self-interference performance, the received signal with self-interference can be simply expressed as

$$s_{si}(t) = s_r(t) + \int_0^{\tau_g} g(\tau) \cdot s(t-\tau) e^{-j\frac{4\pi}{\lambda}\tau c} d\tau \tag{3.23}$$

where $g(t)$ and τ_g denote the interference channel impulse response and the maximum time delay of the self-interference respectively. When reconstructing the image for a point (x_m, y_n) in the beam footprint, the output of the matched filter can be expressed as

$$\begin{aligned} & I_{si}(x_m, y_n) \\ & = I(x_m, y_n) + \int_0^{\tau_g} g(\tau) \int_{\frac{x_m}{v}-\frac{T}{2}}^{\frac{x_m}{v}+\frac{T}{2}} s(t-\tau) s^*(t - \frac{2r(t, x_m, y_n)}{c}) e^{j\frac{4\pi}{\lambda}(r(t, x_m, y_n) - c\tau)} dt d\tau. \end{aligned} \tag{3.24}$$

The integral with regard to t, $\int_{\frac{x_m}{v}-\frac{T}{2}}^{\frac{x_m}{v}+\frac{T}{2}} s(t-\tau) s^*(t - \frac{2r(t,x_m,y_n)}{c}) e^{j\frac{4\pi}{\lambda}(r(t,x_m,y_n)-c\tau)} dt$, represents an ambiguity function of a hypothetical point scatterer with range $0 < \frac{1}{2}c\tau < \frac{1}{2}c\tau_g$. Since $\frac{1}{2}c\tau_g$ is much smaller than the slant range $r(t, x_m, y_n)$, only small sidelobes of the ambiguity function will be superimposed on $I(x_m, y_n)$.

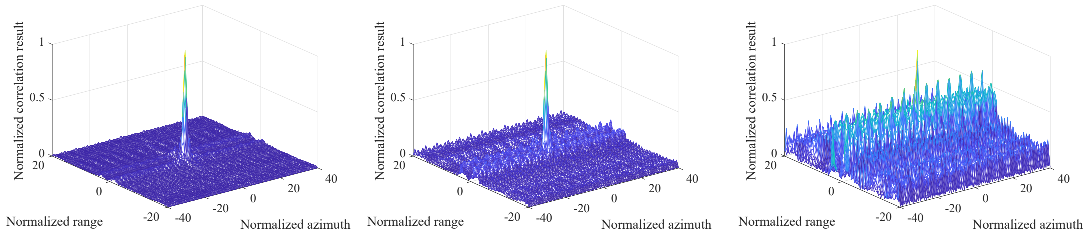

(a) (b) (c)

Figure 3.6 : SIR performance in an airborne GCW-SAR: (a), (b), and (c) show the GCW-SAR images of a point scatterer with PCD algorithm at SIR=$-45dB$, $-55dB$, and $-65dB$ respectively.

In the first simulation experiment, the impact of the self-interference on the GCW-SAR imaging performance is investigated. Firstly, we define the signal to interference power ratio as

$$SIR = 10 \cdot log_{10}(\frac{P_r}{P_i}) \tag{3.25}$$

where P_r and P_i are the average powers of the received echoes and the self-interference respectively. Assuming the self-interference directly comes from the transmitter and ignoring the white noise, Fig. 3.6 shows the imaging results for a point at $(0, 0)$ with SIR$=-45dB$, $-55dB$ and $-65dB$ respectively in an airborne platform. It is seen that the GCW-SAR is highly resistant to self-interference. With SIR higher than $-45dB$, the self-interference is negligible. Due to the GCW-SAR's superb anti-self-interference ability, the SIC requirement in a practical system can be surely satisfied even the actual SIC level achieved in the analog-circuit domain is affected by some negative effects such as non-linearity and phase noise in the radar electronics.

3.6.2 Impact of Pulse Repetition Frequency

In the second simulation experiment, how the period of the chirp signal T_r affects the imaging performance is investigated in GCW-SAR and FMCW-SAR respectively. With the radar parameters given at the beginning of this section, the length of the synthetic aperture is almost 600 δ_x, the lowest possible value of PRF is 0.26 Hz since in this case the period T_r is equal to the aperture time T, and the unambiguous PRF for the FMCW-SAR is $78Hz$.

The PRF, which is equal to $1/T_r = N_r/T$, has little impact on azimuth resolution in GCW-SAR but significantly impacts on FMCW-SAR. Fig. 3.7 shows the imaging performance with different PRFs in GCW-SAR and FMCW-SAR systems for a point source located at $(0, 0)$. It is clearly seen that the GCW-SAR performs much better than the FMCW-SAR which adopts the slow time sampling in azimuth. The change in PRF does not affect the azimuth resolution for the GCW-SAR, even in the lowest PRF case as shown in Fig. 3.7 (a). However, in FMCW-SAR, ambiguities

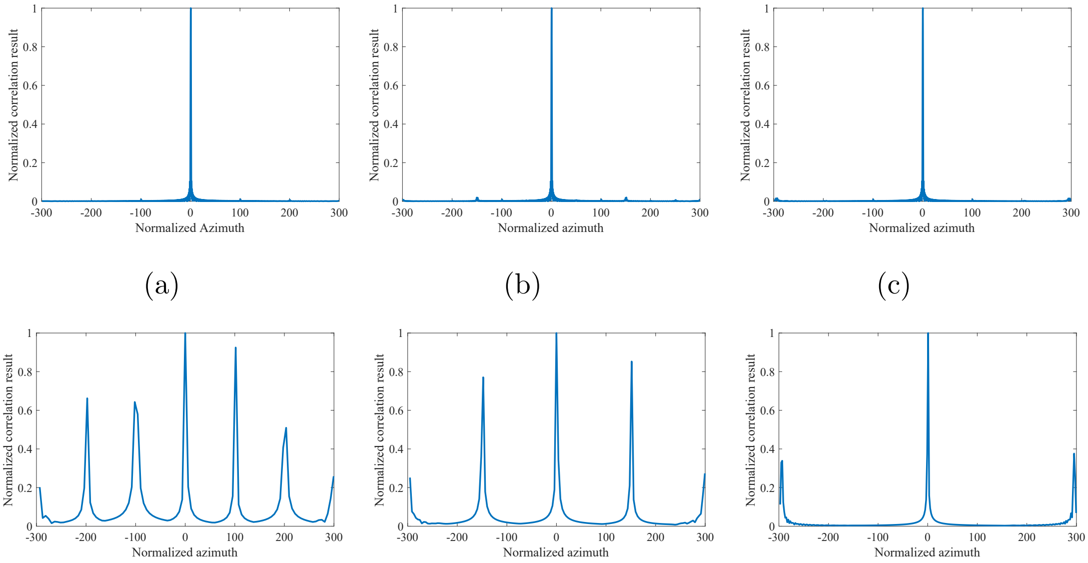

(a) (b) (c)

(d) (e) (f)

Figure 3.7 : Azimuth imaging comparison between GCW-SAR and FMCW-SAR with different PRFs: (a), (b), and (c) show the performance of GCW-SAR with PCD algorithm at $PRF = 0.26Hz$, $39Hz$, and $76.6Hz$ respectively; (d), (e) and (f) show the performance of FMCW-SAR at $PRF = 13Hz$, $39Hz$, and $76.6Hz$ respectively.

will appear when the PRF is less than $78Hz$. For instance, as seen in Fig. 3.7 (c) and 3.7 (f), the two ambiguities show up at $-295\delta_x$ and $295\delta_x$ symmetrically in FMCW-SAR image when the PRF is $76.6Hz$, whereas they are hardly noticeable in the GCW-SAR image. Fig. 3.7 (d) and 3.7 (e) show the low PRF cases in FMCW-SAR where the PRFs are $13Hz$ and $39Hz$ respectively. It is apparent that ambiguities will appear periodically, thus leading to much deteriorated FMCW-SAR images. Therefore, GCW-SAR can break the limitation of minimum antenna area constraint and obtain a wide swath image with high azimuth resolution.

Low PRF may slightly degrade the mainlobe of the ambiguity function in range direction, but as shown in the following simulation, such degradation will be neg-

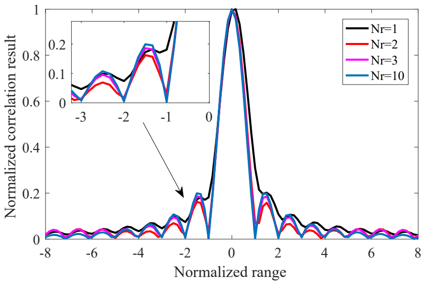

Figure 3.8 : Range resolution with different transmitted repetition interval.

ligible after N_r is larger than 3. With the same one-point imaging setup, Fig. 3.8 shows the image using PCD algorithm with $P = 100$, but different N_r. It is seen that the range resolution is higher when N_r is larger. When N_r is larger than 3, there is no significant improvement any more.

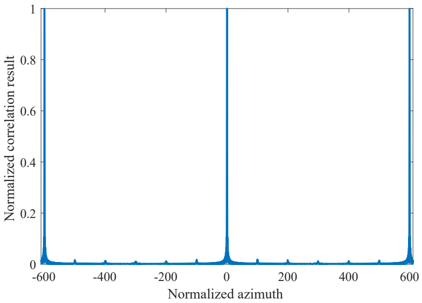

Figure 3.9 : A large image in azimuth.

3.6.3 Large Image Reconstruction in Azimuth

To achieve a large image in azimuth, conventional SAR reconstructs images along the track block by block and then performs image stitching and registration techniques to form a large one. In contrast, GCW-SAR image is reconstructed recursively and such a large image can be achieved directly, thus saving significant operations. For simplicity, only imaging three targets is considered in the azimuth direction and the three targets are located at $-600\delta_x$, 0, and $600\delta_x$ respectively. Both

P and N_r are set to 100. Fig. 3.9 shows the reconstructed GCW-SAR image where x-axis spans from $-610\delta_x$ to $610\delta_x$, almost twice as long as the synthetic aperture. It is evident that the three targets are well distinguished without ambiguities.

3.6.4 Performance of PCD Algorithm

In the fourth simulation experiment, the imaging performance with the ideal matched-filtering based algorithm and the PCD algorithm is compared in GCW-SAR, and investigate the ambiguities caused by linear approximation. The reconstructed images with point targets is shown in Fig. 3.10. N_r is set to 100 in the simulation.

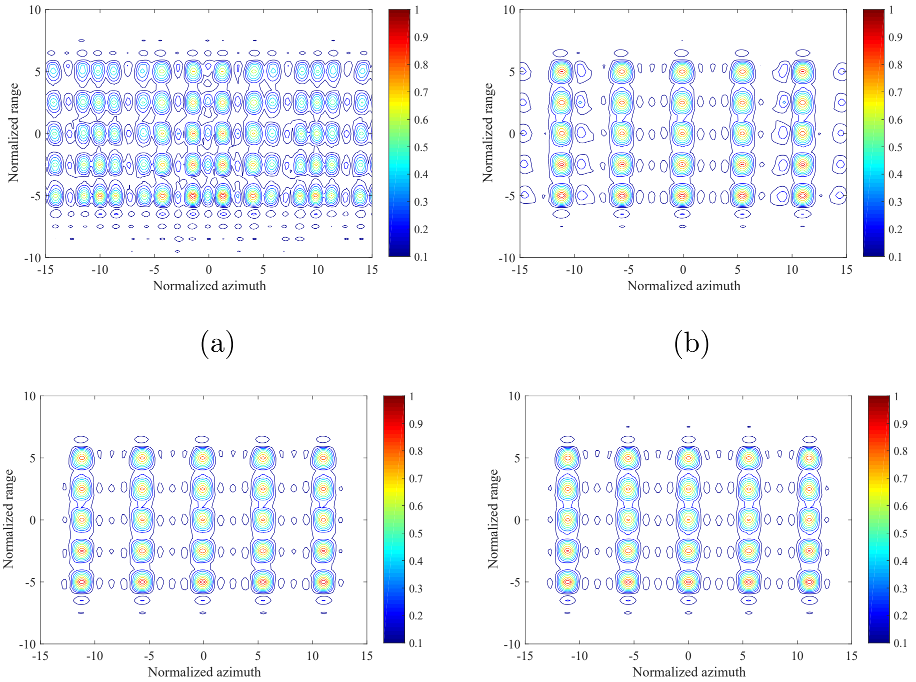

(a)

(b)

(c)

(d)

Figure 3.10 : Imaging quality comparision between the PCD algorithm and the BPA with multiple point targets in GCW-SAR: (a) image with PCD algorithm where $P = 10$; (b) image with PCD algorithm where $P = 20$; (c) image with PCD algorithm where $P = 50$; (d) ideal matched-filtering based image.

Fig. 3.10 (a), 3.10 (b) and 3.10 (c) are the images of point targets with PCD algorithm when $P = 10$, $P = 20$ and $P = 50$ respectively, and Fig. 3.10 (d) is the image of point targets with the ideal matched-filtering algorithm. It is clearly seen that the targets are correctly imaged based on the PCD algorithm when P is increased to 50. Compared with the image using the matched-filtering shown in Fig. 3.10 (d), the only degradation of the image quality with the PCD algorithm appears in the azimuth direction when P is small due to the linear approximation. In range direction, the targets can be distinguished clearly even when $P = 10$. Such degradation can be neglected if a suitable number of segments P is used.

3.6.5 Performance of Decimated PCD Algorithm

In the final simulation experiment, the multiple-target decimated PCD imaging with different Δx is investigated. P is set to 50. The transmitted signal bandwidth is set to 1 GHz and L_a is 0.9 m. The range and azimuth resolution are thus equal to 0.3 m and 0.45 m respectively. The final decimated PCD images with $\Delta x = 0.18$ m ($T_P/(T_s * N_s) = 30$) and $\Delta x = 0.027$ m ($T_P/(T_s * N_s) = 200$) are shown in Fig. 3.11 respectively. It is clearly seen that the error caused by the zero-th order approximation in decimated PCD algorithm is negligible with a proper Δx.

3.7 Summary

A novel SAR concept with full duplex operation and continuous wave signalling is proposed, followed by a fast imaging algorithm to reduce the computational complexity. In this GCW-SAR system, transmission and reception are conducted at the same time in the same frequency band by employing appropriate self-interference cancellation techniques and the continuously received signals can be extracted and stored as one-dimensional raw data. After correlating with location dependent reference signals, the one-dimensional raw data can be efficiently processed to reconstruct

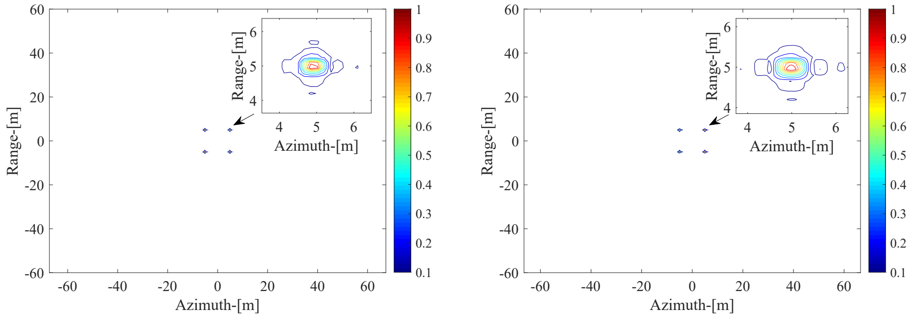

(a)

(b)

Figure 3.11 : Multi-targets SAR imaging comparison among different Δx: (a) $\Delta x = 0.18$ m ($T_P/(T_s * N_s) = 30$) and (b) $\Delta x = 0.027$ m ($T_P/(T_s * N_s) = 200$).

the image. The GCW-SAR performance is evaluated and simulated. As shown from the analytical and simulation results, the proposed new SAR concept and PCD algorithm offer many advantages over conventional pulsed and CW SARs. Firstly, the radar receives more reflected signal energy with CW signalling, hence retaining the same advantages as FMCW-SAR; Secondly, the sampling in azimuth will no longer be restricted, thus eliminating a number of inherent limitations in conventional systems; Thirdly, the system configuration and transmitted signal design are much more flexible. These advantages make the new SAR system a significant advance in SAR technology.

The work presented in this chapter establishes a solid theoretical foundation for next generation imaging radars. The proposed GCW-SAR can be combined with the multiple-input and multiple-output radar to further improve the system performance, such as 3-D imaging suitable for the non-flat terrain. Based on the PCD algorithm, more new active and passive SAR configurations can be further designed to suit different performance requirements.

Chapter 4

PCD Performance Analysis

The PCD algorithm, as a novel 1-D continuous wave imaging process, is the key technique for the GCW-SAR. In this chapter, a detailed theoretical analysis on the PCD algorithm's performance is presented. The common stripmap geometry as shown in Fig. 3.1 is considered, where the difference between the conventional SAR imaging and PCD imaging can be shown clearly and the PCD imaging analyses can be derived easily.

The conventional SAR and PCD imaging processes as the results of the zero-th order and the first order slant range approximations are firstly re-formulated respectively in Section 4.1. Based on the slant range of the approximation, the ambiguity functions in range and azimuth respectively for the PCD algorithm are then analytically derived in Section 4.2. Afterwards, Section 4.3 analyzes the PCD imaging performance in terms of a normalized imaging error as compared with the ideal matched filtering algorithm, which is shown to be a function of an imaging quality factor. This factor quantifies the PCD imaging performance and can be used to guide the GCW-SAR parameter design. Additionally, Section 4.4 analyzes the effect of the downsampling and the zero-th order approximation to the decimated PCD performance and its normalized error function is derived accordingly. Finally, the simulation results which can validate the PCD performance analysis are shown in Section 4.5.

4.1 Imaging Comparison between Conventional SAR Algorithms and PCD Algorithm

Generally speaking, the SAR image reconstruction can be theoretically formulated as a cross-correlation between the received signal and a location dependent reference signal based on the pulse compression principle, known as the ideal matched filtering algorithm. The imaging process of an arbitrary point (x_m, y_n) can be expressed as

$$I(x_m, y_n) = \int_{\frac{x_m}{v}-\frac{T_L}{2}}^{\frac{x_m}{v}+\frac{T_L}{2}} s_r(t)s^*(t - \frac{2r(t, x_m, y_n)}{c})e^{j\frac{4\pi}{\lambda}r(t,x_m,y_n)}dt \tag{4.1}$$

where the synthetic aperture time is defined as T_L, the asterisk $*$ indicates complex conjugation, and $s^*(t - 2r(t, x_m, y_n)/c)e^{j\frac{4\pi}{\lambda}r(t,x_m,y_n)}$ is the location dependent reference signal for the point (x_m, y_n).

In conventional SAR, the transmission and reception are repeated every PRI, and the slant range of point (x_m, y_n) in each PRI is assumed to be constant, thus forming the zero-th order approximation of $r(t, x_m, y_n)$ shown in Fig. 4.1 (a) and described as

$$\widetilde{r}_0(t, x_m, y_n) = r(\tau_q, x_m, y_n), t \in [\tau_q, \tau_q + PRI) \tag{4.2}$$

where $\tau_q = q \cdot PRI + x_m/v - T_L/2$, $q = 0, 1, ..., [T_L/PRI] - 1$, indicates the start of each PRI and $[T_L/PRI]$ is the number of PRIs over T_L. The conventional SAR imaging process can be expressed as

$$\begin{aligned} &I_0(x_m, y_n) \\ &= \int_{\frac{x_m}{v}-\frac{T_L}{2}}^{\frac{x_m}{v}+\frac{T_L}{2}} s_r(t)s^*(t - \frac{2\widetilde{r}_0(t, x_m, y_n)}{c})e^{j\frac{4\pi}{\lambda}\widetilde{r}_0(t,x_m,y_n)}dt \\ &= \sum_{q=0}^{[T_L/PRI]-1} e^{j\frac{4\pi}{\lambda}r(\tau_q,x_m,y_n)} \int_{q\cdot PRI+\frac{x_m}{v}-\frac{T}{2}}^{(q+1)\cdot PRI+\frac{x_m}{v}-\frac{T}{2}} s_r(t)s^*(t - \frac{2r(\tau_q, x_m, y_n)}{c})dt \end{aligned} \tag{4.3}$$

where t, the fast time, describes the time delay of the received signals during each PRI, whereas τ_q, the slow time, describes the discrete time instants whenever the

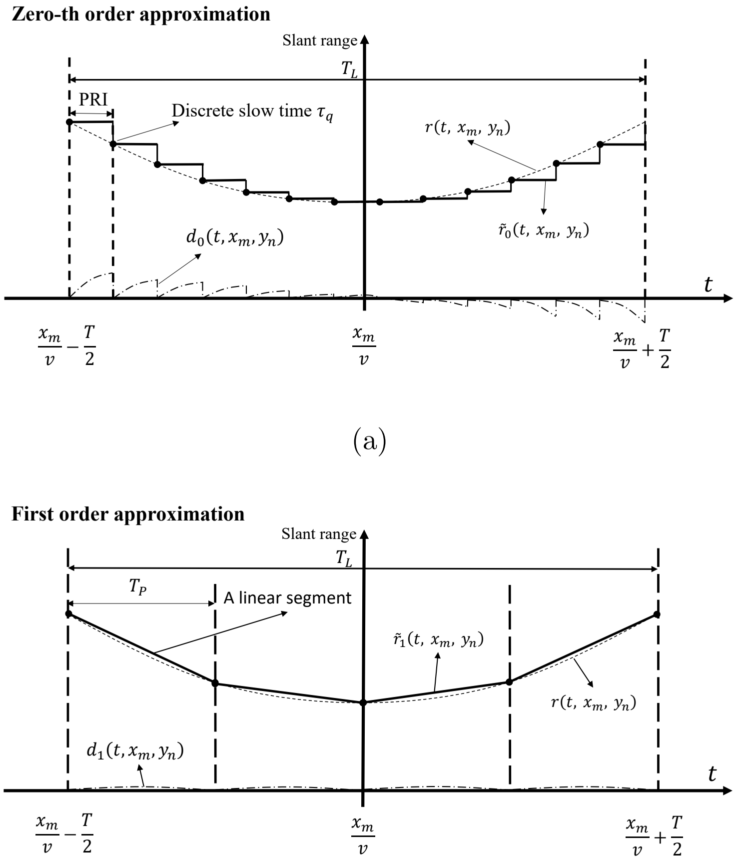

(a)

(b)

Figure 4.1 : Slant range approximations in conventional SAR imaging and PCD imaging: (a) conventional SAR imaging; (b) PCD imaging.

radar travels over a PRI. Therefore, the cross-correlation can be manipulated by independent range and azimuth compressions.

This conventional operation enables FFT-based imaging algorithms with low computational complexity, e.g., the range Doppler algorithm. The error caused by the zero-th order approximation is presented as the black dash-dot line in Fig. 4.1

(a) and can be described as

$$\begin{aligned} d_0(t, x_m, y_n) &= \widetilde{r}_0(t, x_m, y_n) - r(t, x_m, y_n) \approx \frac{(x_m - v\tau_q)^2 - (x_m - vt)^2}{2R(y_n)} \\ &= \frac{-v^2t^2 + 2x_m vt + v^2\tau_q^2 - 2x_m v\tau_q}{2R(y_n)}, t \in [\tau_q, \tau_q + PRI) \end{aligned} \tag{4.4}$$

which indicates that the error in each PRI is different from one another.

The zero-th order approximation leads to some intrinsic limitations in conventional SARs. Firstly, the contradiction between range swath and azimuth resolution is inevitable. To satisfy the azimuth sampling requirement with high Doppler frequency bandwidth, the PRI needs to be short, but a short PRI leads to a narrow range swath. Secondly, the continuous motion within a sweep in FMCW-SAR leads to a range walk term and additional range-azimuth coupling which have to be compensated before the image focusing [28]. In addition, the compensation of RCM is also necessary due to the slow time sampling, which complicates the imaging process [8].

With GCW-SAR, the transmission and reception are conducted at the same time, generating a one-dimensional raw data structure without PRI. Based on the PCD imaging principle, GCW-SAR adopts the first order approximation of the slant range which is composed of P linear segments linked end to end, as shown in Fig. 4.1 (b). Note that $r(t + x_m/v, x_m, y_n) = r(t, 0, y_n)$ is valid in the flat terrain case. Assuming that the length of each segment is $T_P = T_L/P$ and the p-th segment starts from $t_p = p \cdot T_P - T/2, p = 0, 1, 2, ...P - 1$, the corresponding linear approximated slant range can be expressed as

$$\begin{aligned}
&\widetilde{r}_1(t, x_m, y_n)\\
&= \frac{r(t_{p+1} + \frac{x_m}{v}, x_m, y_n) - r(t_p + \frac{x_m}{v}, x_m, y_n)}{(t_{p+1} - t_p)}(t - t_p - \frac{x_m}{v}) + r(t_p + \frac{x_m}{v}, x_m, y_n)\\
&= \frac{r(t_{p+1}, 0, y_n) - r(t_p, 0, y_n)}{(t_{p+1} - t_p)}(t - t_p - \frac{x_m}{v}) + r(t_p, 0, y_n)\\
&= -\frac{\lambda}{2} f_{D_p}(y_n)(t - t_p - \frac{x_m}{v}) + r(t_p, 0, y_n), t \in [t_p + \frac{x_m}{v}, t_{p+1} + \frac{x_m}{v})
\end{aligned} \tag{4.5}$$

where $f_{D_p}(y_n) = -2/\lambda \cdot (r(t_{p+1}, 0, y_n) - r(t_p, 0, y_n))/(t_{p+1} - t_p)$ is the constant Doppler frequency for the p-th segment. Thus, the PCD imaging process for the point (x_m, y_n) can be described as

$$\begin{aligned}
&I_1(x_m, y_n)\\
&= \int_{\frac{x_m}{v} - \frac{T}{2}}^{\frac{x_m}{v} + \frac{T}{2}} s_r(t)s^*(t - \frac{2\widetilde{r}_1(t, x_m, y_n)}{c})e^{j\frac{4\pi}{\lambda}\widetilde{r}_1(t, x_m, y_n)}dt\\
&= \sum_{p=0}^{P-1} \int_{p\cdot T_P + \frac{x_m}{v} - \frac{T}{2}}^{(p+1)\cdot T_P + \frac{x_m}{v} - \frac{T}{2}} s_r(t)s^*(t - \frac{2\widetilde{r}_1(t, x_m, y_n)}{c})e^{-j2\pi f_{D_p}(y_n)(t - t_p - \frac{x_m}{v}) + j\frac{4\pi}{\lambda}r(t_p, 0, y_n)}dt.
\end{aligned} \tag{4.6}$$

With the linear approximation, two adjacent image points $I_1(x_m, y_n)$ and $I_1(x_m + \Delta x, y_n)$ spaced by Δx are mainly different by a constant phase shift, $e^{j2\pi f_{D_p}(y_n)\Delta x/v}$ for the p-th segment in addition to a minor adjustment of the integration interval. Therefore, the images can be reconstructed recursively in azimuth without any involvement of the slow time and hence the inherent limitations in conventional SARs are removed.

The error caused by the first order approximation is shown in Fig. 4.1 (b) plotted by the black dash-dot line. From (3.6) and (4.5), it can be expressed as

$$
\begin{aligned}
&d_1(t, x_m, y_n) = \widetilde{r}_1(t, x_m, y_n) - r(t, x_m, y_n)\\
&= -\frac{\lambda}{2} f_{D_p}(y_n)(t - t_p - \frac{x_m}{v}) + r(t_p, 0, y_n) - r(t, x_m, y_n)\\
&\approx \frac{R(y_n) + \frac{v^2 t_{p+1}^2}{2R(y_n)} - R(y_n) - \frac{v^2 t_p^2}{2R(y_n)}}{t_{p+1} - t_p}(t - t_p - \frac{x_m}{v}) + R(y_n)\\
&+ \frac{v^2 t_p^2}{2R(y_n)} - R(y_n) - \frac{(x_m - vt)^2}{2R(y_n)}\\
&= -\frac{(x_m - vt)^2 + v(t_{p+1} + t_p)(x_m - vt) + v^2 t_p t_{p+1}}{2R(y_n)}, t \in [t_p + \frac{x_m}{v}, t_{p+1} + \frac{x_m}{v}).
\end{aligned}
\tag{4.7}
$$

It is also interesting to see that

$$
\begin{aligned}
&d_1(t + T_P, x_m, y_n)\\
&= -\frac{1}{2R(y_n)}((x_m - v(t + T_P))^2 + v(t_{p+1} + t_p + 2T_P)\\
&\cdot (x_m - v(t + T_P)) + v^2(t_p + T_P)(t_{p+1} + T_P))\\
&= -\frac{1}{2R(y_n)}((x_m - vt)^2 - 2(x_m - vt)vT_P + v^2 T_P^2 + v(t_{p+1} + t_p)(x_m - vt)\\
&- 2v^2 T_P^2 + 2(x_m - vt)vT_P - v^2 T_P(t_p + t_{p+1}) + v^2 t_p t_{p+1} + v^2 T_P(t_p + t_{p+1}) + v^2 T_P^2)\\
&= d_1(t, x_m, y_n), t \in [t_p + \frac{x_m}{v}, t_{p+1} + \frac{x_m}{v})
\end{aligned}
\tag{4.8}
$$

which demonstrates that $d_1(t, x_m, y_n)$ is a periodic function with a period T_P.

As seen from Fig. 4.1, the error is largely reduced with linear approximation, and thus the PCD algorithm can perform well even with a small number of segments P. Moreover, the aforementioned intrinsic limitations caused by the slow time sampling are eliminated in the PCD algorithm.

4.2 PCD Imaging Ambiguity Function

To evaluate the PCD imaging performance, the close form of the ambiguity function when using PCD algorithm is derived firstly. Assuming that the target is located at the origin $(0, 0)$, the received signal can be expressed as $s_r(t) = \sigma(0, 0)s(t-$

$2r(t,0,0)/c)e^{-j\frac{4\pi}{\lambda}r(t,0,0)}$ and the PCD image can be expressed as

$$\begin{aligned}I_1(x_m,y_n) = &\int_{\frac{x_m}{v}+\frac{T_L}{2}}^{\frac{x_m}{v}-\frac{T_L}{2}} \sigma(0,0)s(t-\frac{2r(t,0,0)}{c})s^*(t-\frac{2\widetilde{r}_1(t,x_m,y_n)}{c})\\ &e^{j\frac{4\pi}{\lambda}(\widetilde{r}_1(t,x_m,y_n)-r(t,0,0))}dt.\end{aligned} \tag{4.9}$$

For simplicity, the two cases $I_1(0,y_n)$ and $I_1(x_m,0)$ are considered respectively. The first one represents the image in range direction and the second one in azimuth direction.

4.2.1 Imaging in Range

When $x_m = 0$,

$$\begin{aligned}&\widetilde{r}_1(t,0,y_n) - r(t,0,0) = -\frac{\lambda}{2}f_{D_p}(y_n)(t-t_p) + r(t_p,0,y_n) - r(t,0,0)\\ &\approx \frac{v^2(t_{p+1}+t_p)}{2R(y_n)}(t-t_p) + R(y_n) + \frac{v^2t_p^2}{2R(y_n)} - R_c - \frac{v^2t^2}{2R_c} \approx R(y_n) - R_c\end{aligned} \tag{4.10}$$

since the slant range $R(y_n)$ is much larger than the length of segment T_Pv. Assuming that $s(t)$ satisfies the requirement of the transmitted waveform in GCW-SAR, i.e., it is any normalized low-pass baseband signal with constant energy spectrum in its bandwidth B, Eq. (4.9) can then be simplified as

$$\begin{aligned}I_1(0,y_n) &\approx e^{j\frac{4\pi}{\lambda}(R(y_n)-R_c)}\int_{-\frac{T_L}{2}}^{\frac{T_L}{2}} \sigma(0,0)s(t-\frac{2r(t,0,0)}{c})s^*(t-\frac{2\widetilde{r}_1(t,0,y_n)}{c})dt\\ &\approx e^{j\frac{4\pi}{\lambda}(R(y_n)-R_c)}\int_{-\frac{T_L}{2}}^{\frac{T_L}{2}} \sigma(0,0)s(t-\frac{2R_c-2R(y_n)}{c})s^*(t)dt\\ &\approx \sigma(0,0)e^{j\frac{4\pi}{\lambda}(R(y_n)-R_c)}sinc(\frac{2B}{c}(R(y_n)-R_c))\end{aligned} \tag{4.11}$$

where $sinc(t)$ is the sinc function defined by $sin(\pi t)/\pi t$. Consequently, PCD algorithm has a negligible loss on SAR imaging performance in range direction.

4.2.2 Imaging in Azimuth

When $y_n = 0$, Eq. (4.9) becomes

$$
\begin{aligned}
&I_1(x_m, 0)\\
&= \int_{\frac{x_m}{v}-\frac{T_L}{2}}^{\frac{x_m}{v}+\frac{T_L}{2}} \sigma(0,0)s(t-\frac{2r(t,0,0)}{c})s^*(t-\frac{2\widetilde{r}_1(t,x_m,0)}{c})e^{j\frac{4\pi}{\lambda}(\widetilde{r}_1(t,x_m,0)-r(t,0,0))}dt\\
&= \int_{-\frac{T_L}{2}}^{\frac{T_L}{2}} \sigma(0,0)s(t+\frac{x_m}{v}-\frac{2r(t+\frac{x_m}{v},0,0)}{c})s^*(t+\frac{x_m}{v}-\frac{2\widetilde{r}_1(t+\frac{x_m}{v},\frac{x_m}{v},0)}{c})\\
&\cdot e^{j\frac{4\pi}{\lambda}(\widetilde{r}_1(t+\frac{x_m}{v},x_m,0)-r(t+\frac{x_m}{v},0,0))}.
\end{aligned}
\tag{4.12}
$$

Substituting $r(t+\frac{x_m}{v},\frac{x_m}{v},0) = r(t,0,0)$, $\widetilde{r}_1(t+\frac{x_m}{v},\frac{x_m}{v},0) = \widetilde{r}_1(t,0,0)$, $d_1(t,0,0) = \widetilde{r}_1(t,0,0) - r(t,0,0)$ and (3.6) into (4.12), $I_1(x_m, 0)$ can be simplified as

$$
\begin{aligned}
I_1(x_m,0) = &\int_{-\frac{T_L}{2}}^{\frac{T_L}{2}} \sigma(0,0)s(t+\frac{x_m}{v}-\frac{2r(t+\frac{x_m}{v},0,0)}{c})s^*(t+\frac{x_m}{v}-\frac{2\widetilde{r}_1(t,0,0)}{c})\\
&\cdot e^{j\frac{4\pi}{\lambda}(\widetilde{r}_1(t,0,0)-r(t,0,0))}e^{j\frac{4\pi}{\lambda}(r(t,0,0)-r(t+\frac{x_m}{v},0,0))}dt\\
&= \sigma(0,0)e^{-j\frac{2\pi x_m^2}{\lambda R_c}} \int_{-\frac{T_L}{2}}^{\frac{T_L}{2}} s(t+\frac{x_m}{v}-\frac{2r(t+\frac{x_m}{v},0,0)}{c})s^*(t+\frac{x_m}{v}-\frac{2\widetilde{r}_1(t,0,0)}{c})\\
&\cdot e^{j\frac{4\pi}{\lambda}d_1(t,0,0)}e^{-j2\pi\frac{2vx_m}{\lambda R_c}t}dt.
\end{aligned}
\tag{4.13}
$$

Further assuming that $s(t)$ is a phase only signal, i.e., $s(t) = 1/\sqrt{T}\cdot e^{j\phi(t)}$, where $\phi(t)$ is any phase function, and approximating $s(t - 2r(t + x_m/v, 0, 0)/c)$ as $s(t - 2\widetilde{r}(t,0,0)/c)$ when the condition $|x_m - vt| << R(y)$ is satisfied, the image $I_1(x_m, 0)$ can be further simplified as

$$
\begin{aligned}
I_1(x_m,0) =&\sigma(0,0)e^{-j\frac{2\pi x_m^2}{\lambda R_c}}\frac{1}{T_L}\int_{-\frac{T_L}{2}}^{\frac{T_L}{2}} e^{j\frac{4\pi}{\lambda}d_1(t,0,0)}e^{-j2\pi\frac{2vx_m}{\lambda R_c}t}dt\\
&= \sigma(0,0)e^{-j\frac{2\pi x_m^2}{LL_a}}\sum_{i=-\infty}^{\infty} W(iP\frac{L_a}{2})sinc(\frac{2}{L_a}(x_m - iP\frac{L_a}{2}))
\end{aligned}
\tag{4.14}
$$

where $L = vT_L \approx \lambda/L_a \cdot R_c$ is defined as the synthetic aperture and L_a the antenna aperture in azimuth. The detailed derivation of (4.14) is provided in Appendix A.

Clearly, $I_1(x_m, 0)$ is a weighted sum of sinc functions with equal spacing $PL_a/2$ in azimuth. The weight function $W(x)$ is defined as (see Appendix B)

$$\begin{aligned}
W(x) &= \frac{1}{T_P}\int_{-\frac{T_P}{2}}^{\frac{T_P}{2}} e^{j\frac{4\pi}{\lambda}d_1(t,0,0)} e^{-j2\pi\frac{2vx}{\lambda R_c}t} dt \\
&= \sqrt{\frac{L_aP^2}{2\pi L}} e^{j\frac{\pi L}{2L_aP^2}} e^{j\frac{2\pi x^2}{LL_a}} \Big(C(\sqrt{\frac{2\pi x^2}{LL_a}} + \sqrt{\frac{\pi L}{2L_aP^2}}) - C(\sqrt{\frac{2\pi x^2}{LL_a}} - \sqrt{\frac{\pi L}{2L_aP^2}}) \\
&+ jS(\sqrt{\frac{2\pi x^2}{LL_a}} - \sqrt{\frac{\pi L}{2L_aP^2}}) - jS(\sqrt{\frac{2\pi x^2}{LL_a}} + \sqrt{\frac{\pi L}{2L_aP^2}})\Big)
\end{aligned} \tag{4.15}$$

where $S(x)$ and $C(x)$ are the Fresnel integrals also defined in Appendix B [74].

The first derivative of $|W(x)|$ can be found as shown in

$$\begin{aligned}
\frac{d|W(x)|}{dx} &= \sqrt{\frac{L_aP^2}{2\pi L}} \cdot W_{cs}^{'}(x) \\
&\cdot \Bigg(2\Big(C(\sqrt{\frac{2\pi x^2}{LL_a}} + \sqrt{\frac{\pi L}{2L_aP^2}}) - C(\sqrt{\frac{2\pi x^2}{LL_a}} - \sqrt{\frac{\pi L}{2L_aP^2}})\Big) \\
&\Big(cos(\frac{2\pi}{LL_a}(x + \frac{L}{2P})^2) - cos(\frac{2\pi}{LL_a}(x - \frac{L}{2P})^2)\Big) \\
&+ 2\Big(S(\sqrt{\frac{2\pi x^2}{LL_a}} - \sqrt{\frac{\pi L}{2L_aP^2}}) - S(\sqrt{\frac{2\pi x^2}{LL_a}} + \sqrt{\frac{\pi L}{2L_aP^2}})\Big) \\
&\Big(sin(\frac{2\pi}{LL_a}(x - \frac{L}{2P})^2) - sin(\frac{2\pi}{LL_a}(x + \frac{L}{2P})^2)\Big)\Bigg)
\end{aligned} \tag{4.16}$$

where $W_{cs}^{'}(x)$ is a function of x. Note that $d|W(x)|/d = 0$ when $2\pi/(LL_a) \cdot (x - L/(2P))^2 - 2\pi/(LL_a) \cdot (x + L/(2P))^2 = i \cdot 2\pi$, for $i = 0, \pm 1, \pm 2, ...$, thus $x = i \cdot PL_a/2$ are the extremums of $|W(x)|$. Interestingly, the sinc function $sinc(2/L_a \cdot (x_m - iPL_a/2))$ are also located at these extremum points and it will be shown later in the simulation results that they are actually the minimum points of $|W(x)|$ except for $i = 0$.

4.3 PCD Normalized Error function

The normalized PCD imaging error as compared with the ideal matched filtering method can be evaluated as

$$\epsilon^2 = \frac{\int_{-\infty}^{\infty} |I_1(x_m,0) - I(x_m,0)|^2 dx_m}{\int_{-\infty}^{\infty} |I(x_m,0)|^2 dx_m} \tag{4.17}$$

where $I(x_m, 0)$ is the ideal image expressed as

$$\begin{aligned} I(x_m,0) &= \sigma(0,0)\int_{\frac{x_m}{v}-\frac{T}{2}}^{\frac{x_m}{v}+\frac{T}{2}} s(t-\frac{2r(t,0,0)}{c})s^*(t-\frac{2r(t,x_m,0)}{c})e^{j\frac{4\pi}{\lambda}(r(t,x_m,0)-r(t,0,0))}dt \\ &= \sigma(0,0)\int_{-\frac{T}{2}}^{\frac{T}{2}} s(t+\frac{x_m}{v}-\frac{2r(t+\frac{x_m}{v},0,0)}{c})s^*(t+\frac{x_m}{v}-\frac{2r(t,0,0)}{c}) \\ &\cdot e^{j\frac{4\pi}{\lambda}(r(t,0,0)-r(t+\frac{x_m}{v},0,0))}dt \\ &\approx \sigma(0,0)e^{-j\frac{2\pi x_m^2}{\lambda R_c}}\frac{1}{T}\int_{-\infty}^{\infty} rect(\frac{t}{T})e^{-j2\pi\frac{2vx_m}{\lambda R_c}t}dt \end{aligned} \tag{4.18}$$

with the same assumptions and methods used in the derivation of (4.14). Denoting $2vx_m/(\lambda R_c)$ and substituting (4.18) into (4.17), ϵ^2 can be further derived as

$$\epsilon^2 = \frac{\int_{-\infty}^{\infty} |\int_{-\infty}^{\infty} rect(\frac{t}{T})(e^{j\frac{4\pi}{\lambda}d_1(t,0,0)}-1)e^{-j2\pi\Omega t}dt|^2 d\Omega}{\int_{-\infty}^{\infty} |\int_{-\infty}^{\infty} rect(\frac{t}{T})e^{-j2\pi\Omega t}dt|^2 d\Omega}. \tag{4.19}$$

According to Parseval's Theorem, the power in frequency domain is equal to that in time domain. Therefore, Eq. (4.19) can be further simplified as

$$\begin{aligned} \epsilon^2 &= \frac{\int_{-\infty}^{\infty} |rect(\frac{t}{T})(e^{j\frac{4\pi}{\lambda}d_1(t,0,0)}-1)|^2 dt}{\int_{-\infty}^{\infty} |rect(\frac{t}{T})|^2 dt} = \frac{\int_{-\frac{T_P}{2}}^{\frac{T_P}{2}} |e^{j\frac{4\pi}{\lambda}d_1(t,0,0)}-1|^2 dt}{\int_{-\frac{T_P}{2}}^{\frac{T_P}{2}} |1|^2 dt} \\ &= \frac{1}{T_P}\int_{-\frac{T_P}{2}}^{\frac{T_P}{2}} (e^{j\frac{4\pi}{\lambda}d_1(t,0,0)}-1)(e^{-j\frac{4\pi}{\lambda}d_1(t,0,0)}-1)dt \\ &= 2 - \frac{1}{T_P}\int_{-\frac{T_P}{2}}^{\frac{T_P}{2}} e^{j\frac{4\pi}{\lambda}d_1(t,0,0)}dt - \frac{1}{T_P}\int_{-\frac{T_P}{2}}^{\frac{T_P}{2}} e^{-j\frac{4\pi}{\lambda}d_1(t,0,0)}dt \\ &= 2 - W(0) - W^*(0) = 2 - 2Re\{W(0)\} \end{aligned} \tag{4.20}$$

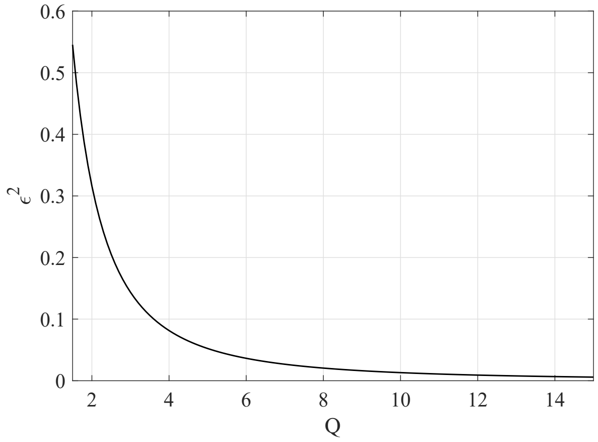

Figure 4.2 : Normalized PCD imaging error as a function of Q.

where $Re\{W(0)\}$ is the real part of $W(0)$. Since the Fresnel integrals $C(.)$ and $S(.)$ are odd functions, $W(0)$ can be derived from (4.15) as

$$\begin{aligned} W(0) = & \sqrt{\frac{L_aP^2}{2\pi L}} e^{j\frac{\pi L}{2L_aP^2}} \Big(C(\sqrt{\frac{\pi L}{2L_aP^2}}) - C(-\sqrt{\frac{\pi L}{2L_aP^2}}) \\ & + jS(-\sqrt{\frac{\pi L}{2L_aP^2}}) - jS(\sqrt{\frac{\pi L}{2L_aP^2}}) \Big) \\ = & \sqrt{\frac{2Q}{\pi}} e^{j\frac{\pi}{2Q}} \Big(C(\sqrt{\frac{\pi}{2Q}}) - jS(\sqrt{\frac{\pi}{2Q}}) \Big) \end{aligned} \tag{4.21}$$

where $Q = L_aP^2/L$ is defined as the image quality factor. From (4.20) and (4.21), it is seen that the normalized PCD imaging error is a function of Q. The error function curve shown in Fig. 4.2 indicates that the PCD imaging performs better as Q increases.

Therefore, for a given quality factor, the GCW-SAR parameters L_a, L, and P can be selected appropriately to satisfy the required PCD imaging performance.

4.4 Decimated PCD Algorithm Analysis

In this section, the effect of the downsampling and the zero-th order approximation on the performance of the decimated PCD algorithm is discussed. The effect of the downsampling is firstly presented. Then, the error of the slant range approximation in decimated PCD algorithm is analyzed and its normalized error function is derived to evaluate the performance.

4.4.1 Downsampling Effect

There is a trade-off between SNR and complexity in the decimated PCD imaging since the downsampling reduces the SNR due to less samples of received signals being used. As seen in (3.22) and Fig. 3.5, the azimuth image spacing is extended from $T_s v$ to $N_s T_s v = N_{s1} N_{s2} T_s v$ after two downsampling operations, and it can be seen that the number of the received samples is only reduced by the first downsampling factor N_{s1}. Therefore, a proper N_{s1} should be first selected to determine the SNR and the azimuth image spacing can be then adjusted by N_{s2}. This effect will be presented in the simulation results.

4.4.2 Normalized Error Function

Assuming that the time interval over the k-th constant segment of the p-th linear segment as shown in Fig. 3.4 (a) is described as $[t_p + x_m/v + k\Delta x/v, t_p + x_m/v + (k+1)\Delta x/v)$ where $k = 0, 1, ..., K-1$, the approximated slant range $\hat{r}_1(t, x_m, y_n)$ can be expressed as

$$\begin{aligned}\hat{r}_1(t, x_m, y_n) =& \widetilde{r}_1(t_p + \frac{x_m}{v} + k\frac{\Delta x}{v}, x_m, y_n)\\ &, t \in [t_p + \frac{x_m}{v} + k\frac{\Delta x}{v}, t_p + \frac{x_m}{v} + (k+1)\frac{\Delta x}{v}).\end{aligned} \tag{4.22}$$

The error in slant range caused by decimated PCD can be then expressed as

$$\begin{aligned}&\hat{d}_1(t, x_m, y_n) = \hat{r}_1(t, x_m, y_n) - r(t, x_m, y_n)\\ &= \frac{r(t_{p+1}, 0, y_n) - r(t_p, 0, y_n)}{(t_{p+1} - t_p)}(t_p + \frac{x_m}{v} + k\frac{\Delta x}{v} - t_p - \frac{x_m}{v}) + r(t_p, 0, y_n) - r(t, x_m, y_n)\\ &\approx \frac{v^2(t_{p+1} + t_p)}{2R(y_n)}k\frac{\Delta x}{v} + \frac{v^2}{2R(y_n)}(t_p^2 - (t - \frac{x_m}{v})^2)\\ &, t \in [t_p + \frac{x_m}{v} + k\frac{\Delta x}{v}, t_p + \frac{x_m}{v} + (k+1)\frac{\Delta x}{v}).\end{aligned} \tag{4.23}$$

Similar to (4.17), the normalized error of decimated PCD imaging compared with the ideal matched filtering method can be evaluated as

$$\epsilon^2 = \frac{\int_{-\infty}^{\infty} |\hat{I}_1(x_m,0) - I(x_m,0)|^2 dx_m}{\int_{-\infty}^{\infty} |I(x_m,0)|^2 dx_m} \tag{4.24}$$

where $I(x_m, 0)$ is expressed as (4.18). With the same technique used to derive (4.20), Eq. 4.24 can be further expressed as

$$\begin{aligned}
\epsilon^2 &= \frac{\int_{-\infty}^{\infty} |rect(\frac{t}{T})(e^{j\frac{4\pi}{\lambda}\hat{d}_1(t,0,0)} - 1)|^2 dt}{\int_{-\infty}^{\infty} |rect(\frac{t}{T})|^2 dt} = \frac{\int_{-\frac{T}{2}}^{\frac{T}{2}} |e^{j\frac{4\pi}{\lambda}\hat{d}_1(t,0,0)} - 1|^2 dt}{\int_{-\frac{T}{2}}^{\frac{T}{2}} |1|^2 dt} \\
&= \frac{1}{T}\int_{-\frac{T}{2}}^{\frac{T}{2}} (e^{j\frac{4\pi}{\lambda}\hat{d}_1(t,0,0)} - 1)(e^{-j\frac{4\pi}{\lambda}\hat{d}_1(t,0,0)} - 1) dt = 2 - \frac{1}{T}\int_{-\frac{T}{2}}^{\frac{T}{2}} e^{j\frac{4\pi}{\lambda}\hat{d}_1(t,0,0)} dt \\
&- \frac{1}{T}\int_{-\frac{T_P}{2}}^{\frac{T}{2}} e^{-j\frac{4\pi}{\lambda}\hat{d}_1(t,0,0)} dt = 2 - 2Re\{\frac{1}{T}\int_{-\frac{T}{2}}^{\frac{T}{2}} e^{j\frac{4\pi}{\lambda}\hat{d}_1(t,0,0)} dt\} \\
&= 2 - 2Re\{\frac{1}{P}\sum_{p=0}^{P-1}\sum_{k=0}^{K-1} e^{j\frac{2\pi}{P^2}\frac{L}{L_a}((-P+2p+1)\frac{k}{K}+(-\frac{P}{2}+p)^2)}\sqrt{\frac{P^2}{2\pi}\frac{L_a}{L}} \\
&\cdot \Big(C((-\frac{P}{2}+p+\frac{k+1}{K})\sqrt{\frac{2\pi}{P^2}\frac{L}{L_a}}) - C((-\frac{P}{2}+p+\frac{k}{K})\sqrt{\frac{2\pi}{P^2}\frac{L}{L_a}}) \\
&+ jS((-\frac{P}{2}+p+\frac{k}{K})\sqrt{\frac{2\pi}{P^2}\frac{L}{L_a}}) - jS((-\frac{P}{2}+p+\frac{k+1}{K})\sqrt{\frac{2\pi}{P^2}\frac{L}{L_a}})\Big)\}
\end{aligned} \tag{4.25}$$

where the closed-form expression of the integral $1/T_L \int_{-T_L/2}^{T_L/2} e^{j4\pi/\lambda \cdot \hat{d}_1(t,0,0)} dt$ is derived in Appendix C. It is seen that the decimated PCD error is a function of P, K and L/L_a.

Since the $\hat{d}_1 \approx d_1$ when K is sufficiently large, the decimated PCD imaging error is bounded by the PCD imaging error. Therefore, in a practical GCW-SAR system, the GCW-SAR parameters L, L_a and P should firstly be determined to satisfy the upper bound of the GCW-SAR imaging performance. With the knowledge of P and L/L_a, K can then be selected based on (4.25) to meet the required imaging performance.

4.5 Simulation Result

To compare the performance of different imaging algorithms, the same airborne simulation scenario is assumed. The transmitted signal is a continuous-wave periodic chirp signal. The SARs operate in the same stripmap mode with the following airborne SAR parameters: carrier frequency $f_c = 10$ GHz, platform altitude $h_0 = 7000$ m, antenna aperture $L_a = 0.9$ m, speed of radar platform $v = 70$ m/s, and $R_c = 8082.9$ m. To present the imaging performance in azimuth clearly, the y coordinate is normalized by the azimuth resolutions $\delta_x = L_a/2$ in the first four simulation experiments.

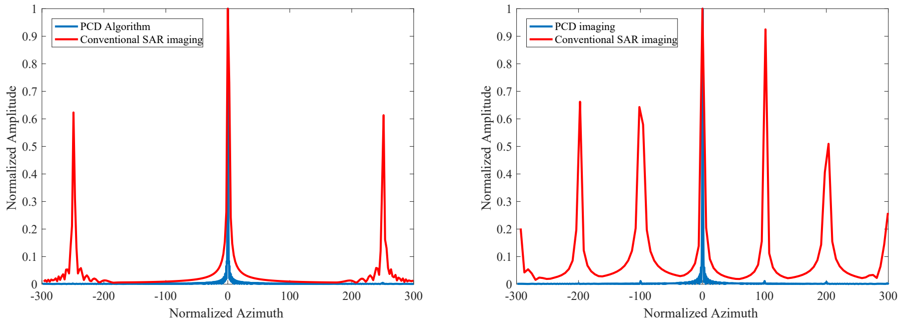

(a) (b)

Figure 4.3 : Comparison between PCD imaging and conventional SAR imaging when $P = [T_L/PRI] < 300$: (a) $P = [T_L/PRI] = 250$; (b) $P = [T_L/PRI] = 100$.

4.5.1 Comparison between Conventional SAR Imaging and PCD Imaging

In the first simulation experiment, the performance of an FMCW-SAR using PCD algorithm and range Doppler algorithm respectively is compared assuming that the number of linear segments, P, is the same as the number of PRIs, $[T_L/PRI]$, over a synthetic aperture time. Due to the zero-th order approximation of the slant range for the conventional range Doppler algorithm, azimuth ambiguity will occur if the PRI is large. However, the azimuth ambiguity using the PCD algorithm can be greatly reduced due to the first order approximation even if the linear segment is long. With the radar parameters given at the beginning of this section, the length of the synthetic aperture is almost $600\delta_x$, and the lowest bound of the unambiguous PRF, i.e., 1/PRI, is $78Hz$. Fig. 4.3 shows the imaging performance of a one-point image at $(0, 0)$ with $[T_L/PRI] = P = 250$ and $[T_L/PRI] = P = 100$ respectively. Obviously, the first order approximation in PCD imaging can reduce the azimuth ambiguity caused by the inadequate PRF in conventional SAR. In Fig. 4.3 (a), the first azimuth ambiguity will appear at the points $x = 250\delta_x$ and $x = -250\delta_x$ symmetrically when $[T_L/PRI] = P = 250$. Such ambiguities can be reduced to a negligible level in PCD imaging.

4.5.2 Performance of PCD Imaging

The PCD imaging ambiguity function theoretically derived in Section 4.2 is validated in the second simulation experiment. For simplicity, a one-point image at $(0, 0)$ is assumed. Firstly, the range images with $P = 60$, 40 and 20 respectively are shown in Fig. 4.4 (a). It is seen that the change in P makes no difference to the range image quality since the slant range is much longer than the length of a linear segment. The azimuth images with $P = 60$, 40 and 20 are shown in Fig. 4.4 (b), (c) and (d) respectively, where the corresponding values of the image quality factor Q are 12, 5.33 and 1.33, respectively, with $L_a = 0.9$ m and $L \approx 270$ m. It is clearly seen that an azimuth image is a sum of a set of sinc functions spaced by $PL_a/2$. The corresponding weight function $|W(x)|$ are plotted with the red lines in the figures, noting that the $i \cdot PL_a/2, i = \pm 1, \pm 2, \ldots$, are the locations of the local minimums of $|W(x)|$. The imaging performance shows that the ambiguity caused by PCD becomes increasingly negligible when $Q > 5.33$ and the corresponding $\epsilon^2 < 0.05$.

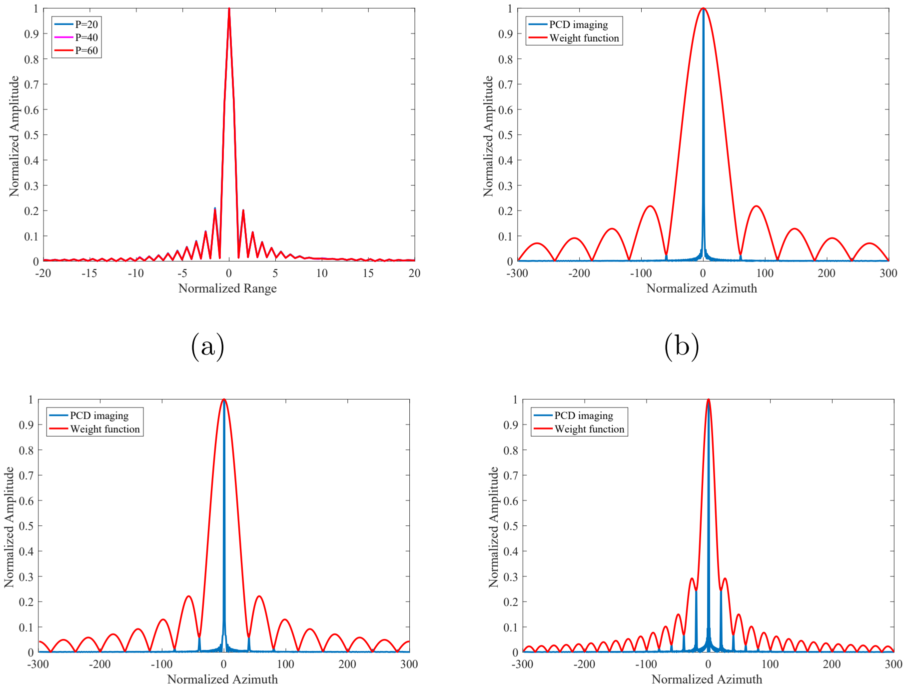

(a) (b)

(c) (d)

Figure 4.4 : PCD images in range and azimuth respectively, where the range images with $P = 60$, 40 and 20 are shown in (a), and the azimuth images and corresponding weight function $|W(x)|$ with different P are shown in (b) $P = 60$ ($Q = 12$), (c) $P = 40$ ($Q = 5.33$), and (d) $P = 20$ ($Q = 1.33$) respectively.

4.5.3 Performance of Decimated PCD Imaging

In this simulation experiment, the impact of azimuth image spacing Δx on the decimated PCD performance is investigated. Based on the aforementioned SAR parameters, the ratio L/L_a is 300. The number of linear segment P is set to 50 and the corresponding $Q = 8.33$. A one-point image at $(0, 0)$ is adopted and the azimuth imaging results with $\Delta x = 1$ m, 0.25 m, 0.125 m and 0.025 m (corresponding $K = 5, 20, 40,$ and 200) are shown respectively in Fig. 4.5. It is evident that the azimuth ambiguity can be reduced with the decreasing Δx. Compared with the PCD error at $Q = 8.33$, the decimated PCD error as a function of K is shown in

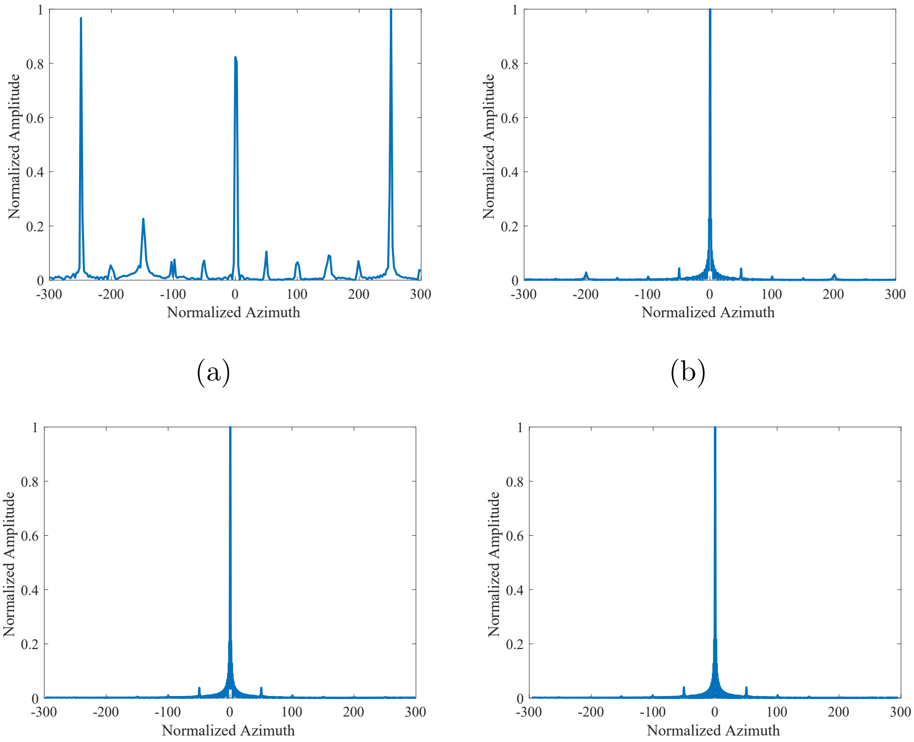

(a) (b)

(c) (d)

Figure 4.5 : Imaging performance of decimated PCD algorithm with different azimuth spacings: (a) $\Delta x = 1$ m ($K = 5$); (b) $\Delta x = 0.25$ m ($K = 20$); (c) $\Delta x = 0.125$ m ($K = 40$); and (d) $\Delta x = 0.025$ m ($K = 200$).

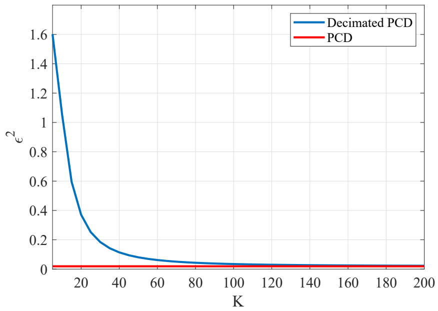

Figure 4.6 : Decimated PCD error as a function of K, when $P = 50$, $L/L_a = 300$ and $Q = 8.33$.

Fig. 4.6. We see that the PCD imaging error $\epsilon^2 = 0.02$ is the lower bound of the

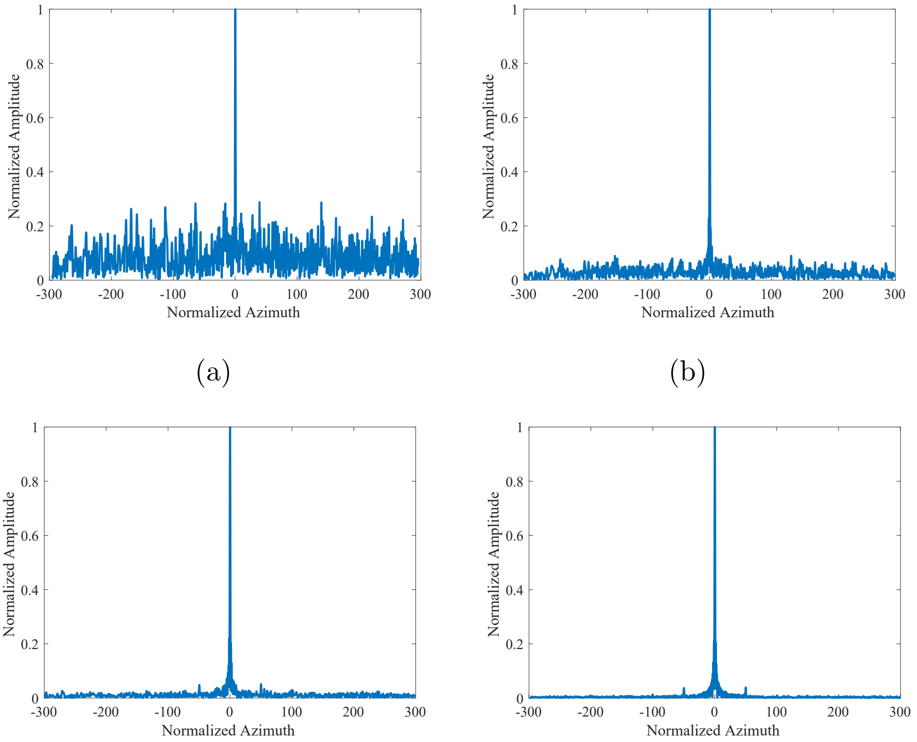

(a) (b)

(c) (d)

Figure 4.7 : Decimated PCD images in azimuth with different N_{s_1}: (a) $N_{s_1} = 10000$, (b) $N_{s_1} = 1000$, (c) $N_{s_1} = 100$ and (d) $N_{s_1} = 10$.

decimated PCD imaging. When K is larger than 140 ($\Delta x < 0.036$ m), the error caused by the zero-th order approximation can be neglected. In fact, K does not necessarily need to be reduced to 140 as Fig. 4.5 shows that almost the same imaging performance can be obtained when $K > 40$ since ϵ^2 is small enough. Therefore, a high-quality image with a large Δx can be achieved by decimated PCD imaging as long as ϵ^2 is sufficiently small.

4.5.4 Complexity and Impact of Downsampling on SNR

In the fourth simulation experiment, the computational cost between PCD and decimated PCD algorithms is compared and the impact of downsampling on SNR in decimated PCD algorithm is investigated. With $P = 50$, $L/L_a = 300$, $T_s = 5 \times 10^{-9}$

s and $\Delta x = 0.125$ m ($K = 40$), a one-point image at $(0, 0)$ is reconstructed by PCD and decimated PCD algorithms respectively. The number of complex multiplications in PCD imaging can be computed as 1.17×10^{11}. In decimated PCD imaging, with $N_{s_1} = 10000, 1000, 100$, and 10 respectively, the number of complex multiplications can be reduced to 4.13×10^6, 3.95×10^7, 3.93×10^8 and 3.93×10^9 respectively. Hence, the computational cost is significantly reduced in the decimated PCD imaging. Although a larger N_{s_1} can achieve a lower computational complexity, it also leads to a lower SNR after image reconstruction. Assuming that the SNR in the receiver is -30 dB, the final SAR images with $N_{s_1} = 10000, 1000, 100$, and 10 are shown in Fig. 4.7 respectively, validating the trade-off between complexity and SNR. Therefore, N_{s_1} and N_{s_2} should be determined appropriately to achieve a balance between SNR and complexity.

4.6 Summary

Detailed analysis of the PCD algorithm are presented in this chapter. Compared with the zero-th order approximation to the slant range in conventional SAR imaging, the PCD imaging demonstrates many advantages due to the one-dimensional data structure and the first order approximation to the slant range. The closed form ambiguity functions in range and azimuth direction are derived respectively. With ideal matched filtering method as the benchmark, the normalized imaging error function of the PCD algorithm is also formulated, which can be defined as a function of the image quality factor. The corresponding decimated PCD imaging error, lower-bounded by the PCD imaging error function, is also analyzed. The work presented in this chapter and supported by the experimental results validates the theoretical foundation of the PCD algorithm in terms of imaging process, ambiguity function, and performance bound, offering a clear guideline to the GCW-SAR imaging system design.

Chapter 5

GCW-SAR System Design

In this chapter, two GCW-SAR systems are developed for the different GCW-SAR applications. Firstly, a non-cooperative space-surface bistatic GCW-SAR system is proposed in Section 5.1 by exploiting the continuous wave signal from the transmitters of opportunity (e.g., GSM, analog TV, Digital Video Broadcasting-Terrestrial (DVB-T), DVB-S, DVB-S2, etc.) [75, 76, 77]. Unlike the conventional passive SAR, the image reconstruction is achieved based on the GCW-SAR concept, thus removing the intrinsic limitations caused by the slow time sampling. Secondly, a novel active GCW-SAR based on deramp-on-receive operating in millimeter wave frequency is proposed in Section 5.2. With deramp-on-receive, the receiver sampling rate is drastically reduced and the down-sampled one-dimensional raw data can be obtained from the received beat signal. The short wavelength of the millimeter wave carrier used in this system enables high azimuth resolution as well as short synthetic aperture which in turn significantly reduces the imaging computational complexity.

5.1 Passive GCW-SAR System Design

As an alternative to active SAR, passive SAR imaging system has gained more and more attention due to its covert operation without intentional transmission. By using transmitters of opportunity as the source of scene illumination, it can receive reflected and/or scattered signals off the Earth's surface and/or other objects for various remote sensing and imaging applications. A typical passive SAR configuration is the bistatic one with stationary transmitter but moving receivers. For example, the DVB-S signal from a geosynchronous satellite can be used as the illuminator of opportunity and the radar receivers can be mounted on a moving platform such as an unmanned aerial vehicle (UAV). This system is known as the space-surface bistatic SAR (SS-BSAR) [78].

Current passive SAR image processing algorithms are mostly based on respective range and azimuth compressions, where the continuous wave received echo signals over a synthetic aperture can be equally divided into multiple segments in time domain forming a 2-D data structure. However, these algorithms, e.g., passive RDA are still based on the “stop-and-go” approximation and the slow time sampling leads to the intrinsic limitation in conventional SAR. In addition, due to the continuously transmitted signal, RDA also introduces the range/azimuth coupling and range walk term like conventional FMCW SAR, thus further deteriorating the image quality. Moreover, for some passive SAR with cooperative transmitter, exact a *priori* information about the transmitter's parameters has to be estimated from the received reference signal.

The PCD imaging process is more suitable for the passive SAR scenario rather than the conventional SAR algorithms due to the 1-D time correlation over a synthetic aperture time. In this section, a non-cooperative SS-BSAR with PCD image processing is proposed. The system geometry of the SS-BSAR system is revisited and a modified PCD algorithm is proposed accordingly based on time-domain correlation between surveillance signal and reference signal, which can be recursively calculated with low complexity. Due to the non-cooperative nature, no transmitted signal parameter is necessary other than the angle-of-arrival (AoA) of the incident beam, further reducing the signal processing complexity for signal parameter estimation and synchronization.

5.1.1 System Configuration

The considered passive SAR system is equipped with two receiving antennas to separate direct reference signal and surveillance echoes from the observed scene: the reference antenna looks toward the transmitter and the surveillance one looks toward the observed scene. The remaining direct power, which masks the weak surveillance signal, can be further removed using CLEAN techniques [79]. In this section, the DVB-S is assumed as the source of scene illumination. Since the observed scene is much farther from the satellite than the radar, the normalized incident angle of the DVB-S signal can be assumed as a constant, $\vec{I} = (a, b, c)$, where $a^2 + b^2 + c^2 = 1$, when the radar is traveling over the synthetic aperture.

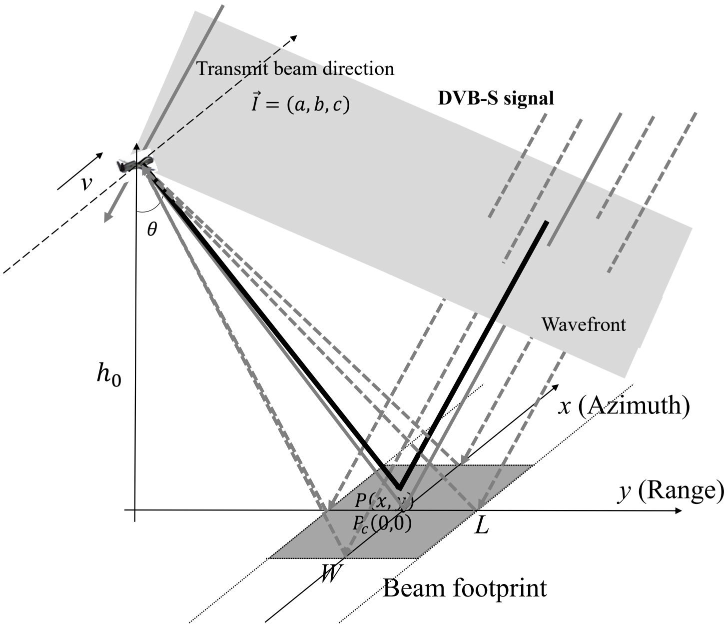

Figure 5.1 : SS-BSAR geometry.

The system geometry is presented in Fig. 5.1. For simplicity, a flat-terrain stripmap mode is considered. The origin is set as the center of the observed scene (beam footprint), $P_c(0, 0)$. The range and azimuth widths of the beam footprint are set to W and L respectively. The radar is mounted on the moving platform, which travels along the x-axis with the constant velocity v at a height h_0. The incident angle of the surveillance antenna is set to θ and the shortest slant range from the origin to the radar is set to R_c. Therefore, the radar's position can be expressed as $(vt, -R_c sin\theta, h_0)$ and the slant range from an arbitrary point $P(x, y)$ to the radar is

$$r_R(t, x, y) = \sqrt{(R_c sin\theta + y)^2 + (x - vt)^2 + h_0^2} \tag{5.1}$$

where $t \in [y/v - T_L/2, y/v + T_L/2]$. T_L is the synthetic aperture time, which is equal to L/v. The yellow plane illustrates the wavefront of the DVB-S signal which is received by the radar as the reference signal. The reference signal on the wavefront propagates toward the target $P(x, y)$. It is reflected off the target and then received by the radar as the surveillance signal. Thus the difference of signal propagation path $r(t, x, y)$ between two antennas, illustrated as the black solid line, consists of the slant range $r_R(t, x, y)$ and the distance $r_T(t, x, y)$ from the imaging point P to this wavefront. $r_T(t, x, y)$ can be derived as

$$r_T(t, x, y) = |a(y + Rsin\theta) + b(x - vt) - ch_0| \tag{5.2}$$

where $t \in [y/v - T_L/2, y/v + T_L/2]$.

The relative motion between the radar and propgation direction of the DVB-S leads to a slight distortion in the received reference signal. As the radar moves along the x-axis, the wavefront across the radar will move forward or backward according to the AoA of the incident beam. Assuming that the transmitted DVB-S signal is defined as $s(t)$, the demodulated reference signal $s_{ref}(t)$ and surveillance signal $s_{sur}(t)$ can be expressed as

$$s_{ref}(t) = s(t + b \cdot vt)e^{j\frac{2\pi}{\lambda}b \cdot vt} \tag{5.3}$$

and

$$s_{sur}(t) = \int_{-\frac{W}{2}}^{\frac{W}{2}} \int_{vt-\frac{L}{2}}^{vt+\frac{L}{2}} \sigma(x, y)s_{ref}(t - \frac{r(t, x, y)}{c})e^{-j\frac{2\pi}{\lambda}r(t,x,y)}dxdy \tag{5.4}$$

respectively, where $\sigma(x, y)$ is the RCS of point (x, y), the center of beam footprint is $(0, vt)$, c is the light speed, and λ is the wavelength of the transmit beam.

5.1.2 Passive GCW-SAR Imaging Processing

The ideal matched filtering algorithm, i.e., back projection algorithm, for the passive GCW-SAR is proposed firstly. For each pixel of the observed scene, the imaging process is generally a cross-correlation over time period T_L between the surveillance signal and its location dependent reference signal. The most accurate ideal matched filtering algorithm is thus to reconstruct an arbitrary pixel (x_m, y_n) according to the equation

$$\begin{aligned}
&\int_{\frac{x_m}{v}-\frac{T_L}{2}}^{\frac{x_m}{v}+\frac{T_L}{2}} s_{sur}(t)s^*_{ref}(t-\frac{r(t,x_m,y_n)}{c})e^{j\frac{2\pi}{\lambda}r(t,x_m,y_n)}dt \\
&= \int_{-\frac{W}{2}}^{\frac{W}{2}}\int_{x_m-\frac{L}{2}}^{x_m+\frac{L}{2}} \sigma(x,y)\chi_p(x,y;x_m,y_n)dxdy
\end{aligned} \tag{5.5}$$

where the corresponding ambiguity function is expressed as

$$\begin{aligned}
\chi_p(x,y;x_m,y_n) = &\int_{\frac{x_m}{v}-\frac{T_L}{2}}^{\frac{x_m}{v}+\frac{T_L}{2}} s_{ref}(t-\frac{r(t,x,y)}{c})s^*_{ref}(t-\frac{r(t,x_m,y_n)}{c}) \\
&\cdot e^{j\frac{2\pi}{\lambda}(r(t,x_m,y_n)-r(t,x,y))}dt
\end{aligned} \tag{5.6}$$

The beam footprint consists of a set of uniformly distributed pixels with spacings along y and x axises equal to the range and azimuth resolutions, δ_y and δ_x, respectively. From the knowledge of the position of pixels and the trajectory of the passive radar, the location dependent reference signal of any pixel can be reconstructed from the received reference signal directly. After performing correlation, the passive SAR finally reconstructs a two-dimensional image.

Based on the geometry and the ideal matched filtering algorithm in the passive GCW-SAR, a novel passive PCD imaging algorithm is proposed as follows. Assume that $r(t, x_m, y_n)$ satisfies the condition, $r(t, 0, y_n) = r(t + \frac{x_m}{v}, x_m, y_n)$. The difference in correlation outputs between two adjacent pixels in azimuth just involves a Doppler frequency shift and a little time delay, and thus the purpose of the PCD algorithm is to reconstruct the pixels recursively in azimuth. The Doppler frequency shift corresponds to the variation of range $r(t, x, y)$. The distance $r_T(t, x, y)$ varies linearly, resulting in a constant Doppler frequency shift, but the slant range $r_R(t, x, y)$ has non-linear variation. Therefore, the entire correlation interval $[-T_L/2, T_L/2]$ is divided into P segments and define the time instants at the junctions of these segments as $t_p = pT_L/P - T_L/2$ for $p = 0, 1, ..., P-1$. The segmentation, linearization and their relationship with the correlation are shown in Fig. 5.2. The recursive procedure in each segment can be further explained as follows.

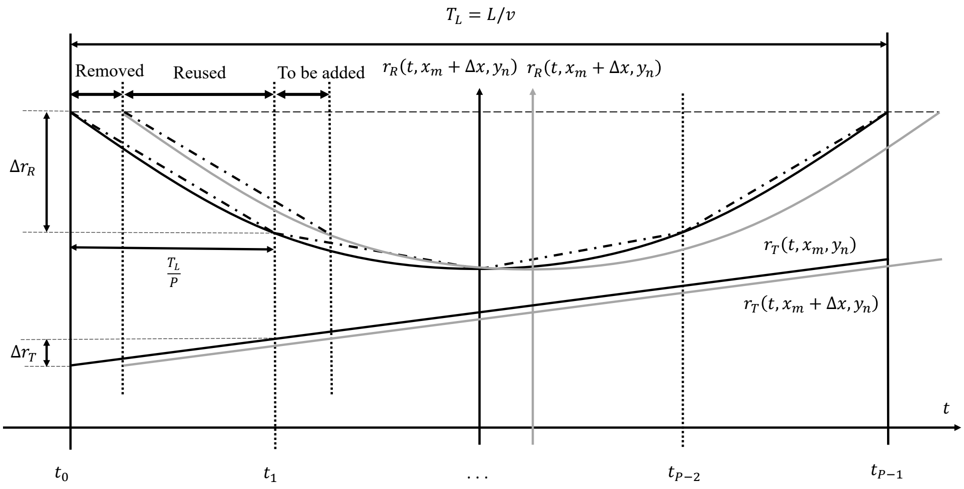

Figure 5.2 : Over the synthetic aperture L, the black solid curve indicates the slant range r_R of the pixel (x_m, y_n), which can be piecewise linearized into the black dot-dash linear segments; Black solid line indicates the distance r_T; The gray lines indicate the r_R and r_T for the next azimuth pixel $(x_m + \Delta x, y_n)$.

Assume that the cross-correlation in an integration interval $[t_p, t_{p+1}]$ has been obtained for the pixel (x_m, y_n). To calculate the cross-correlation in the integration interval $[t_p + \Delta x/v, t_{p+1} + \Delta x/v]$ for the pixel $(x_m + \Delta x, y_n)$, the cross-correlation obtained in the interval $[t_p, t_p + \Delta x/v]$ is first removed. It is easily seen in Fig. 2

that the correlation in the removed interval for the pixel (x_m, y_n) does not belong to the correlation for the pixel $(x_m + \Delta x, y_n)$. The second step is to compensate the Doppler frequency shift in the reused interval, which consists of two components: the first one is caused by the slant range difference,

$$r_{d_R} = r_R(t, x_m + \delta_x, y_n) - r_R(t, x_m, y_n) = \frac{\Delta x P(r_R(t_p, 0, y_n) - r_R(t_{p+1}, 0, y_n))}{T_L v} \tag{5.7}$$

and the second one is caused by the difference of r_T,

$$r_{d_T} = r_T(t, x_m + \Delta x, y_n) - r_T(t, x_m, y_n) = \Delta x \cdot b. \tag{5.8}$$

Therefore, the Doppler frequency shift can be compensated by multiplying $e^{-j2\pi/\lambda \cdot (r_{d_R} - r_{d_T})}$. The final step is to add the new integration in the added interval which only belongs to the pixel $(x_m + \Delta x, y_n)$.

As a result, the only difference between the PCD algorithms used in active and passive GCW-SAR is the compensation of the Doppler frequency shift, which is determined by the system geometry.

5.1.3 Simulation Results

Now consider a non-cooperative SS-BSAR with the following parameters: the antenna aperture is 1m, the radar velocity is 40m/s, the height of platform is 300m, the carrier frequency and bandwidth of DVB-S signal is 3GHz and 30MHz respectively, the normalized vector of AoA $\vec{I}$ is set to $(0.0099, -0.0995, 0.9950)$ and the incident angle of the radar θ is set to 45°.

Figs. 5.3 gives the two 9-point final focused SAR images reconstructed by RDA and PCD algorithms respectively. In conventional passive SAR with RDA, the ranging compression is performed block by block along the synthetic aperture, resulting in the sampling in azimuth, known as the slow time. With continuous wave reference signal, the RDA will introduce interference in the range compressed image.

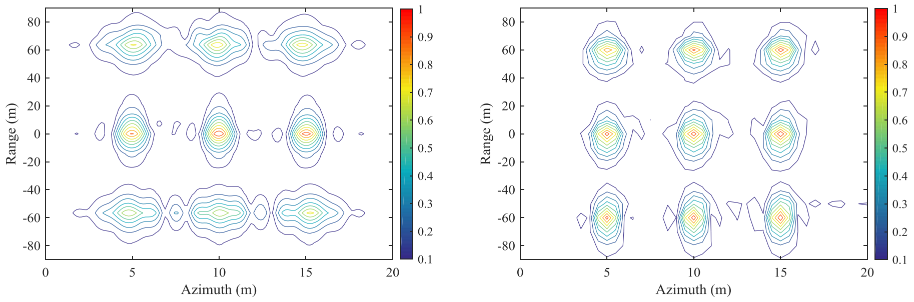

(a) (b)

Figure 5.3 : Comparison between RDA in passive SAR and PCD imaging in passive GCW-SAR: (a) RDA; (b) PCD.

The poor range compression will also have a negative impact on the further azimuth compression. Conversely, the PCD algorithm extends the integration interval to the synthetic aperture without the slow time sampling, and thus the interference between segments can be neglected. It is evidently shown that except the central pixels, the imaging performance of PCD is superior to that of RDA in passive SAR.

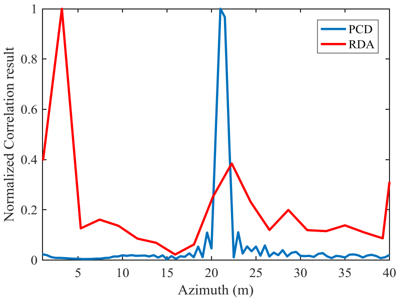

Figure 5.4 : Azimuth imaging performance comparison between RDA and PCD.

Fig. 5.4 gives the correlation output in azimuth for an one-point SAR image. Assume that the the number of azimuth samples is set to 20. It is evidently seen that the azimuth ambiguity cannot be suppressed with the low azimuth sampling rate. Conversely, the proposed SAR performs perfectly with the same number of segments $P = 20$, thus removing the intrinsic limitation in conventional passive SAR.

5.2 A Millimeter Wave GCW-SAR System with Deramp-on-Receive

In a GCW-SAR system, a high sampling rate to obtain the one-dimensional raw data is required according to the bandwidth of the received signal. On the other hand, to achieve a high azimuth resolution, a long synthetic aperture time is required, leading to increased computational cost. In this section, a novel active GCW-SAR system is proposed based on the deramp-on-receive principle as in a millimeter FMCW radar.

In FMCW radar, the received signal is mixed with a replica (reference signal) of the transmitted signal and down-converted to the baseband to produce the beat signal via a low-pass filter. Hence, the received bandwidth can be drastically reduced [30, 66]. Then, the down-sampled one-dimensional received signal can be obtained from the beat signal with the know transmitted waveform and synchronization. Finally, applying the PCD algorithm, an efficient GCW-SAR implementation is achieved. It is known that, with a conventional FMCW radar, the duration of useful beat signal in a chirp period is reduced as the target distance increases. However, the GCW-SAR reconstructs the image by performing cross-correlation of the received signals with location dependent reference signals. The targets are distinguished by the time correlation rather than frequency differences. Hence, with a triangular frequency modulated waveform, all of the beat signal components over the signalling period can be fully utilized in GCW-SAR to capture the maximum signal power.

As the azimuth resolution is theoretically equal to half of the antenna aperture which is inversely proportional to the synthetic aperture, achieving a high azimuth resolution requires a long synthetic aperture. With the PCD imaging adopted in the GCW-SAR, the slant range is approximated as multiple piecewise linear segments. If the synthetic aperture is long, and/or more accurate approximation is required, the number of linear segments must be increased, leading to increased computational complexity. In order to achieve high resolution imaging with low complexity, millimeter wave signal in the GCW-SAR is further proposed. Since the synthetic aperture is proportional to the wavelength of the transmitted signal given the antenna aperture, the proposed millimeter wave GCW-SAR will have short synthetic aperture once the wavelength is reduced to millimeter scale. With the same high azimuth resolution, a short synthetic aperture not only reduces the computational cost significantly, but also improves PCD image quality. Note that the length of the synthetic aperture will not restrict the image size in azimuth since the GCW-SAR imaging in azimuth direction is a recursive and on-going process.

5.2.1 GCW-SAR with Deramp-on-Receive

For simplicity, the GCW-SAR working in the flat-terrain stripmap geometry shown in Fig. 2.3 is considered, where the side-looking radar, at a height h_0, travels along the x-direction with a constant speed v. The instantaneous slant range and the time correlation output can be assumed the same as (3.1) and (3.3) in conventional GCW-SAR. In this subsection, the GCW-SAR deramping process is firstly described, then the beat signals produced by different transmitted waveforms are compared, and finally the effect of the deramp-on-receive to the PCD imaging performance is discussed.

5.2.1.1 RF Deramping at Receiver Frontend

The architecture of the GCW-SAR with deramp-on-receive is shown in Fig. 5.5. Assuming that $s(t)$ has a constant envelope which is also normalized to 1 for simplicity, i.e., $|s(t)|^2 = s^*(t)s(t) = 1$, the received baseband signal can be expressed as

$$s_r(t) = s_r(t)s^*(t)s(t) = s_b(t)s(t) \tag{5.9}$$

where

$$s_b(t) = s_r(t)s^*(t) \tag{5.10}$$

is the beat signal similar to the one used in an FMCW radar. Expressing the transmitted and received radio frequency signals as $S(t) = Re\{s(t)e^{j2\pi f_c t}\}$ and $S_r(t) = Re\{s_r(t)e^{j2\pi f_c t}\}$ respectively, $Re\{s(t)e^{j2\pi f_c t}\} \cdot S_r(t) = \frac{1}{2}Re\{s_r(t)s(t)e^{j4\pi f_c t}\} + \frac{1}{2}Re\{s_b(t)\}$ and $Im\{s(t)e^{j2\pi f_c t}\} \cdot S_r(t) = \frac{1}{2}Im\{s_r(t)s(t)e^{j4\pi f_c t}\} - \frac{1}{2}Im\{s_b(t)\}$. After removing the high frequency components with carrier frequency $2f_c$ by low-pass

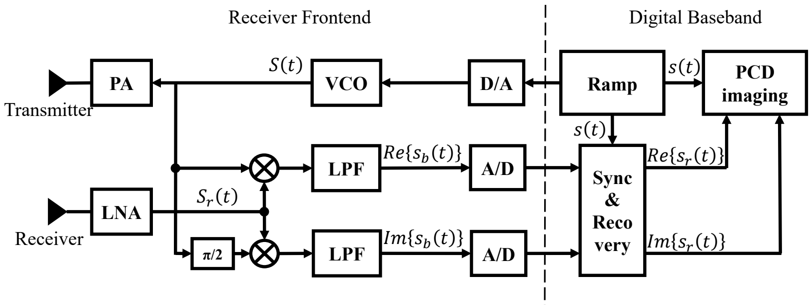

Figure 5.5 : Block diagram of GCW-SAR with deramp-on-receive, where PA and LNA denote power amplifier and low noise amplifier respectively, VCO denotes voltage controlled oscillator producing carrier frequency, A/D and D/A are analog-digital and digital-analog converters and Sync represents time synchronization. The down-sampled received signal can be obtained after the "Sync & Recovery" module.

filters (LPFs), It is seen that the beat signal $s_b(t)$ can be obtained by using the I/Q demodulator at the RF frontend. As the bandwidth of the beat signal $s_b(t)$ is much smaller than the received signal $s_r(t)$, only lower sampling rate ADCs are required. With the known transmitted signal frequency ramp and the sampling time of the A/D converters, the down-sampled transmitted baseband signal $s(t)$ can be re-generated. Once the beat signal is obtained, the down-sampled version of the original received signal can be easily recovered from (5.9) in digital baseband.

Though passing through the low-pass filters introduces a time delay to the beat signal, it can be compensated after time synchronization in digital baseband. From the block diagram of the GCW-SAR with deramp-on-receive, it is seen that the differences between the FMCW radar system and the proposed GCW-SAR are the additional time synchronization and the imaging process in digital baseband. Their RF deramping processes in receiver frontend are the same. Therefore, the GCW-SAR with the deramp-on-receive can be easily implemented by using the existing FMCW radar hardware.

5.2.1.2 Transmitted Waveform Selection

The conventional FMCW radar adopts the up/down-chirp signal, producing the unwanted high frequency components in the beat signal. After low-pass filtering, these components are removed so that the corresponding received signal components are lost. In order to completely pass through the low-pass filter, the highest instantaneous frequency of the beat signal must be smaller than the cut-off frequency of the low-pass filter. Therefore, a triangular frequency modulated waveform is selected for the proposed GCW-SAR, which not only retains the characteristics of the chirp signal but also produces beat signal without high frequency components. Considering the phase continuity, over the period $[0, T_r)$, the triangular frequency modulated waveform can be expressed as

$$s(t) = \begin{cases} e^{j\pi K_r t(t-\frac{T_r}{2})}, t \in [0, \frac{T_r}{2}) \\ e^{-j\pi K_r (t-\frac{T_r}{2})(t-T_r)}, t \in [\frac{T_r}{2}, T_r) \end{cases} \tag{5.11}$$

where $K_r = 2B/T_r$ is the chirp rate and B is the bandwidth of the transmitted signal.

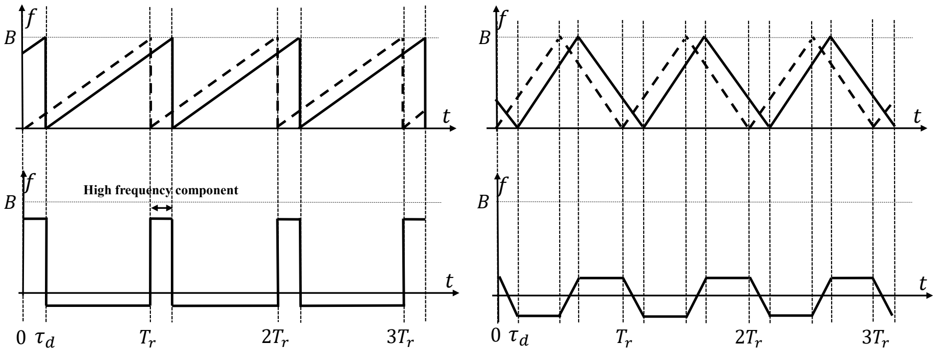

(a) (b)

Figure 5.6 : Beat frequency produced by up-chirp waveform and triangular frequency modulated waveform respectively: (a) up-chirp waveform; (b) triangular frequency modulated waveform.

Fig. 5.6 depicts the frequency variations of the beat signals with respect to time t produced by the up-chirp waveform and the triangular frequency modulated waveform respectively. With the up-chirp waveform, a high frequency signal is obtained at the start of each transmitted repetition period due to sharp frequency transition as shown in Fig. 5.6 (a), and it will be filtered out after passing through a narrow-bandwidth low-pass filter. With the triangular frequency modulated waveform, there is no sharp frequency transition so that the deramping will never produce high beat frequency as shown in Fig. 5.6 (b).

5.2.1.3 PCD Imaging in Digital Baseband

Without deramp-on-receive, from (3.19), the PCD imaging process in digital domain can be expressed as

$$\begin{aligned}
&I_p((m+1)\Delta x, y_n) = I_p((m+1)vT_s, y_n) \\
&= I_p(mvT_s, y_n)e^{j2\pi f_{D_p}(y_n)T_s} \\
&- T_s s_r((m+1)T_s + t_p)s^*((m+1)T_s + t_p - \frac{2r(t_p, 0, y_n)}{c})e^{j\frac{4\pi}{\lambda}r(t_p,0,y_n)} \\
&+ T_s s_r((m+1)T_s + t_{p+1})s^*((m+1)T_s + t_{p+1} - \frac{2r(t_{p+1}, 0, y_n)}{c})e^{j\frac{4\pi}{\lambda}r(t_{p+1},0,y_n)}.
\end{aligned} \tag{5.12}$$

To satisfy the Nyquist–Shannon sampling theorem, the sampling rate $1/T_s$ should be larger than the transmitted bandwidth B. After applying the deramp-on-receive technique to the GCW-SAR, the sampling rate can be significantly reduced due to the much more narrow bandwidth of the received beat signal. Assuming that the sampling interval of the beat signal is defined as T_b, Eq. (5.12) can be derived as

$$\begin{aligned}
&I_p((m+1)\Delta x, y_n) = I_p((m+1)vT_b, y_n) \\
&= I_p(mvT_b, y_n)e^{j2\pi f_{D_p}(y_n)T_b} \\
&- T_b s_r((m+1)T_b + t_p)s^*((m+1)T_b + t_p - \frac{2r(t_p, 0, y_n)}{c})e^{j\frac{4\pi}{\lambda}r(t_p,0,y_n)} \\
&+ T_s s_r((m+1)T_b + t_{p+1})s^*((m+1)T_b + t_{p+1} - \frac{2r(t_{p+1}, 0, y_n)}{c})e^{j\frac{4\pi}{\lambda}r(t_{p+1},0,y_n)}
\end{aligned} \tag{5.13}$$

where the azimuth spacing Δx can be extended from $T_s v$ to $T_b v$. Based on (5.13), the impacts of the deramping operation on the PCD imaging performance are elaborated from the range and azimuth directions respectively as follows.

- In the range direction, the images at different y_n are reconstructed independently by correlating a location dependent reference signal with the received signal. According to the pulse compression theory, the range ambiguity is determined by the time delay between the reference and received signals. It is easily seen in (11) that the time delay $2r(t_p, 0, y_n)/c$ in PCD is independent of the sampling rate of the received signal, $1/T_b$. Therefore, PCD imaging performance is hardly affected by deramping operation in the range direction.

- In the azimuth direction, the azimuth imaging spacing in the original GCW-SAR is much shorter than the azimuth resolution since the sampling rate of the received signal is much higher than the Doppler bandwidth, leading to a large amount of redundant imaging points and hence significant computational cost for the PCD implementation. The deramp-on-receive can drastically reduce the sampling rate due to the low bandwidth beat signal and the down-sampled received signal can be recovered, thus largely improving the imaging efficiency. The azimuth spacing in (5.13) is extended to $T_b v$ and the computational cost is further reduced by T_b/T_s times.

Note that the recovered down-sampled received signal is not suitable to be used in the conventional imaging algorithms based on two-dimensional (fast time and slow time) raw data structure, e.g., the range-Doppler algorithm, since the range compression is achieved in fast time dimension by the convolution between the received signal and a reference signal. The fast time sampling with low sampling rate would cause significant range ambiguity.

5.2.2 GCW-SAR with Millimeter Wave Signal

According to the SAR principle, the range and azimuth resolutions are determined by the transmitted bandwidth B and the physical antenna aperture L_a respectively, i.e.,

$$\delta_y = \frac{c}{2Bsin\theta} \tag{5.14}$$

and

$$\delta_x = \frac{\lambda R_c}{2L} = \frac{L_a}{2} \tag{5.15}$$

where λ denotes the transmitted wavelength. From (5.15), the synthetic aperture can be expressed as

$$L = \frac{\lambda R_c}{L_a} \tag{5.16}$$

which is determined by the transmitted wavelength, the physical antenna aperture, and the distance from the target. Assuming the same distance R_c and the physical antenna aperture L_a, the synthetic aperture can be shortened by reducing the transmitted wavelength as seen in (5.16).

In conventional SAR, the synthetic aperture determines the imaging azimuth dimension since the image is reconstructed by focusing the two-dimensional raw data matrix. To achieve a large image in azimuth, conventional SAR has to achieve several sub-images along the flight trajectory block by block and then performs the image stitching to form a large image, e.g., Mosaic SAR [80, 81]. However, shortening the synthetic aperture obviously increases the number of the sub-images in azimuth, hence complicating the data stitching. Therefore, it is difficult for conventional SAR system to achieve a large image by using the millimeter wave FMCW radar. In GCW-SAR, however, the imaging size in azimuth is independent of the synthetic aperture since the image is reconstructed recursively in azimuth. A large GCW-SAR image in azimuth can be directly achieved without data stitching. This nature allows for millimeter transmitted signal to be used in GCW-SAR without restriction in azimuth dimension. The advantages of millimeter wave GCW-SAR system with deramp-on-receive are elaborated in various aspects, including high PCD image quality, low computational complexity, and high range and azimuth resolutions.

5.2.2.1 High Image Quality

From (4.20) and (4.21), the PCD image quality can be evaluated by the PCD imaging error derived as

$$\varepsilon^2 = 2 - 2Re\{\sqrt{\frac{2Q}{\pi}}e^{j\frac{\pi}{2Q}}\Big(C(\sqrt{\frac{\pi}{2Q}}) - jS(\sqrt{\frac{\pi}{2Q}})\Big)\} \tag{5.17}$$

where $Q = L_a P^2/L$ is defined as the image quality factor, and $C(.)$ and $S(.)$ are the Fresnel integrals respectively. As seen in Fig. 4.3, the PCD imaging error becomes smaller as Q increases, indicating that a larger Q value leads to a better PCD image quality. From (5.16), the PCD image quality factor can be further expressed as

$$Q = \frac{L_a^2 P^2}{\lambda R_c} = \frac{L_a^2 P^2 f_c}{c R_c}. \tag{5.18}$$

It is seen that, the shorter the wavelength of the transmitted signal is, the larger the quality factor. With the same L_a and P, adopting the millimeter wave transmitted signal can achieve a high image quality.

5.2.2.2 Low Complexity

The GCW-SAR adopts PCD imaging algorithm which approximates the range curve as piecewise linear segments. A long synthetic aperture will increase the number of the linear segments. Given the same image quality and resolutions, the number of linear segments P can be significantly reduced by using a shorter wavelength transmitted signal as seen in (5.18), thus leading to a low computational complexity and reduced memory requirement. Assuming the same observed scene where the number of range pixels is N, computational complexity of the millimeter wave GCW-SAR and its required memory are compared with those of the conventional one as follows.

The PCD algorithm updates the image in azimuth recursively whenever the system obtains a new received sample. Assuming that the number of the received samples in the conventional GCW-SAR is $N \times N$, an $N \times N^2$ pixel image over the observed scene is achieved. Referring to, imaging each pixel needs $3P + 2$ complex multiplications, and thus $(3P + 2) \times N^3$ complex multiplications are required in the conventional GCW-SAR. However, after adopting the millimeter wave transmitted signal with shortened synthetic aperture, the deramp-on-receive can decrease the number of the received samples to $N \times N/(T_b/T_s)$. Hence the computational cost is significantly reduced. Assuming that the number of the linear segments is further reduced to P/N_P, the proposed GCW-SAR system only requires $(3P/N_P + 2) \cdot N^2 \cdot N/(T_b/T_s)$ complex multiplications.

Assuming that the number of received samples over a transmitted period is N_{period} and the number of the range pixels is N, the number of memory units used in the PCD imaging of the conventional GCW-SAR is equal to $N_{period} + N \times (3P + 2)$ as seen in Fig. 3.3. In the proposed GCW-SAR, the N_{period} and P have been reduced to $N_{period}/(T_b/T_s)$ and P/N_P respectively and thus the number of memory units is $N_{period}/(T_b/T_s) + N \times (3P/N_P + 2)$.

5.2.2.3 High Image Resolutions

As seen in (5.14) and (5.15), the range and azimuth resolutions are determined by the transmitted signal bandwidth and the antenna aperture respectively. Using the millimeter wave signal allows a wider transmitted signal bandwidth and hence a higher range resolution. On the other hand, a high azimuth resolution requires a short antenna aperture which leads to a long synthetic aperture and increases the computational cost. Based on (5.16), the synthetic aperture can be shortened by using the millimeter wave radar. Given the high image quality and the low computational cost, a higher azimuth resolution $L_a/2$ can be achieved by transmitting a shorter transmitted wavelength as seen in (5.18). Therefore, the millimeter wave FMCW radar can provide high image resolutions in both range and azimuth.

5.2.3 Simulation Results

In this subsection, comprehensive performance evaluation of the novel GCW-SAR and comparison with the millimeter wave FMCW-SAR are made through simulation in an airborne stripmap SAR geometry with the following parameters: platform altitude 500 m, speed of radar platform 45 m/s, the transmitted bandwidth 250 MHz, and R_c=1113.3 m. The noise at the receiver is not considered for simplicity.

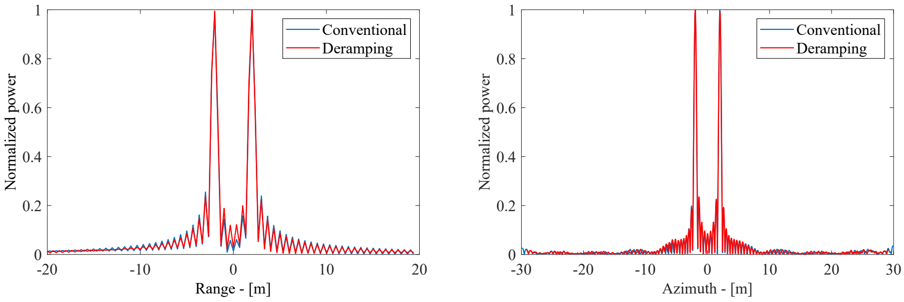

(a) (b)

Figure 5.7 : Imaging performance comparison between conventional GCW-SAR and GCW-SAR based on deramp-on-receive: (a) range direction and (b) azimuth direction.

5.2.3.1 *Performance of GCW-SAR Imaging from Beat Signal*

Deramp-on-receive can significantly reduce the sampling rate of the received signal. In the first simulation, the impact of the deramping operation on PCD imaging performance is investigated. The point targets are located at $(-2\ \mathrm{m}, 0)$, $(2\ \mathrm{m}, 0)$, $(0, -2\ \mathrm{m})$ and $(0, 2\ \mathrm{m})$. The antenna aperture L_a is 0.8 m, the carrier frequency is 7 GHz, the number of linear segments P is 40, and the triangular frequency modulated waveform is adopted. The full imaging result is shown in Fig. 6, and the range and azimuth imaging results at $x_m = 0$ and $y_n = 0$ are shown

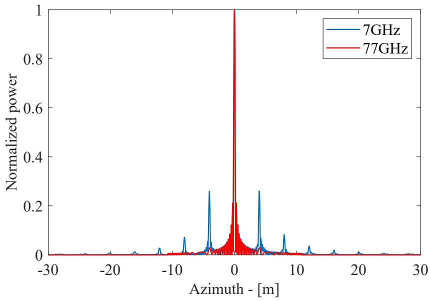

Figure 5.8 : Azimuth imaging comparison using $f_c = 7$ GHz and $f_c = 77$ GHz when the $L_a = 0.4$ m and $P = 20$.

in Fig. 5.7 respectively. It is evident from the imaging results shown in Fig. 7 that the deramp-on-receive in GCW-SAR system does not cause any performance degradation. As the range ambiguity is determined by the time delay of the reference signal with PCD imaging, reducing the samples in the received signal does not affect the range resolution, as shown in Fig. 5.7 (a). In azimuth, reducing the received samples improves the imaging efficiency without azimuth resolution degradation, as shown in Fig. 5.7 (b).

5.2.3.2 High Image Quality by GCW-SAR with Millimeter Wave Signal

In the second simulation experiment, the impact of changing carrier frequency on the image quality of the GCW-SAR is investigated. With the triangular frequency modulated waveform, an image with a point target at $(0, 0)$ is considered. The antenna aperture L_a is 0.4 m, and the number of linear segment P is 20. The image quality factor Q as a function of the carrier frequency has been described in (5.18), where the Q is proportional to the carrier frequency. The images in azimuth with 7 GHz and 77 GHz carrier frequencies respectively are given in Fig. 5.8. The results show that the 77 GHz millimeter wave radar can significantly improve the image quality from 1.34 to 14.81 compared with the 7 Ghz radar. With

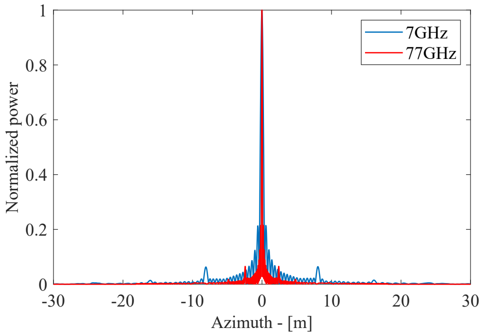

Figure 5.9 : Azimuth imaging comparison using $f_c = 7$ GHz and $f_c = 77$ GHz when the $Q = 5.39$ and $P = 20$.

7 GHz carrier frequency, $P = 20$ is not enough to approximate the slant range over the 119 m synthetic aperture. However, with 77 GHz carrier frequency, the synthetic aperture is shortened to 11 m, thus drastically reducing the error of slant range approximation. Moreover, assuming that the echoes reflected from any two targets whose spacing is larger than twice synthetic aperture are independent, the interference from the sidelobes can be also suppressed by shortening the synthetic aperture. As seen in Fig. 8, with 77 GHz carrier frequency, the sidelobes can only impact on the image within the interval $(-11$ m, 11 m$)$.

5.2.3.3 High Azimuth Resolution by GCW-SAR with Millimeter Wave Signal

In the third simulation experiment, given the same Q and P, the azimuth resolution by using different carrier frequencies is compared. Assume that the Q is 5.39 and P is 20. Adopting the triangular frequency modulated waveform and an image with one point target at $(0, 0)$, the azimuth imaging results with the 7 GHz and 77 GHz carrier frequencies respectively are provided in Fig. 5.9, which shows that a higher azimuth resolution image with the same Q and P can be achieved with the increase of the carrier frequency. Maintaining the same $Q = 5.39$ and $P = 20$, a

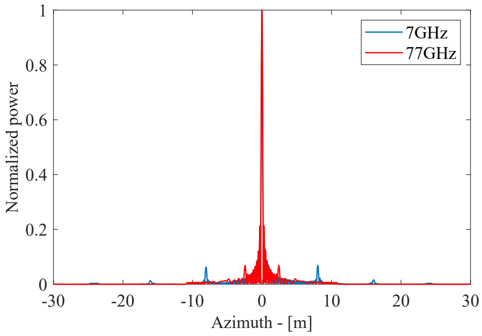

Figure 5.10 : Azimuth imaging comparison using $f_c = 7$ GHz and $f_c = 77$ GHz when the $L_a = 0.4$ m and $Q = 5.39$.

0.12 m azimuth resolution can be achieved when transmitting 77 GHz millimeter wave, while transmitting 7 GHz signal can only achieve a 0.4 m azimuth resolution.

5.2.3.4 Low Complexity by GCW-SAR with Millimeter Wave Signal

The impact of changing carrier frequency on the number of linear segments in GCW-SAR is investigated in this simulation experiment. The L_a is set to 0.4 m. The triangular frequency modulated waveform is adopted. Given the same $Q = 5.39$ and $L_a = 0.4$ m, an image with one point target at $(0, 0)$ is obtained by using the 7 GHz and 77 GHz carrier frequencies respectively as shown in Fig. 5.10. To achieve the same image quality $Q = 5.39$, the P must ba as large as 40 in the 7 GHz imaging but only 12 in the 77 GHz imaging, thus saving much computational cost.

5.2.3.5 Multi-point GCW-SAR Imaging with Millimeter Wave Radar

In the final simulation experiment, the multi-point GCW-SAR imaging between the 7 GHz system and the 77 GHz millimeter wave system are compared. The L_a and P are set to 0.4 m and 20 respectively, and the triangle frequency modulated waveform is adopted in the two imaging scenarios. By transmitting the 250 MHz bandwidth signals, the reconstructed 7 GHz and 77 GHz images are shown in Fig.

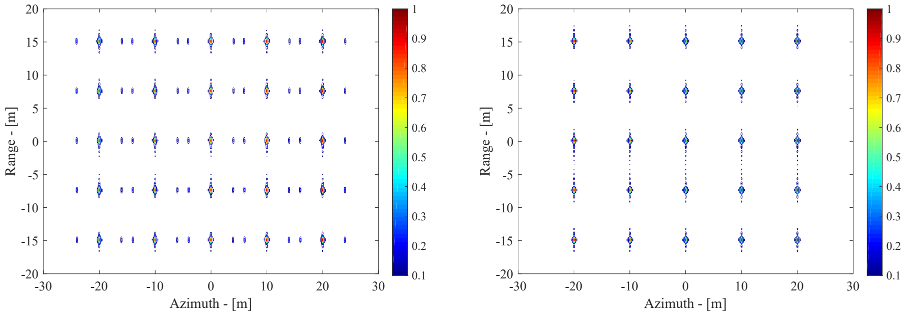

(a)

(b)

Figure 5.11 : Multi-point imaging performance comparison between (a) 7 GHz GCW-SAR and (b) 77 GHz GCW-SAR, where $L_a = 0.4$ m and $B = 250$ MHz.

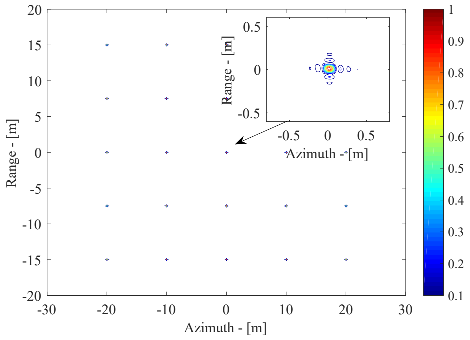

Figure 5.12 : Multi-point 77 GHz GCW-SAR imaging with high range and azimuth resolution where $L_a = 0.2$ m and $B = 2.5$ GHz.

5.11 (a) and (b) respectively. It is evident that 77 Ghz millimeter wave GCW-SAR performs much better than the 7 GHz one. To achieve higher range and azimuth resolutions, a wider bandwidth 2.5 GHz and a shorter antenna aperture $L_a = 0.2$ m are further used in the 77 Ghz millimeter wave GCW-SAR. To keep the same image quality Q, the P is increased to 40 and the imaging result is shown in Fig. 12, which validates the capability of the 77-GHz GCW-SAR system to achieve higher imaging resolutions.

5.3 Summary

In this chapter, two special GCW-SAR systems, i.e., passive GCW-SAR system and a millimeter wave active GCW-SAR sytem with deramp-on-receive, are developed.

In the first section, the passive GCW-SAR system is developed. By analyzing the geometry and the reference and received signals of the passive SAR system, a modified PCD algorithm is proposed to reconstruct the image recursively along the flight path of the radar based on the constant Doppler frequency shift approximation in segmented range curve. The proposed passive GCW-SAR removes the limitations caused by the slow time sampling, thus achieving a high resolution and wide-swath SAR image with good quality.

A novel active GCW-SAR system based on a millimeter wave FMCW radar is developed in the second section. It is seen that with deramp-on-receive frontend and PCD imaging algorithm the GCW-SAR not only works well with down-sampled received signal but also can be easily implemented with existing FMCW radar hardwares. The shortened synthetic aperture due to the use of millimeter wave signalling results in a number of advantages, such as improved image quality, high imaging resolutions, and reduced computational complexity. It is believed that the proposed millimeter wave GCW-SAR will find wide applications because of its high resolution and low complexity imaging capability.

Chapter 6

A Millimeter Wave GCW-SAR Experimental System

This chapter presents a GCW-SAR experimental system composed of a millimeter wave FMCW radar sensor and a linear moving platform, which contributes to the experimental demonstration of the GCW-SAR concept proposed in the earlier chapters. From the receiver frontend to the digital imaging process, all of the GCW-SAR system development issues are presented in detail in this chapter.

6.1 System Configuration

This experimental system is built based on the millimeter wave GCW-SAR with deramp-on-receive presented in Chapter 5, where the AWR1843 single-chip 77-GHz FMCW radar sensor made by Texas Instruments [82] is adopted and the imaging processing in digital domain is performed by a personal computer (PC). The whole system is composed of receiver frontend subsystem, radar control subsystem, positioning control subsystem and the digital imaging subsystem, and its block diagram is depicted in Fig. 6.1.

The receiver frontend subsystem is processed in the AWR1843 FMCW radar sensor by using the deramp-on-receive technique as seen in Fig. 5.5, where a complex beat signal can be acquired and transferred to the PC. The radar control system has been integrated in the AWR1843 evaluation module, where antenna, transmitted waveform, chirp period, and time synchronization can be selected manually via a graphical user interface (GUI) installed in the PC. The corresponding position

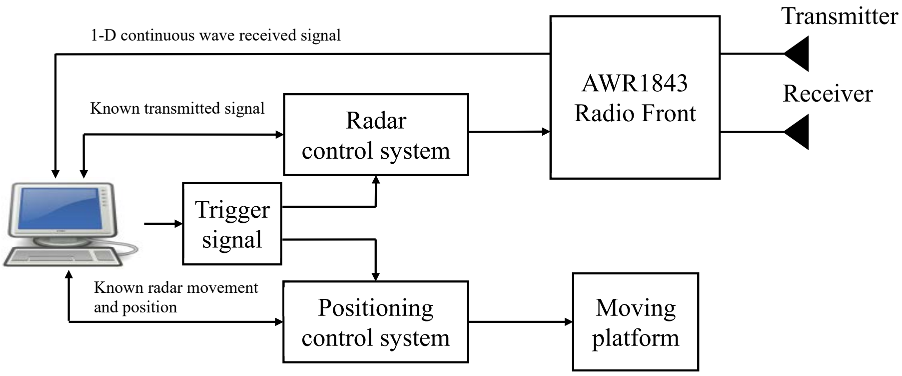

Figure 6.1 : Block diagram of GCW-SAR experimental system.

control system, made by FUYU Technology company in China, Chengdu, is an independent micro controller [83] connected to a stepping motor, and can be also manipulated via a GUI installed in the PC, where the platform moving speed and its start location can be initialized. Meanwhile, both of the radar and platform parameters setting can be transferred to the digital imaging subsystem. Finally, the decimated PCD algorithm combined with the recovery of the received signal is conducted in the digital imaging subsystem and a GCW-SAR image can be reconstructed recursively.

6.2 Receiver Frontend Subsystem

This section describes the the receiver frontend subsystem from two aspects, the antenna and the RF circuit.

The AWR1843 FMCW radar sensor includes onboard-etched antennas for its three transmitters and four receivers. Here, a single channel mode within one transmit and one receive antenna is adopted and the antenna peak gain is larger than 10.5 dBi. The radiation pattern of the antenna can be seen in the datasheet of the AWR1843 evaluation module, where the horizontal and elevation 3dB-beamwidths are ±28 and ±14 degrees respectively. Note that the AWR1843 made by TI is an

FMCW radar sensor used in the automotive industry for applications such as avoiding collision of cars. Although the antenna is not designed for the FMCW-SAR, it can be applied to the GCW-SAR system since the imaging size of the GCW-SAR is independent of the length of the synthetic aperture.

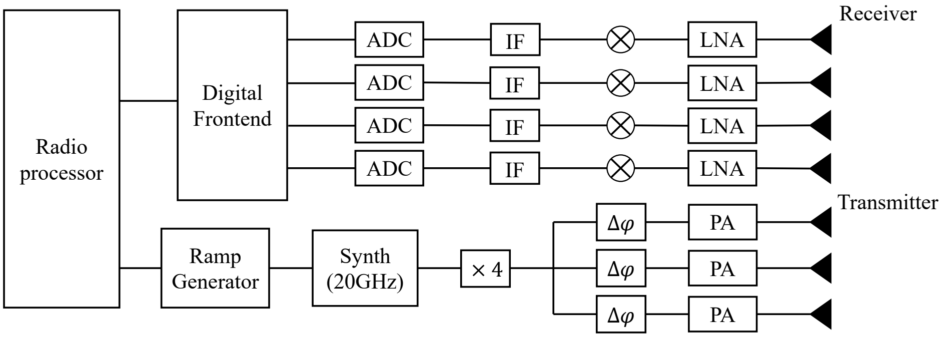

Figure 6.2 : Block diagram of RF circuit in the AWR1843.

The RF and analog circuit connected to the antenna consists of synthesizer, PA, LNA, mixer, intermediate frequencies (IF), and ADC. The block diagram of RF circuit in the AWR1843 can be shown in Fig. 6.2. With the known transmitted waveform and period, the baseband transmitted chirp signal is produced repeatedly by the ramp generator. After passing through the synthesizer, power amplifiers and additional phase shifters, a RF millimeter wave chirp signals are emitted towards the observed scene. A receive channel is composed of an LNA, mixer, IF filtering, ADC, and decimation in digital frontend. Fortunately, the AWR1843 RF circuits can produce a complex beat signal based on the deramp-on-receive seen in Fig. 5.5, which uses quadrature mixer and dual IF and ADC chains to provide complex I and Q outputs. This complex beat signal is then transferred to the PC used by the digital subsystem.

6.3 Radar Control Subsystem

TI company provides us a GUI called “mmWaveStudio” to operate the AWR1843 radar sensor, where the selection of the radar parameters setting can be conducted. To run this GUI, a PC is connected by the USB cable to this radar sensor, the required software package is installed, and the AWR1843Boost startup is initialized.

The connection operation is firstly described as seen in Fig. 6.3. The Sense-on-Power (SOP) mode is set to debug mode via the jumper in the AWR1843 evaluation module and the COM Port enumerated as “XDS110 Class Application/User UART” is selected for RS232 operations to allow firmware download and enable the device for characterization purposes. The PC host communicates with the AWR1843 by using the serial peripheral interface (SPI) interface. Once the firmware is downloaded, click the SPI connection and RF Power-up buttons.

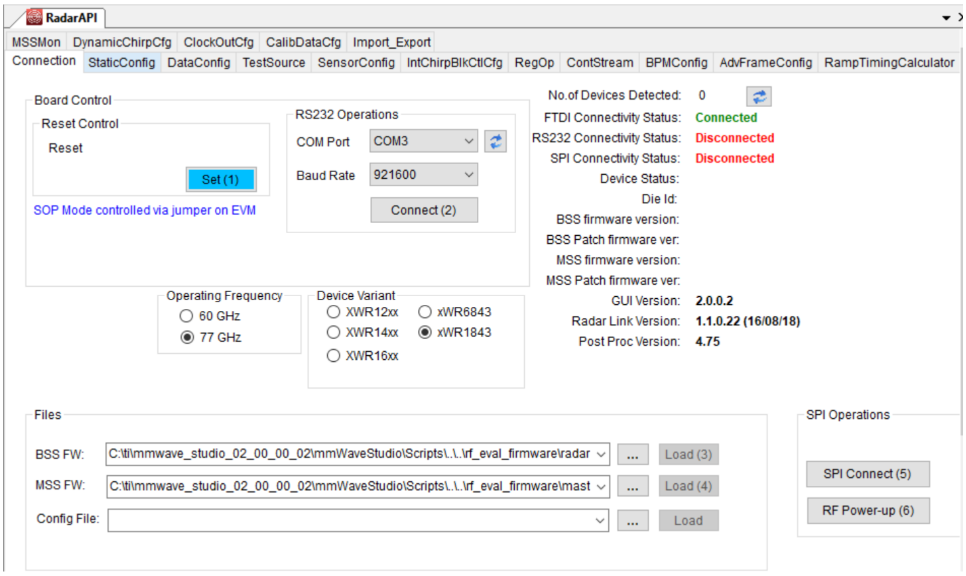

SOP Mode controlled via jumper on EVM

COM Port: COM3
Baud Rate: 921600

○ 60 GHz
● 77 GHz

○ XWR12xx
○ XWR14xx
○ XWR16xx
○ xWR6843
● xWR1843

No.of Devices Detected: 0
FTDI Connectivity Status: Connected
RS232 Connectivity Status: Disconnected
SPI Connectivity Status: Disconnected
Device Status:
Die Id:
BSS firmware version:
BSS Patch firmware ver:
MSS firmware version:
MSS Patch firmware ver:
GUI Version: 2.0.0.2
Radar Link Version: 1.1.0.22 (16/08/18)
Post Proc Version: 4.75

BSS FW: C:\ti\mmwave_studio_02_00_00_02\mmWaveStudio\Scripts\..\..\rf_eval_firmware\radar
MSS FW: C:\ti\mmwave_studio_02_00_00_02\mmWaveStudio\Scripts\..\..\rf_eval_firmware\mast
Config File:

Figure 6.3 : Connection tab in the mmWaveStudio.

Then, the number of transmit and receive channels, the data format of the ADC input, and the frequency configuration are determined in the static configuration tab. As seen in Fig. 6.4, Tx0 and Rx0 are selected to construct a single channel

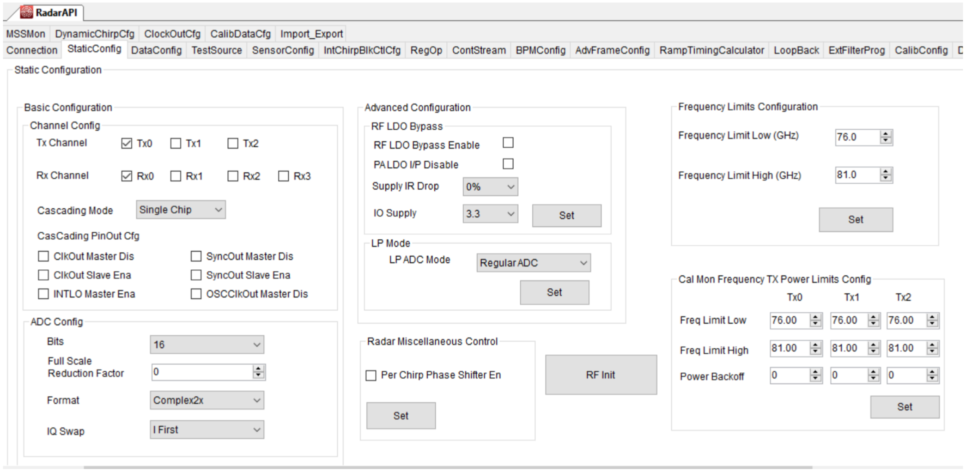

Static Configuration

Basic Configuration

Channel Config

Tx Channel ☑ Tx0 ☐ Tx1 ☐ Tx2

Rx Channel ☑ Rx0 ☐ Rx1 ☐ Rx2 ☐ Rx3

Cascading Mode: Single Chip

CasCading PinOut Cfg

☐ ClkOut Master Dis ☐ SyncOut Master Dis
☐ ClkOut Slave Ena ☐ SyncOut Slave Ena
☐ INTLO Master Ena ☐ OSCClkOut Master Dis

ADC Config

Bits: 16
Full Scale Reduction Factor: 0
Format: Complex2x
IQ Swap: I First

Advanced Configuration

RF LDO Bypass

RF LDO Bypass Enable ☐
PALDO I/P Disable ☐
Supply IR Drop: 0%
IO Supply: 3.3

LP Mode

LP ADC Mode: Regular ADC

Radar Miscellaneous Control

☐ Per Chirp Phase Shifter En

Frequency Limits Configuration

Frequency Limit Low (GHz): 76.0
Frequency Limit High (GHz): 81.0

Cal Mon Frequency TX Power Limits Config

	Tx0	Tx1	Tx2
Freq Limit Low	76.00	76.00	76.00
Freq Limit High	81.00	81.00	81.00
Power Backoff	0	0	0

Figure 6.4 : Static configuration in the mmWaveStudio.

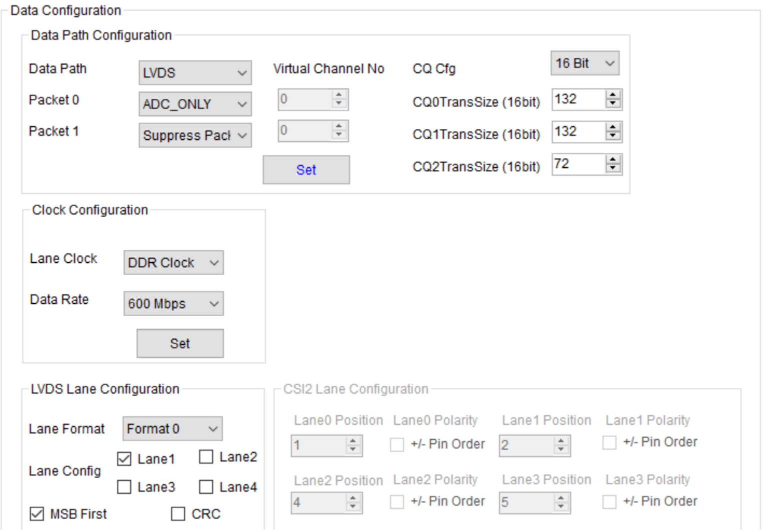

Data Configuration

Data Path Configuration

Data Path: LVDS
Packet 0: ADC_ONLY
Packet 1: Suppress Pacl
Virtual Channel No: 0
Virtual Channel No: 0
CQ Cfg: 16 Bit
CQ0TransSize (16bit): 132
CQ1TransSize (16bit): 132
CQ2TransSize (16bit): 72

Clock Configuration

Lane Clock: DDR Clock
Data Rate: 600 Mbps

LVDS Lane Configuration

Lane Format: Format 0
Lane Config: ☑ Lane1 ☐ Lane2 ☐ Lane3 ☐ Lane4
☑ MSB First ☐ CRC

CSI2 Lane Configuration

Lane0 Position: 1
Lane0 Polarity: ☐ +/- Pin Order
Lane1 Position: 2
Lane1 Polarity: ☐ +/- Pin Order
Lane2 Position: 4
Lane2 Polarity: ☐ +/- Pin Order
Lane3 Position: 5
Lane3 Polarity: ☐ +/- Pin Order

Figure 6.5 : Data configuration in the mmWaveStudio.

for the 1-D data acquisition, and a complex 16-bit 1-D data can be obtained. To maximize the range resolution, the widest frequency range is set from 76 GHz to 81 GHz. To transfer a large amount of received data to the PC, the DCA1000EVM data capture card is used and the data path format can be set in the data configuration tab shown in Fig. 6.5.

Afterwards, the transmitted waveform can be generated by using the sensor

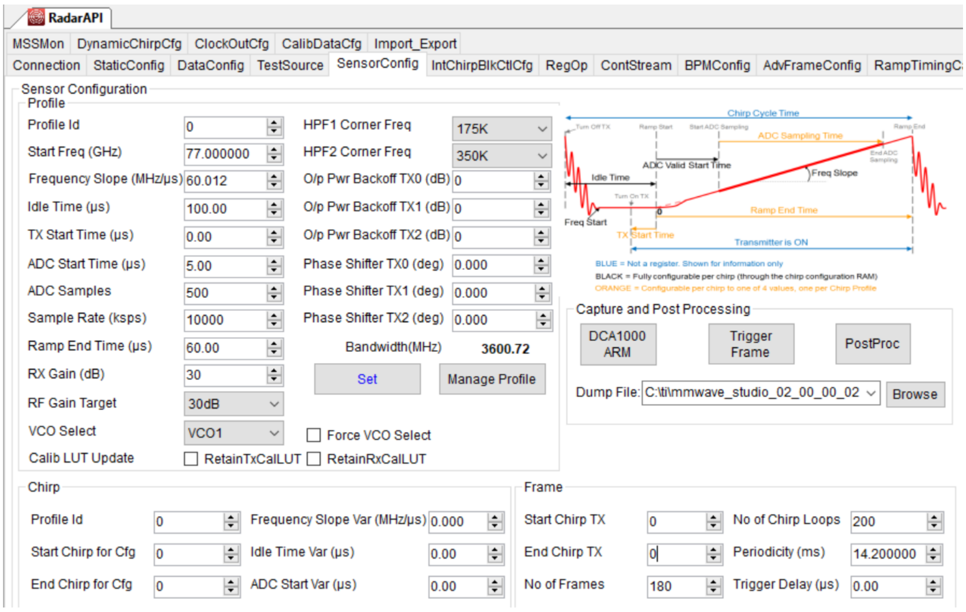

Sensor Configuration

Profile

Profile Id: 0
Start Freq (GHz): 77.000000
Frequency Slope (MHz/μs): 60.012
Idle Time (μs): 100.00
TX Start Time (μs): 0.00
ADC Start Time (μs): 5.00
ADC Samples: 500
Sample Rate (ksps): 10000
Ramp End Time (μs): 60.00
RX Gain (dB): 30
RF Gain Target: 30dB
VCO Select: VCO1
Calib LUT Update: ☐ RetainTxCalLUT ☐ RetainRxCalLUT
HPF1 Corner Freq: 175K
HPF2 Corner Freq: 350K
O/p Pwr Backoff TX0 (dB): 0
O/p Pwr Backoff TX1 (dB): 0
O/p Pwr Backoff TX2 (dB): 0
Phase Shifter TX0 (deg): 0.000
Phase Shifter TX1 (deg): 0.000
Phase Shifter TX2 (deg): 0.000
Bandwidth(MHz): 3600.72
☐ Force VCO Select

BLUE = Not a register. Shown for information only
BLACK = Fully configurable per chirp (through the chirp configuration RAM)
ORANGE = Configurable per chirp to one of 4 values, one per Chirp Profile

Capture and Post Processing

Dump File: C:\ti\mmwave_studio_02_00_00_02

Chirp

Profile Id: 0
Start Chirp for Cfg: 0
End Chirp for Cfg: 0
Frequency Slope Var (MHz/μs): 0.000
Idle Time Var (μs): 0.00
ADC Start Var (μs): 0.00

Frame

Start Chirp TX: 0
End Chirp TX: 0
No of Frames: 180
No of Chirp Loops: 200
Periodicity (ms): 14.200000
Trigger Delay (μs): 0.00

Figure 6.6 : Sensor configuration in the mmWaveStudio.

configuration tab. To obtain a high transmitted bandwidth, the chirp rate is set to 60.012 MHz/μs and the chirp duration is set to 60 μs. In the AWR1843 radar sensor, the transmitted signals are packaged in a series of frames and each of them includes a sequence of chirps to be transmitted subsequently. Since the AWR1843 radar sensor is not capable of generating the triangular frequency modulated waveform and its ADC does not work whenever the beat signal is at high frequencies, the one-dimensional beat signal is obtained by concatenating the received samples in all chirp periods and padding zeros during ADC idle time. Therefore, appropriate chirp and frame parameters are set up to obtain a high duty-cycle in the system as seen in Fig. 6.6, and the trigger frame button is clicked to launch the transmission.

6.4 Positioning Control Subsystem

A linear motion machine made by FUYU Technology company with a length of 1.5 m is adopted to build a moving platform. The stepping motor is triggered

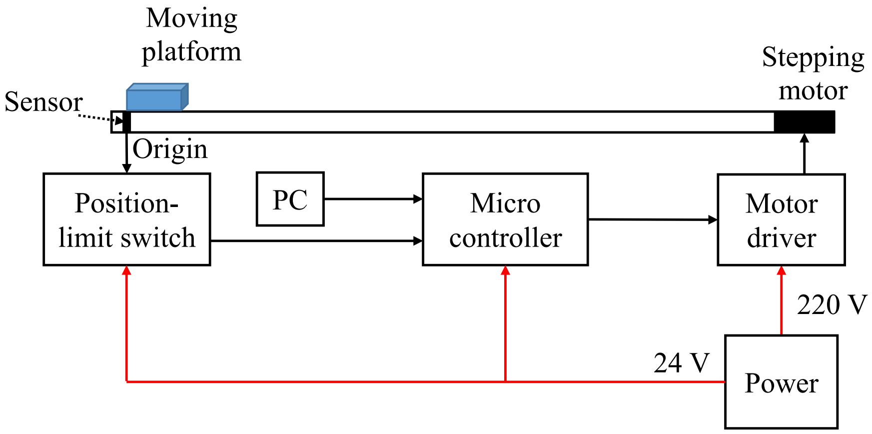

Figure 6.7 : Construction of moving platform.

by its driver and this driver is connected to a micro controller. For simplicity, this company provides a GUI to conduct the movement in a PC, sending the command signal to the micro controller via a USB cable.

The construction of the moving platform is described in Fig. 6.7, where the red and black solid lines denote the power and signaling connections respectively. According to the user's manuals, the moving platform can be installed as follows. A position-limit switch is used to set up the origin. Once the platform reach the origin, a trigger signal can be sent to the micro controller. The outputs of this switch and the PC are connected to the micro controller. After the installation, the moving platform system is powered up and the GUI is launched in the PC. The parameters of stepping motor is set up and the moving process can be conducted by a program which is written, complied and stored into the micro controller. Once clicking the trigger button, the platform can be launched.

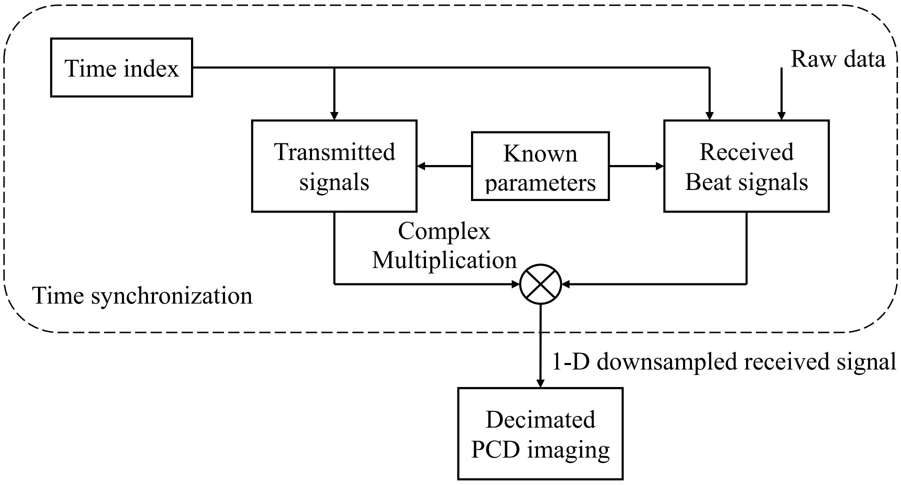

Figure 6.8 : Digital imaging process.

6.5 Digital Imaging Subsystem

After triggering the radar transmission and the stepping motor of the moving platform simultaneously, the received 1-D complex beat samples can be directly transferred to the PC and stored as a binary file. The Matlab 2018 is adopted to read this binary file and implement the decimated PCD algorithm. The flowchart of the digital imaging process is described in Fig. 6.8.

Before the decimated PCD processing, the time synchronization between the received and reference signal should be achieved accurately. Firstly, a time index is obtained from the 1-D data matrix and then the transmitted signal and the received beat signal can be constructed based on the know radar parameters after padding zeros during ADC idle time. Thus, the 1-D downsampled complex received signal can be recovered from (5.9) and a GCW-SAR image can be finally reconstructed. Note that the first small part of the data received during the acceleration of the moving platform must be removed.

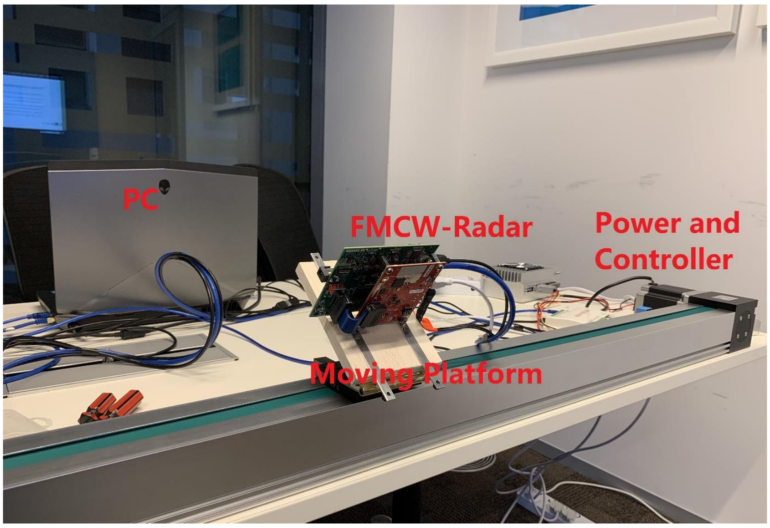

Figure 6.9 : GCW-SAR laboratory system set up.

6.6 Experiment Results

This section describes the real GCW-SAR imaging experiment of the multiple targets in an indoor scenario. Fig. 6.9 shows the GCW-SAR experimental system setup from which the final imaging results are obtained to validate the GCW-SAR concept and demonstrate the performance of the proposed GCW-SAR implementation.

6.6.1 Geometry of the GCW-SAR Experiment

A stripmap GCW-SAR geometry, as shown in Fig. 3.1, is adopted in this experiment. The AWR1843 radar sensor is mounted on the moving platform and its radiation pattern points to the observed targets with an incident angle $\theta = 40$ degree. The height of the radar is set to 0.92 m. The maximum accelerated speed of the platform, 20 m/s^2, is used to reach the constant speed v=0.8 m/s. In the experiment, the one-dimensional raw data are obtained by using one-channel working mode with chirp signal bandwidth 3.6 GHz to maximize the range resolution, where the chirp rate and chirp duration are 60.012 MHz/μs and 60 μs respectively. The

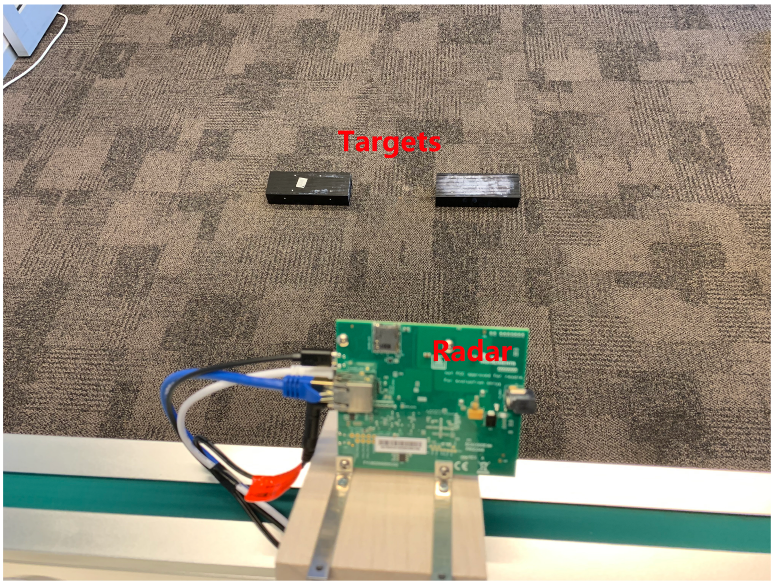

Figure 6.10 : Radar front view during measurement.

idle time between two adjacent chirps and between two adjacent frames are set to 10 μs and 200 μs respectively, reaching a 70.42% duty-cycle. After setting up the radar and positioning parameters, the moving platform and the FMCW radar are triggered when the PC sends command strings to them. Two targets of rectangular metal blocks are measured with dimension 0.225 m × 0.08 m. Fig. 6.10 shows the radar front view during the measurements, where the length in azimuth of the target is 0.225 m.

6.6.2 Imaging Results

A combination of the deramp-on-receive technique and the decimated PCD imaging algorithm is adopted in this experiment. After recovering the downsampled 1-D complex received signal, the final image can be reconstructed by using the decimated PCD imaging. Without deramp-on-received, the sampling rate would be larger than 3.6 GHz to satisfy the Nyquist–Shannon sampling theorem. After the deramping, the sampling rate is reduced to 10 MHz and thus the azimuth spacing is extended by 360 times, saving much computational cost. By using the decimated PCD, a lower sampling rate can be achieved and a larger azimuth spacing can further reduce the complexity. In this subsection, the real GCW-SAR imaging results are presented.

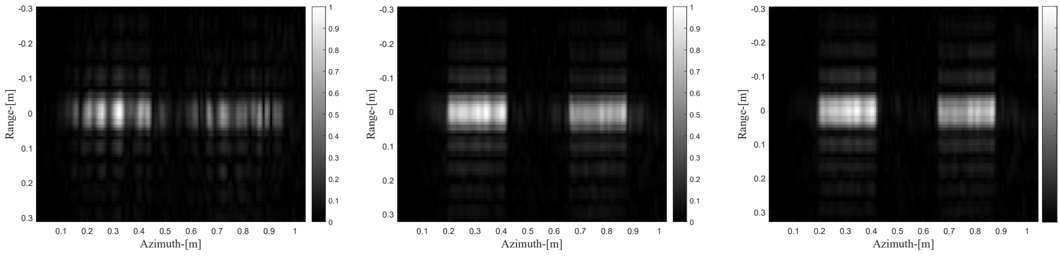

(a) (b) (c)

Figure 6.11 : Real data GCW-SAR imaging comparison with different Q: (a) Q= 0.5617, (b) Q= 3.5106, and (c) Q= 14.0425.

By using the AWR1843 radar sensor, the ratio $L/L_a = 7.1212$ is fixed in the experimental scenario and thus the PCD image quality Q is only determined by the parameter P. Based on the proposed GCW-SAR parameter design in section 4.4, to obtain the upper bound of the normalized PCD imaging error $\epsilon^2 = 0.1$, the image quality factor Q is approximately equal to 3.6 and thus P is set to 5. For comparison, the GCW-SAR images with different Q values = 0.5617, 3.5106, and 14.0425, corresponding to P= 2, 5, and 10 respectively, are reconstructed by using the decimated PCD algorithm with the same $\Delta x = 0.004$ m, as shown in Fig. 6.11. It is evident that the two targets are shown clearly in the GCW-SAR image with the $Q = 3.5106$. When Q is increased to 14.0425, the improvement of the image quality in azimuth can be hardly seen, and a small Q can lead to a worse PCD imaging performance. Therefore, $P = 5$ is suitable for this real imaging system.

With the known $P = 5$ and $L/L_a = 7.1212$, the number of constant segments K in the decimated PCD algorithm can be selected based on (4.25). Fig. 6.12 shows the relationship between K and ϵ^2. To keep $\epsilon^2 \leq 0.2$, K is set to 10. The real data GCW-SAR images reconstructed by using different $K = 2$, 5, and 10 are

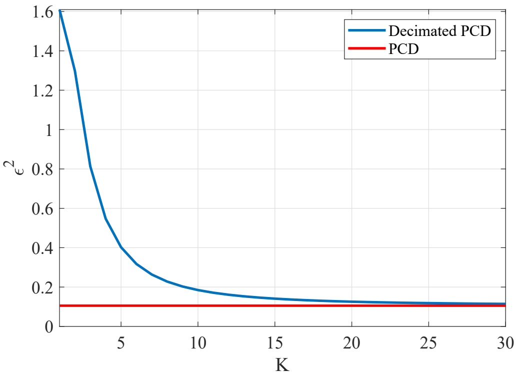

Figure 6.12 : Decimated PCD error function with different K, where $P = 5$ and $L/L_a = 7.1212$.

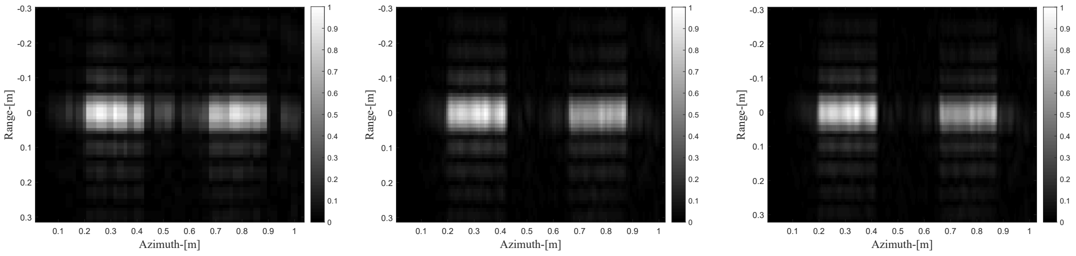

(a) (b) (c)

Figure 6.13 : Real data GCW-SAR imaging comparison with the same $P = 5$ and $L/L_a = 7.1212$ but different K: (a) $K = 2$ ($\Delta x = 0.02$ m), (b) $K = 5$ ($\Delta x = 0.008$ m), and (c) $K = 10$ ($\Delta x = 0.004$ m).

shown respectively with the same $P = 5$ and $L/L_a = 7.1212$ in Fig. 6.13. The two targets can be seen clearly even when $K = 5$ where the corresponding $\epsilon^2 = 0.4$ since the radar cross section of the targets is much higher than that of the carpet floor. Therefore, the threshold of ϵ^2 is determined based on the different imaging scenarios.

In addition, the computational cost can be further reduced by downsampling the received signal. In the above experimental results, N_{s1} is set to 1, and thus the sampling rate of the downsampled received signal is 10 MHz. With the known $P = 5$, $L/L_a = 7.1212$, and $K = 10$, the real data GCW-SAR image with $N_{s1} = 2$ is reconstructed as shown in Fig. 6.14. With reduced SNR, the two targets cannot be distinguished and thus N_{s1} should be set to 1 in this GCW-SAR experimental scenario.

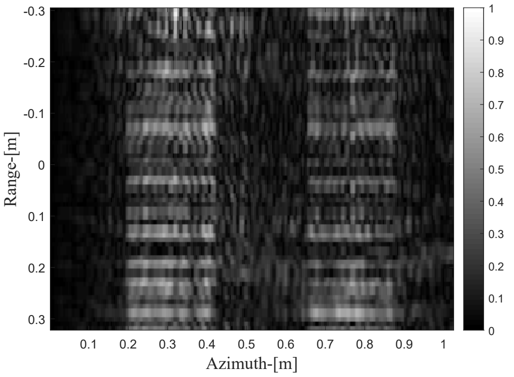

Figure 6.14 : Real data GCW-SAR image with $N_{s1} = 2$.

Therefore, to design a practical GCW-SAR system, the antenna aperture L_a and the transmitted signal bandwidth should be firstly determined to ensure the azimuth and range resolutions. Then, the synthetic aperture L is obtained based on the carrier frequency and the imaging distance. With the known L/L_a ratio and the desired normalized PCD error ϵ^2, the number of linear segments P can be determined. Substituting P and L/L_a into (4.25), the number of constant segments K can be further determined. Finally, N_{s1} can be selected based on the required SNR.

6.7 Summary

A real millimeter wave GCW-SAR experimental system with deramp-on-receive is presented in this chapter. By using the AWR 1843 radar sensor made by TI and a linear moving platform made by FUYU Technology company, a stripmap single channel GCW-SAR system, consisting of receiver frontend subsystem, radar control subsystem, positioning control subsystem and the digital imaging subsystem, is achieved and these four subsystems have been described respectively. The experimental results can validate the GCW-SAR concept, performance analysis and the millimeter wave GCW-SAR system proposed in the early chapters. This practical GCW-SAR system also provides a suitable platform to demonstrate more GCW-SAR working modes in our future work. For example, the AWR1843 sensor can acquire multiple channels within 3 transmit and 4 receive antennas, which allows for a MIMO GCW-SAR system. By substituting the circular moving platform to the linear one, a circular GCW-SAR system can be developed. These novel GCW-SAR working modes will be further investigated by this experimental platform.

Chapter 7

Conclusion

The conventional slow time sampling in azimuth leads to some intrinsic limitations to the pulsed and FMCW SAR systems including the rigid time sequences in transmission and reception, the trade-off between the range swath and azimuth resolution, the range cell migration, and the azimuth ambiguities and restrictions in FMCW SAR. The methods to overcome these limitations have become the most challenging topics in SAR related researches. To achieve a high resolution and a wider range swath, the state-of-the-art SAR uses several advanced techniques to develop different SAR working modes, and a large number of corresponding SAR imaging algorithms are proposed to deal with the range cell migration and other phase errors. However, these intrinsic limitations are not removed with existing SAR technologies since they still adopt the compression of the slow time samples to determine the azimuth image.

This thesis develops a novel GCW-SAR system, where the slow time sampling is no longer adopted and the SAR image can be reconstructed by correlating the 1-D received signals with location dependent reference signals after self-interference cancellation. The state-of-art SAR technologies are revisited in Chapter 2, indicating the limitations caused by slow time sampling. Chapter 3 presents the GCW-SAR concept including the SIC technique in GCW-SAR, 1-D CW imaging process and GCW-SAR ambiguity function. To reduce the computational cost, the PCD algorithm is proposed in this chapter based on the linear approximation of the slant range. A faster and more flexible PCD implementation, i.e., decimated PCD algorithm, is further proposed to reduce the PCD complexity. The PCD imaging is the key enabling technology in GCW-SAR and its performance analysis is derived in Chapter 4, offering a clear guideline to the GCW-SAR imaging system design. The difference between conventional SAR and PCD imaging is investigated and then the PCD ambiguity function is derived. An error function of the PCD imaging as compared with the ideal matched filtering is adopted and can be shown as a function of image quality to quantify the PCD imaging performance. Accordingly, the error function of the decimated PCD imaging is analyzed. In Chapter 5, two GCW-SAR systems, i.e., passive GCW-SAR system and millimeter wave GCW-SAR system with deramp-on-receive, are developed. A novel modified PCD imaging is proposed for the passive GCW-SAR system. A millimeter wave GCW-SAR implementation is achieved based on the deramping technique in FMCW signalling, leading to a light-weight and low cost GCW-SAR system. Using the millimeter wave signals also can offer advantages to the GCW-SAR imaging. Chapter 6 describes the construction of the real millimeter wave GCW-SAR experimental system in detailed. The experimental results are shown to validate the proposed GCW-SAR system.

7.1 Future Work

The works presented in this thesis establishes a solid theoretical foundation for next-generation imaging radars. Without the slow time, the transmitted signal and the imaging system designs are more flexible, and thus more effective practical GCW-SAR systems can be developed in the future based on the different system geometry and the multiple received channels. The following research fields will be considered.

- Circular SAR is a new kind of imaging process in a circular trajectory which is capable of achieving a 360-degree aspect angle observation to the target scene. In a conventional linear SAR system, the Doppler spectrum bandwidth can be only improved by extending the synthetic aperture to increase the observed angle. In contrast, the observed angle in a circular trajectory varies from zero to 360 degrees, thus achieving a higher resolution. Therefore, a circular GCW-SAR can be developed. Since the targets with the same distance from the origin have the same variation of the instantaneous slant range, a polar coordinate is more suitable for the PCD imaging. The effect of the PCD imaging on a circular GCW-SAR will be investigated and a modified PCD algorithm will be proposed. The implementation and real-data experiment are also required in the future work.

- In a microwave imaging system, an image can be reconstructed from the data recorded over a 2-D aperture. This multiple-channel data acquisition can be achieved by a linear mechanic scanning of an antenna array. The conventional imaging algorithms are conducted in a two-dimensional domain similar to the range Doppler algorithm in SAR system. Adopting a wideband transmitted signal, the radar can look down the observed scene on both sides and a 3-D image can be reconstructed. This technique can be also used in a GCW-SAR system. With a 2-D synthetic aperture, the variation of the instantaneous slant range can be presented as a hyperbolic surface. Therefore, different linear approximation of the slant range has to be considered and a new microwave imaging system will be developed.

Appendix A

Derivation of PCD azimuth ambiguity function

Defining the rectangular function $rect(\frac{t}{T})$ as

$$rect(\frac{t}{T}) = \begin{cases} 1, & |t| < T/2, \\ \frac{1}{2}, & |t| = T/2, \\ 0, & \text{otherwise} \end{cases} \tag{A.1}$$

the PCD image $I_1(x_m, 0)$ in (4.14) can be described as

$$\begin{aligned} & I_1(x_m, 0) \\ & = \sigma(0,0)e^{-j\frac{2\pi x_m^2}{\lambda R_c}} \int_{-\infty}^{\infty} \frac{1}{T} rect(\frac{t}{T}) e^{j\frac{4\pi}{\lambda}d_1(t,0,0)} e^{-j2\pi\frac{2vx_m}{\lambda R_c}t} dt \end{aligned} \tag{A.2}$$

which can be viewed as a Fourier transform, in terms of a frequency variable $\Omega = \frac{2vx_m}{\lambda R_c}$. The time domain function, which is a product of $\frac{1}{T}rect(\frac{t}{T})$ and $e^{j\frac{4\pi}{\lambda}d_1(t,0,0)}$, can be represented as a convolution in Ω domain, so that Eq. (A.2) can be rewritten as

$$\begin{aligned} & I_1(x_m, 0) \\ & = \sigma(0,0)e^{-j\frac{2\pi x_m^2}{\lambda R_c}} \Big(\int_{-\infty}^{\infty} \frac{1}{T} rect(\frac{t}{T}) e^{-j2\pi\Omega t} dt \otimes \int_{-\infty}^{\infty} e^{j\frac{4\pi}{\lambda}d_1(t,0,0)} e^{-j2\pi\Omega t} dt \Big) \end{aligned} \tag{A.3}$$

where $\otimes$ denotes convolution operation. The expression of $\frac{1}{T}rect(t)$ in Ω domain is the sinc function $sinc(T\Omega)$. Since $d_1(t, x_m, y_n)$ is a periodic function, the Fourier transform of $e^{j\frac{4\pi}{\lambda}d_1(t,0,0)}$ can be expressed as

$$\int_{-\infty}^{\infty} e^{j\frac{4\pi}{\lambda}d_1(t,0,0)} e^{-j2\pi\Omega t} dt = \frac{1}{T_P} \sum_{i=-\infty}^{\infty} D(\frac{i}{T_P}) \delta(\Omega - \frac{i}{T_P}) \tag{A.4}$$

where $D(\Omega)$ is the Fourier transform of $e^{j\frac{4\pi}{\lambda}d_1(t,0,0)}$ in one period, i.e.,

$$D(\Omega) = \int_{-\frac{T_P}{2}}^{\frac{T_P}{2}} e^{j\frac{4\pi}{\lambda}d_1(t,0,0)} e^{-j2\pi\Omega t} dt. \tag{A.5}$$

Therefore, $I_1(x_m, 0)$ can be expressed as

$$\begin{aligned}
&I_1(x_m, 0) \\
&= \sigma(0,0)e^{-j\frac{2\pi x_m^2}{\lambda R_c}}\Big(sinc(T\Omega) \otimes \frac{1}{T_P}\sum_{i=-\infty}^{\infty} D(\frac{i}{T_P})\delta(\Omega - \frac{i}{T_P})\Big) \\
&= \sigma(0,0)e^{-j\frac{2\pi x_m^2}{\lambda R_c}}\Big(\frac{1}{T_P}\sum_{i=-\infty}^{\infty} D(\frac{i}{T_P})sinc(T(\Omega - \frac{i}{T_P}))\Big).
\end{aligned} \tag{A.6}$$

Defining $W(x) = \frac{1}{T_P}D(\frac{2vx}{\lambda R_c})$ and replacing Ω by $\frac{2vx}{\lambda R_c}$, we have the final expression of (4.14).

Appendix B

PCD Weight Function

Assuming that the number of linear segments, P, is odd, $d_1(t,0,0)$ in the integration interval $[-\frac{T_P}{2},\frac{T_P}{2})$ can be expressed as

$$d_1(t,0,0) = \frac{v^2}{2R_c}(-t^2+\frac{T_P^2}{4}), t \in [-\frac{T_P}{2},\frac{T_P}{2}). \tag{B.1}$$

Hence, the corresponding weight function can be derived as

$$\begin{aligned}
W(x) &= \frac{1}{T_P}\int_{-\frac{T_P}{2}}^{\frac{T_P}{2}} e^{j\frac{4\pi}{\lambda}d_1(t,0,0)} e^{-j2\pi\frac{2vx}{\lambda R_c}t}dt \\
&= \frac{1}{T_P}\int_{-\frac{T_P}{2}}^{\frac{T_P}{2}} e^{j\frac{4\pi}{\lambda}\frac{v^2}{2R_c}(-t^2+\frac{T_P^2}{4})} e^{-j2\pi\frac{2vx}{\lambda R_c}t}dt \\
&= e^{j\frac{\pi v^2T_P^2}{2\lambda R_c}}\frac{1}{T_P}\int_{-\frac{T_P}{2}}^{\frac{T_P}{2}} e^{-j\frac{2\pi}{\lambda R_c}(v^2t^2+2xvt)}dt \\
&= e^{j\frac{\pi v^2T_P^2}{2\lambda R_c}} e^{j\frac{2\pi x^2}{\lambda R_c}}\frac{1}{T_P}\int_{-\frac{T_P}{2}}^{\frac{T_P}{2}} e^{-j\frac{2\pi}{\lambda R_c}(vt+x)^2}dt \\
&= \sqrt{\frac{\lambda R_c}{2\pi v^2T_P^2}} e^{j\frac{\pi v^2T_P^2}{2\lambda R_c}} e^{j\frac{2\pi x^2}{\lambda R_c}} \int_{(x-\frac{T_P}{2}v)\sqrt{\frac{2\pi}{\lambda R_c}}}^{(x+\frac{T_P}{2}v)\sqrt{\frac{2\pi}{\lambda R_c}}} e^{-jt^2}dt \\
&= \sqrt{\frac{\lambda R_c}{2\pi v^2T_P^2}} e^{j\frac{\pi v^2T_P^2}{2\lambda R_c}} e^{j\frac{2\pi x^2}{\lambda R_c}} \Big(\int_0^{(x+\frac{T_P}{2}v)\sqrt{\frac{2\pi}{\lambda R_c}}} (cos(t^2) \\
&- jsin(t^2))dt - \int_0^{(x-\frac{T_P}{2}v)\sqrt{\frac{2\pi}{\lambda R_c}}} (cos(t^2) - jsin(t^2))dt \Big) \\
&= \sqrt{\frac{\lambda R_c}{2\pi v^2T_P^2}} e^{j\frac{\pi v^2T_P^2}{2\lambda R_c}} e^{j\frac{2\pi x^2}{\lambda R_c}} \Big(C((x+\frac{T_P}{2}v)\sqrt{\frac{2\pi}{\lambda R_c}}) \\
&- C((x-\frac{T_P}{2}v)\sqrt{\frac{2\pi}{\lambda R_c}}) + jS((x-\frac{T_P}{2}v)\sqrt{\frac{2\pi}{\lambda R_c}}) \\
&- jS((x+\frac{T_P}{2}v)\sqrt{\frac{2\pi}{\lambda R_c}}) \Big)
\end{aligned} \tag{B.2}$$

where $S(x)$ and $C(x)$ are the Fresnel integrals respectively defined as

$$\begin{aligned} S(x) &= \int_0^x sin(t^2)dt = \sum_{n=0}^{\infty}(-1)^n \frac{x^{4n+3}}{(2n+1)!(4n+3)}, \\ C(x) &= \int_0^x cos(t^2)dt = \sum_{n=0}^{\infty}(-1)^n \frac{x^{4n+1}}{(2n)!(4n+1)}. \end{aligned} \tag{B.3}$$

Since $L \approx \frac{\lambda}{L_a} R_c$, Eq. (B.2) is further expressed as (4.15).

When P is even, $d_1(t, 0, 0)$ is a time $\frac{T_P}{2}$ shifted version of that with odd P, so that $W(x)$ has the same expression as (B.2) except for a phase shift $e^{-j\frac{2\pi v T_P}{\lambda R_c}x}$. Note that both weight functions have the same amplitude $|W(x)|$ and $W(0)$.

Appendix C

Integral in Decimated PCD Error Function

Based on (4.23), the integral $\frac{1}{T}\int_{-\frac{T}{2}}^{\frac{T}{2}} e^{j\frac{4\pi}{\lambda}\hat{d}_1(t,0,0)}dt$ can be expressed as a sum of $P \cdot K$ integrations over respective constant segments of the slant range, i.e.,

$$\begin{aligned}
&\frac{1}{T}\int_{-\frac{T}{2}}^{\frac{T}{2}} e^{j\frac{4\pi}{\lambda}\hat{d}_1(t,0,0)}dt \\
&= \frac{1}{T}\sum_{p=0}^{P-1}\sum_{k=0}^{K-1}\int_{t_p+k\frac{\Delta x}{v}}^{t_p+(k+1)\frac{\Delta x}{v}} e^{j\frac{4\pi}{\lambda}\frac{v^2(t_{p+1}+t_p)}{2R_c}k\frac{\Delta x}{v}+\frac{v^2}{2R_c}(t_p^2-t^2)}dt \\
&= \frac{1}{T}\sum_{p=0}^{P-1}\sum_{k=0}^{K-1}\int_{t_p+k\frac{\Delta x}{v}}^{t_p+(k+1)\frac{\Delta x}{v}} e^{j\frac{2\pi v^2}{\lambda R_c}(-t^2+(t_{p+1}+t_p)k\frac{\Delta x}{v}+t_p^2)}dt \\
&= \frac{1}{P}\sum_{p=0}^{P-1}\sum_{k=0}^{K-1} e^{j\frac{2\pi v^2}{\lambda R_c}((t_{p+1}+t_p)k\frac{\Delta x}{v}+t_p^2)}\sqrt{\frac{\lambda R_c}{2\pi v^2 T_P^2}}\int_{(t_p+k\frac{\Delta x}{v})\sqrt{\frac{2\pi v^2}{\lambda R_c}}}^{(t_p+(k+1)\frac{\Delta x}{v})\sqrt{\frac{2\pi v^2}{\lambda R_c}}} e^{-jt^2}dt.
\end{aligned} \tag{C.1}$$

Since $t_p = -\frac{T}{2} + pT_P$, $L \approx \frac{\lambda}{L_a}R_c$, and $\Delta x = \frac{T_P}{K}v$, Eq. (C.1) can be further derived as

$$\begin{aligned}
&\frac{1}{T}\int_{-\frac{T}{2}}^{\frac{T}{2}} e^{j\frac{4\pi}{\lambda}\hat{d}_1(t,0,0)}dt \\
&= \frac{1}{P}\sum_{p=0}^{P-1}\sum_{k=0}^{K-1} e^{j\frac{2\pi}{P^2}\frac{L}{L_a}((-P+2p+1)\frac{k}{K}+(-\frac{P}{2}+p)^2)}\sqrt{\frac{P^2}{2\pi}\frac{L_a}{L}}\int_{(-\frac{P}{2}+p+\frac{k}{K})\sqrt{\frac{2\pi}{P^2}\frac{L}{L_a}}}^{(-\frac{P}{2}+p+\frac{k+1}{K})\sqrt{\frac{2\pi}{Q}}} e^{-jt^2}dt \\
&= \frac{1}{P}\sum_{p=0}^{P-1}\sum_{k=0}^{K-1} e^{j\frac{2\pi}{P^2}\frac{L}{L_a}((-P+2p+1)\frac{k}{K}+(-\frac{P}{2}+p)^2)}\sqrt{\frac{P^2}{2\pi}\frac{L_a}{L}}\Big(C((-\frac{P}{2}+p+\frac{k+1}{K})\sqrt{\frac{2\pi}{P^2}\frac{L}{L_a}}) \\
&- C((-\frac{P}{2}+p+\frac{k}{K})\sqrt{\frac{2\pi}{P^2}\frac{L}{L_a}}) + jS((-\frac{P}{2}+p+\frac{k}{K})\sqrt{\frac{2\pi}{P^2}\frac{L}{L_a}}) \\
&- jS((-\frac{P}{2}+p+\frac{k+1}{K})\sqrt{\frac{2\pi}{P^2}\frac{L}{L_a}})\Big).
\end{aligned} \tag{C.2}$$

Bibliography

[1] A. Moreira, P. Prats-Iraola, M. Younis, G. Krieger, I. Hajnsek, and K. P. Papathanassiou, “A Tutorial on Synthetic Aperture Radar,” *IEEE Geoscience and Remote Sensing Magazine*, vol. 1, no. 1, pp. 6–43, March 2013.

[2] J. H. Gonzalez, M. Bachmann, R. Scheiber, and G. Krieger, “Definition of ICESat Selection Criteria for Their Use as Height References for TanDEM-X,” *IEEE Transactions on Geoscience and Remote Sensing*, vol. 48, no. 6, pp. 2750–2757, June 2010.

[3] A. Rosenqvist, M. Shimada, N. Ito, and M. Watanabe, “Alos Palsar: A Pathfinder Mission for Global-Scale Monitoring of The Environment,” *IEEE Transactions on Geoscience and Remote Sensing*, vol. 45, no. 11, pp. 3307–3316, Nov 2007.

[4] C. Clemente and J. J. Soraghan, “Vibrating Target Micro-Doppler Signature in Bistatic SAR with A Fixed Receiver,” *IEEE Transactions on Geoscience and Remote Sensing*, vol. 50, no. 8, pp. 3219–3227, Aug 2012.

[5] X. M. Li, S. Lehner, and T. Bruns, “Ocean Wave Integral Parameter Measurements Using Envisat ASAR Wave Mode Data,” *IEEE Transactions on Geoscience and Remote Sensing*, vol. 49, no. 1, pp. 155–174, Jan 2011.

[6] J. P. Robin, M. Lafitte, and E. Coiras, “A Review of SAR Imagery Exploitation Methods in Support of Defence and Security Missions,” in *Proceedings of EUSAR 2016: 11th European Conference on Synthetic Aperture Radar*, June 2016, pp. 1–5.

[7] I. G. Cumming and F. H. Wong, *Digital Processing of Synthetic Aperture Radar Data*, 2005, vol. 1, no. 2.

[8] M. Soumekh, *Synthetic Aperture Radar Signal Processing.* New York: Wiley, 1999, vol. 7.

[9] M. I. Skolnik, "Introduction to Radar Systems," *New York, McGraw Hill Book Co., 1980. 590 p.*, 1980.

[10] I. Cumming and J. Bennett, "Digital Processing of SEASAT SAR Data," in *ICASSP'79. IEEE International Conference on Acoustics, Speech, and Signal Processing*, vol. 4. IEEE, 1979, pp. 710–718.

[11] N. Ducet, P.-Y. Le Traon, and G. Reverdin, "Global High-Resolution Mapping of Ocean Circulation from TOPEX/Poseidon and ERS-1 and-2," *Journal of Geophysical Research: Oceans*, vol. 105, no. C8, pp. 19 477–19 498, 2000.

[12] M. C. Dobson, L. E. Pierce, and F. T. Ulaby, "Knowledge-Based Land-Cover Classification Using ERS-1/JERS-1 SAR Composites," *IEEE Transactions on Geoscience and Remote Sensing*, vol. 34, no. 1, pp. 83–99, 1996.

[13] J. Horstmann, W. Koch, S. Lehner, and R. Tonboe, "Ocean Winds from RADARSAT-1 ScanSAR," *Canadian journal of remote sensing*, vol. 28, no. 3, pp. 524–533, 2002.

[14] F. De Zan and A. Monti Guarnieri, "TOPSAR: Terrain Observation by Progressive Scans," *IEEE Transactions on Geoscience and Remote Sensing*, vol. 44, no. 9, pp. 2352–2360, Sep. 2006.

[15] R. Bamler and M. Eineder, "Scansar Processing Using Standard High Precision SAR Algorithms," *IEEE Transactions on Geoscience and Remote Sensing*, vol. 34, no. 1, pp. 212–218, Jan 1996.

[16] J. Mittermayer, A. Moreira, and O. Loffeld, “Spotlight SAR Data Processing Using The Frequency Scaling Algorithm,” *IEEE Transactions on Geoscience and Remote Sensing*, vol. 37, no. 5, pp. 2198–2214, Sep. 1999.

[17] M. D. Desai and W. K. Jenkins, “Convolution Backprojection Image Reconstruction for Spotlight Mode Synthetic Aperture Radar,” *IEEE Transactions on Image Processing*, vol. 1, no. 4, pp. 505–517, Oct 1992.

[18] J. H. Kim, M. Younis, A. Moreira, and W. Wiesbeck, “A Novel Ofdm Chirp Waveform Scheme for Use of Multiple Transmitters in SAR,” *IEEE Geoscience and Remote Sensing Letters*, vol. 10, no. 3, pp. 568–572, May 2013.

[19] J. Wang, X. D. Liang, L. Y. Chen, and K. Li, “A Novel Space-Time Coding Scheme Used for MIMO-SAR Systems,” *IEEE Geoscience and Remote Sensing Letters*, vol. 12, no. 7, pp. 1556–1560, July 2015.

[20] W. Q. Wang, “Space-Time Coding MIMO-OFDM SAR for High-Resolution Imaging,” *IEEE Transactions on Geoscience and Remote Sensing*, vol. 49, no. 8, pp. 3094–3104, Aug 2011.

[21] G. Krieger, N. Gebert, and A. Moreira, “Multidimensional Waveform Encoding: A New Digital Beamforming Technique for Synthetic Aperture Radar Remote Sensing,” *IEEE Transactions on Geoscience and Remote Sensing*, vol. 46, no. 1, pp. 31–46, Jan 2008.

[22] G. Krieger, “MIMO-SAR: Opportunities and Pitfalls,” *IEEE Transactions on Geoscience and Remote Sensing*, vol. 52, no. 5, pp. 2628–2645, May 2014.

[23] N. Gebert, G. Krieger, and A. Moreira, “Digital Beamforming on Receive: Techniques and Optimization Strategies for High-Resolution Wide-Swath SAR Imaging,” *IEEE Transactions on Aerospace and Electronic Systems*, vol. 45, no. 2, pp. 564–592, April 2009.

[24] A. Currie and M. A. Brown, “Wide-Swath SAR,” *IEE Proceedings F - Radar and Signal Processing*, vol. 139, no. 2, pp. 122–135, April 1992.

[25] J. C. Curlander and R. N. McDonough, “Synthetic Aperture Radar Systems and Signal Processing,” *New York: John Wiley & Sons, Inc, 1991.*, 1991.

[26] Y. Liu, Y. K. Deng, and R. Wang, “Focus Squint FMCW SAR Data Using Inverse Chirp-Z Transform Based on an Analytical Point Target Reference Spectrum,” *IEEE Geoscience and Remote Sensing Letters*, vol. 9, no. 5, pp. 866–870, Sept 2012.

[27] Z. Jiang, F. Huang, J. Wan, and Z. Cheng, “Modified Frequency Scaling Algorithm for FMCW SAR Data Processing,” *Chinese Journal of Aeronautics*, vol. 20, no. 4, pp. 339–345, 2007.

[28] R. Wang, O. Loffeld, H. Nies, S. Knedlik, M. Hagelen, and H. Essen, “Focus FMCW SAR Data Using The Wavenumber Domain Algorithm,” *IEEE Transactions on Geoscience and Remote Sensing*, vol. 48, no. 4, pp. 2109–2118, April 2010.

[29] R. J. Mailloux, *Phased Array Antenna Handbook.* Artech house, 2017.

[30] A. G. Stove, “Linear FMCW Radar Techniques,” in *IEE Proceedings F (Radar and Signal Processing)*, vol. 139, no. 5. IET, 1992, pp. 343–350.

[31] D. Zhu, “A Novel Approach to Residual Video Phase Removal in Spotlight SAR Image Formation,” in *2007 IET International Conference on Radar Systems*, Oct 2007, pp. 1–4.

[32] G. T. Ruck, D. E. Barrick, W. D. Stuart, and C. K. Krichbaum, *Radar Cross Section Handbook.* Plenum press New York, 1970, vol. 1.

[33] R. Lanari, S. Hensley, and P. Rosen, “Modified SPECAN Algorithm for ScanSAR Data Processing,” in *IGARSS ’98. Sensing and Managing The Environment. 1998 IEEE International Geoscience and Remote Sensing. Symposium Proceedings. (Cat. No.98CH36174)*, vol. 2, July 1998, pp. 636–638 vol.2.

[34] L. Fang, X. Wang, and Y. Wang, “A Modified SPECAN Algorithm for Synthetic Aperture Radar Imaging,” in *2010 International Conference on Measuring Technology and Mechatronics Automation*, vol. 1, March 2010, pp. 153–156.

[35] Zengliang Li, Di Yao, and Teng Long, “SPECAN Algorithm for Forward-Looking Bistatic SAR,” in *2008 9th International Conference on Signal Processing*, Oct 2008, pp. 2517–2520.

[36] F. Li, C. Croft, and D. N. Held, “Comparison of Several Techniques to Obtain Multiple-Look SAR Imagery,” *IEEE Transactions on Geoscience and Remote Sensing*, vol. GE-21, no. 3, pp. 370–375, July 1983.

[37] N. Li, S. Niu, Z. Guo, Y. Liu, and J. Chen, “Raw Data-Based Motion Compensation for High-Resolution Sliding Spotlight Synthetic Aperture Radar,” *Sensors*, vol. 18, no. 3, p. 842, 2018.

[38] R. Bamler, “A Comparison of Range-Doppler and Wavenumber Domain SAR Focusing Algorithms,” *IEEE Transactions on Geoscience and Remote Sensing*, vol. 30, no. 4, pp. 706–713, 1992.

[39] C. Cafforio, C. Prati, and F. Rocca, “SAR Data Focusing Using Seismic Migration Techniques,” *IEEE Transactions on Aerospace and Electronic Systems*, vol. 27, no. 2, pp. 194–207, March 1991.

[40] A. Li, “Algorithms for The Implementation of Stolt Interpolation in SAR Processing,” in *IGARSS’92; Proceedings of the 12th Annual International Geoscience and Remote Sensing Symposium*, vol. 1, 1992, pp. 360–362.

[41] E. Fishler, A. Haimovich, R. Blum, D. Chizhik, L. Cimini, and R. Valenzuela, “MIMO Radar: An Idea Whose Time Has Come,” in *Proceedings of the 2004 IEEE Radar Conference (IEEE Cat. No.04CH37509)*, April 2004, pp. 71–78.

[42] J. Li and P. Stoica, “MIMO Radar with Colocated Antennas,” *IEEE Signal Processing Magazine*, vol. 24, no. 5, pp. 106–114, Sep. 2007.

[43] M. Suess, B. Grafmueller, and R. Zahn, “A Novel High Resolution, Wide Swath SAR System,” in *IGARSS 2001. Scanning the Present and Resolving the Future. Proceedings. IEEE 2001 International Geoscience and Remote Sensing Symposium (Cat. No.01CH37217)*, vol. 3, July 2001, pp. 1013–1015 vol.3.

[44] G. Krieger, N. Gebert, and A. Moreira, “Unambiguous SAR Signal Reconstruction from Nonuniform Displaced Phase Center Sampling,” *IEEE Geoscience and Remote Sensing Letters*, vol. 1, no. 4, pp. 260–264, Oct 2004.

[45] A. Bellettini and M. A. Pinto, “Theoretical Accuracy of Synthetic Aperture Sonar Micronavigation Using A Displaced Phase-Center Antenna,” *IEEE Journal of Oceanic Engineering*, vol. 27, no. 4, pp. 780–789, Oct 2002.

[46] M. Suess and W. Wiesbeck, “Side Looking SAR System,” Mar. 22 2005, uS Patent 6,870,500.

[47] S. Zhu, G. Liao, Y. Qu, Z. Zhou, and X. Liu, “Ground Moving Targets Imaging Algorithm for Synthetic Aperture Radar,” *IEEE Transactions on Geoscience and Remote Sensing*, vol. 49, no. 1, pp. 462–477, Jan 2011.

[48] D. Cerutti-Maori and I. Sikaneta, “A Generalization of DPCA Processing for Multichannel SAR/GMTI Radars,” *IEEE Transactions on Geoscience and Remote Sensing*, vol. 51, no. 1, pp. 560–572, Jan 2013.

[49] D. Cerutti-Maori, I. Sikaneta, and C. H. Gierull, “Optimum SAR/GMTI Processing and Its Application to The Radar Satellite RADARSAT-2 for Traffic

Monitoring," *IEEE Transactions on Geoscience and Remote Sensing*, vol. 50, no. 10, pp. 3868–3881, Oct 2012.

[50] A. Ferretti, C. Prati, and F. Rocca, "Permanent Scatterers in SAR Interferometry," *IEEE Transactions on Geoscience and Remote Sensing*, vol. 39, no. 1, pp. 8–20, Jan 2001.

[51] G. Krieger, A. Moreira, H. Fiedler, I. Hajnsek, M. Werner, M. Younis, and M. Zink, "TanDEM-X: A Satellite Formation for High-Resolution SAR Interferometry," *IEEE Transactions on Geoscience and Remote Sensing*, vol. 45, no. 11, pp. 3317–3341, Nov 2007.

[52] S. R. Cloude and K. P. Papathanassiou, "Polarimetric SAR Interferometry," *IEEE Transactions on Geoscience and Remote Sensing*, vol. 36, no. 5, pp. 1551–1565, Sep. 1998.

[53] Jong-Sen Lee, D. L. Schuler, and T. L. Ainsworth, "Polarimetric SAR Data Compensation for Terrain Azimuth Slope Variation," *IEEE Transactions on Geoscience and Remote Sensing*, vol. 38, no. 5, pp. 2153–2163, Sep. 2000.

[54] J. Horstmann, W. Koch, S. Lehner, and R. Tonboe, "Wind Retrieval over The Ocean Using Synthetic Aperture Radar with C-Band HH Polarization," *IEEE Transactions on Geoscience and Remote Sensing*, vol. 38, no. 5, pp. 2122–2131, Sep. 2000.

[55] R. Torres, P. Snoeij, D. Geudtner, D. Bibby, M. Davidson, E. Attema, P. Potin, B. Rommen, N. Floury, M. Brown *et al.*, "GMES Sentinel-1 Mission," *Remote Sensing of Environment*, vol. 120, pp. 9–24, 2012.

[56] W. Wang, "MIMO SAR Chirp Modulation Diversity Waveform Design," *IEEE Geoscience and Remote Sensing Letters*, vol. 11, no. 9, pp. 1644–1648, Sep. 2014.

[57] S. Hong, J. Brand, J. I. Choi, M. Jain, J. Mehlman, S. Katti, and P. Levis, "Applications of Self-Interference Cancellation in 5G and Beyond," *IEEE Communications Magazine*, vol. 52, no. 2, pp. 114–121, February 2014.

[58] A. Sabharwal, P. Schniter, D. Guo, D. W. Bliss, S. Rangarajan, and R. Wichman, "In-Band Full-Duplex Wireless: Challenges and Opportunities," *IEEE Journal on Selected Areas in Communications*, vol. 32, no. 9, pp. 1637–1652, Sept 2014.

[59] X. Huang and Y. J. Guo, "Radio Frequency Self-Interference Cancellation With Analog Least Mean-Square Loop," *IEEE Transactions on Microwave Theory and Techniques*, vol. PP, no. 99, pp. 1–15, 2017.

[60] J. Zhou, T. H. Chuang, T. Dinc, and H. Krishnaswamy, "Integrated Wideband Self-Interference Cancellation in The RF Domain for FDD and Full-Duplex Wireless," *IEEE Journal of Solid-State Circuits*, vol. 50, no. 12, pp. 3015–3031, Dec 2015.

[61] M. P. Chang, C. L. Lee, B. Wu, and P. R. Prucnal, "Adaptive Optical Self-Interference Cancellation Using a Semiconductor Optical Amplifier," *IEEE Photonics Technology Letters*, vol. 27, no. 9, pp. 1018–1021, May 2015.

[62] J. I. Choi, M. Jain, K. Srinivasan, P. Levis, and S. Katti, "Achieving Single Channel, Full Duplex Wireless Communication," in *Proceedings of the sixteenth annual international conference on Mobile computing and networking*. ACM, 2010, pp. 1–12.

[63] M. A. Khojastepour, K. Sundaresan, S. Rangarajan, X. Zhang, and S. Barghi, "The Case for Antenna Cancellation for Scalable Full-Duplex Wireless Communications," in *Proceedings of the 10th ACM Workshop on Hot Topics in Networks*. ACM, 2011, p. 17.

[64] E. Everett, A. Sahai, and A. Sabharwal, “Passive Self-Interference Suppression for Full-Duplex Infrastructure Nodes,” *IEEE Transactions on Wireless Communications*, vol. 13, no. 2, pp. 680–694, 2014.

[65] E. Everett, “Full-Duplex Infrastructure Nodes: Achieving Long Range with Half-Duplex Mobiles,” Ph.D. dissertation, Rice University, 2012.

[66] A. Meta, P. Hoogeboom, and L. P. Ligthart, “Signal Processing for FMCW SAR,” *IEEE Transactions on Geoscience and Remote Sensing*, vol. 45, no. 11, pp. 3519–3532, Nov 2007.

[67] A. Meta, “Signal processing of FMCW Synthetic Aperture Radar Data,” 2006.

[68] A. T. Le, Y. Nan, L. C. Tran, X. Huang, Y. J. Guo, and Y. Vardaxoglou, “Analog least mean square loop for self-interference cancellation in generalized continuous wave sar,” in *2018 IEEE 88th Vehicular Technology Conference (VTC-Fall)*, Aug 2018, pp. 1–5.

[69] Y. Na, Y. Lu, and H. Sun, “A Comparison of Back-Projection and Range Migration Algorithms for Ultra-Wideband SAR Imaging,” in *Fourth IEEE Workshop on Sensor Array and Multichannel Processing, 2006.*, July 2006, pp. 320–324.

[70] A. F. Yegulalp, “Fast Backprojection Algorithm for Synthetic Aperture Radar,” in *Proceedings of the 1999 IEEE Radar Conference. Radar into the Next Millennium (Cat. No.99CH36249)*, 1999, pp. 60–65.

[71] S. Xiao, D. C. Munson, S. Basu, and Y. Bresler, “An N2logN Back-Projection Algorithm for SAR Image Formation,” in *Conference Record of the Thirty-Fourth Asilomar Conference on Signals, Systems and Computers (Cat. No.00CH37154)*, vol. 1, Oct 2000, pp. 3–7 vol.1.

[72] L. M. H. Ulander, H. Hellsten, and G. Stenstrom, “Synthetic-Aperture Radar

Processing Using Fast Factorized Back-Projection," *IEEE Transactions on Aerospace and Electronic Systems*, vol. 39, no. 3, pp. 760–776, July 2003.

[73] Y. F. Shao, R. Wang, Y. K. Deng, Y. Liu, R. Chen, G. Liu, and O. Loffeld, "Fast Backprojection Algorithm for Bistatic SAR Imaging," *IEEE Geoscience and Remote Sensing Letters*, vol. 10, no. 5, pp. 1080–1084, Sept 2013.

[74] J. Boersma, "Computation of Fresnel Integrals," *Mathematics of Computation*, 1960.

[75] D. Gromek, K. Kulpa, and P. Samczyński, "Experimental Results of Passive SAR Imaging Using DVB-T Illuminators of Opportunity," *IEEE Geoscience and Remote Sensing Letters*, vol. 13, no. 8, pp. 1124–1128, Aug 2016.

[76] A. Morello and V. Mignone, "DVB-S2: The Second Generation Standard for Satellite Broad-Band Services," *Proceedings of The IEEE*, vol. 94, no. 1, pp. 210–227, 2006.

[77] R. B. Smith, M. Jordan, B. Steinberger, C. M. Puskas, J. Farrell, G. P. Waite, S. Husen, W.-L. Chang, and R. O'Connell, "Geodynamics of The Yellowstone Hotspot and Mantle Plume: Seismic and GPS Imaging, Kinematics, and Mantle Flow," *Journal of Volcanology and Geothermal Research*, vol. 188, no. 1-3, pp. 26–56, 2009.

[78] M. Antoniou, M. Cherniakov, and C. Hu, "Space-Surface Bistatic SAR Image Formation Algorithms," *IEEE Transactions on Geoscience and Remote Sensing*, vol. 47, no. 6, pp. 1827–1843, June 2009.

[79] K. Kulpa, P. Samczynski, M. Malanowski, L. Maslikowski, and V. Kubica, "The Wse of CLEAN Processing for Passive SAR Image Creation," in *2013 IEEE Radar Conference (RadarCon13)*, April 2013, pp. 1–6.

[80] W. Wang, Z. Liu, X. Song, and X. Ma, “Research of Imaging Method for Spaceborne Mosaic Mode SAR,” in *2012 IEEE 11th International Conference on Signal Processing*, vol. 3, Oct 2012, pp. 1847–1851.

[81] N. Li, R. Wang, Y. Deng, T. Zhao, W. Wang, and H. Zhang, “Processing Sliding Mosaic Mode Data With Modified Full-Aperture Imaging Algorithm Integrating Scalloping Correction,” *IEEE Journal of Selected Topics in Applied Earth Observations and Remote Sensing*, vol. 10, no. 5, pp. 1804–1812, May 2017.

[82] T. Instruments, “AWR1843 Single-Chip 77- and 79-Ghz FMCW Radar Sensor,” http://www.ti.com/lit/ds/swrs222/swrs222.pdf, Dec 2018, original document from Texas Instruments.

[83] F. T. Company, “AMC4030 Micro Controller,” http://www.fuyuautomation.com/article/cpsysc.html, Nov 2018, original document from FUYU Technology Company.